Nanoscale

ROYAL SOCIETY OF CHEMISTRY

REVIEW

View Article Online
View Journal | View Issue

Cite this: *Nanoscale*, 2024, **16**, 6778

Anisotropy in magnetic materials for sensors and actuators in soft robotic systems

Hyeokju Kwon, Yeonhee Yang, Geonsu Kim, Dongyeong Gim and Minjeong Ha *

The field of soft intelligent robots has rapidly developed, revealing extensive potential of these robots for real-world applications. By mimicking the dexterities of organisms, robots can handle delicate objects, access remote areas, and provide valuable feedback on their interactions with different environments. For autonomous manipulation of soft robots, which exhibit nonlinear behaviors and infinite degrees of freedom in transformation, innovative control systems integrating flexible and highly compliant sensors should be developed. Accordingly, sensor–actuator feedback systems are a key strategy for precisely controlling robotic motions. The introduction of material magnetism into soft robotics offers significant advantages in the remote manipulation of robotic operations, including touch or touchless detection of dynamically changing shapes and positions resulting from the actuations of robots. Notably, the anisotropies in the magnetic nanomaterials facilitate the perception and response with highly selective, directional, and efficient ways used for both sensors and actuators. Accordingly, this review provides a comprehensive understanding of the origins of magnetic anisotropy from both intrinsic and extrinsic factors and summarizes diverse magnetic materials with enhanced anisotropy. Recent developments in the design of flexible sensors and soft actuators based on the principle of magnetic anisotropy are outlined, specifically focusing on their applicabilities in soft robotic systems. Finally, this review addresses current challenges in the integration of sensors and actuators into soft robots and offers promising solutions that will enable the advancement of intelligent soft robots capable of efficiently executing complex tasks relevant to our daily lives.

Received 12th November 2023,
Accepted 29th February 2024

DOI: 10.1039/d3nr05737b

rsc.li/nanoscale

1. Introduction

Soft robots, known for their flexible designs and interactive features, introduce a paradigm shift in robotics by offering unique attributes for compliant, continuum, and configurable

School of Materials Science and Engineering, Gwangju Institute of Science and Technology (GIST), Gwangju 61005, Republic of Korea.
E-mail: minjeongha@gist.ac.kr

Hyeokju Kwon

Hyeokju Kwon received his BS from the Department of Organic Materials Science and Engineering, Pusan National University, South Korea, in 2023. He is currently pursuing his Combined Master's–Doctoral Program at the School of Materials Science and Engineering, Gwangju Institute of Science and Technology (GIST), South Korea, under the supervision of Prof. Minjeong Ha. His research interests are in the development of magnetic soft composites and applications for soft robotics.

Yeonhee Yang

Yeonhee Yang received her MS from Materials Science and Engineering, Gwangju Institute of Science and Technology (GIST), South Korea, in 2022 and BS from the Department of Display and Semiconductor Physics, Korea University, Sejong, South Korea in 2020. She is currently pursuing her Doctoral program at the School of Materials Science and Engineering, GIST, under the supervision of Prof. Minjeong Ha. Her research interests are in the development of magnetic field sensors for flexible electronics and soft robotics.

behaviors.[1] These complete soft-bodied systems demonstrate seamless adaptation to irregular surfaces and high degrees of freedom (DoFs) of transformation while exhibiting mechanical resilience.[2–4] This capability is achieved using intrinsically deformable and stretchable yet mechanically robust materials such as silicone elastomers, tough gels, functionalized polymers, and polymer composites.[5] These characteristics render soft robots superior in areas where conventional rigid robots struggle, playing roles in safe human interactions, handling of delicate objects, navigation of soft robots *via* confined spaces, and execution of intricate motions of these robots. However, the control of soft robots is more complex than that of rigid robots, which relies on well-defined kinematics of pre-formed joints. Soft bodies exhibit nonlinear viscoelastic behavior with significant hysteresis and different degrees of transformation based on their designs and material compositions. Therefore, predicting their responses and changes in their shapes and positions in a three-dimensional (3D) space is challenging.[6]

The locomotion of soft robots depends on adjustments of the dimension and stiffness of the materials constituting the robot bodies. Stimuli-responsive materials demonstrate notable actuating mechanisms, including energy-efficient and precise control of motion in response to external triggers such as heat, light, humidity, and electric and magnetic fields.[7] During the operation of soft robots in untethered states and dynamic environments as illustrated in Fig. 1, magnetic field-responsive materials allow robot bodies to undergo immediate transformation owing to a relatively fast response time of these materials as compared with those of other stimuli-responsive materials.[8] Additionally, magnetic field-driven actuation facilitates remote operation of untethered soft robots because magnetic fields can penetrate *via* various media while decoupling from other stimuli, for example, mechanical stress, radiation, illumination, and humidity.

For delicate control of a soft robot, the capability for directional actuation has attracted significant attention.[9,10] However, achieving a directional response to external stimuli often requires complicated designs. By employing materials with inherent anisotropic characteristics, it becomes possible to implement directional actuation without the design of complex structures.[11] For example, Kim *et al.* demonstrated an electrothermal soft actuator utilizing the anisotropic thermal expansion of low-density polyethylene (LDPE).[12] They designed a bilayer structure comprising LDPE, which has a large anisotropic thermal expansion, and polyvinyl chloride, which exhibits a small isotropic thermal expansion. The mismatch in thermal expansion between the layers results in directional bending in response to electrical stimuli. The significance of magnetism in manipulating robotics is attributed to the selective and directional response capabilities of magnetic materials induced by magnetic anisotropy, which can be obtained by either localized magnetization or the strategical distribution of micro/nano-scale magnets at desired spots in the soft matrix. Magnetic anisotropy with a preferred pole enables the generation of strong torques or programmable actuations along the magnetic easy axes without pre-defined structures.

Soft robotic systems mimicking the sensorimotor functions of biological organisms exhibit adaptabilities to variable and uncertain environments because of the integration of magnetic sensors into their actuating bodies. A closed-loop control system with magnetic sensors and actuators allows the robot to autonomously adjust its activities based on sensory feedback.[13–15] Without sensory feedback, even minor variations in material properties or environmental factors can cause errors that disrupt the sequential actuation and hinder task completion. Nevertheless, traditional rigid, chip-type magnetic sensors encounter difficulties in delivering high-quality signals due to their inferior mechanical compliance with soft bodies.[16] Fortunately, progress in materials science and flexible electronics has led to the development of stretchable, highly deformable, and conformable magnetic sensors that

Geonsu Kim

Geonsu Kim received his MS from the the Department of Carbon Composites Convergence Materials Engineering, Jeonbuk National University, South Korea, in 2023 and BS in the Department of Organic Materials and Textile Engineering from Jeonbuk National University in 2021. He is currently pursuing his Doctoral Program at the School of Materials Science and Engineering, Gwangju Institute of Science and Technology (GIST), under the supervision of Prof. Minjeong Ha. His research interests are in the development of flexible multifunctional sensing devices for human health monitoring and soft robotics.

Dongyeong Gim

Dongyeong Gim is currently pursuing his BS program at the Department of Chemistry, Gwangju Institute of Science and Technology (GIST), South Korea. His research interests are in the development of magnetic soft composites and applications for EMI shielding.

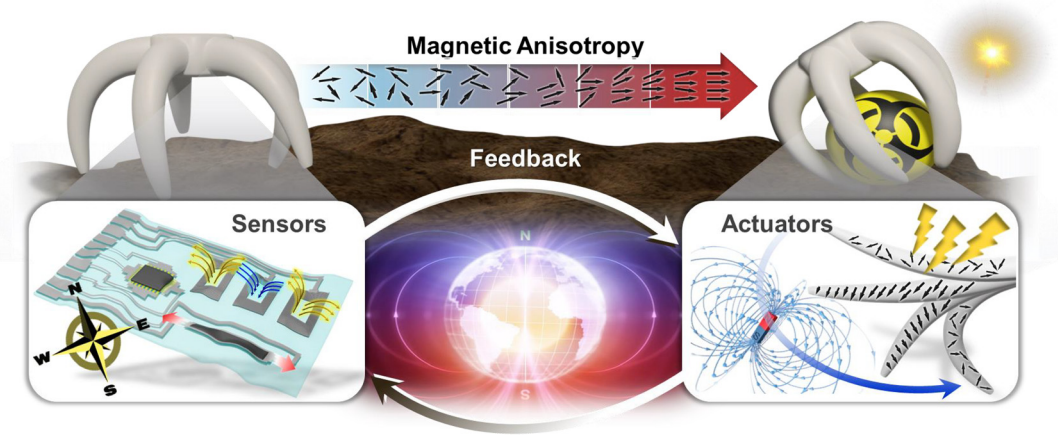

Fig. 1 Magnetic soft robot autonomously operating in dynamic environments. The schematic illustration depicts that the magnetic anisotropy facilitates the sensing capabilities for both robotic motions and the surrounding changes as well as the precise manipulation of actuation for the applications of soft robots.

can be integrated into soft robots without disturbing their motion and degrading the softness of the robot bodies. To monitor both the movements of a robot and its surroundings, two distinct sensing modalities are necessary: proprioception and exteroception.[16–18] Proprioceptive sensors provide information about the internal states of the robot bodies during actuation,[18] whereas exteroceptive sensors detect changes in the surroundings to identify the location of the robot.[16] Magnetic sensors are versatile for these sensing modalities because they not only can detect the variations in stray fields caused by the actuations of magnetic robot bodies, but can also determine the proximity of external magnetic field sources. Particularly, magnetic anisotropy demonstrates strong responses to certain axial directions of the magnetic field. Sensors with magnetic anisotropy offer exceptional sensitivity, accuracy, and selectivity for recognizing the shape and position of soft robots while minimizing interference and crosstalk resulting from varying magnetic field orientations or the integration of multiple magnetic sensors into the robot bodies. Despite the challenges associated with integrating sensors and actuators due to the potential for interference among the components, this integration remains essential for the advancement of soft robotics with seamless operation. Thus, anisotropy in magnetic nanomaterials is indispensable for high compatibility of both sensors and actuators in terms of controlling actuation and tracking changes in the internal and external states of magnetic soft robots. The anisotropy guarantees the successful execution of various missions and tasks.

This review aims to investigate magnetic nanomaterials with a particular focus on magnetic anisotropy and applications of these nanomaterials in sensors and actuators, which are key components in soft robotics (Fig. 1). First, we discuss the origins of magnetic anisotropy and underlying mechanisms that drive anisotropy in magnetism considering the energy in the system. Then, a variety of magnetic nanomaterials with enhanced magnetic anisotropy through alignment, shape control, interlayer coupling, and external energy source (*e.g.* mechanical and magnetic energy) are highlighted. These magnetic nanomaterials are categorized based on their dimensions and dominant magnetic anisotropy, which will be discussed in section 2. Furthermore, we present the compatibility of each magnetic nanomaterial with distinct magnetic anisotropy and discuss how these materials and corresponding magnetisms satisfy the specific requirements of sensors, actuators, or both in soft robotic applications. As these magnetic nanomaterials are sufficiently compliant with the pliable bodies of soft robots, we investigate their design, fabrication, and manufacturing processes aimed at preserving the aniso-

Minjeong Ha

Minjeong Ha is currently an assistant professor in the School of Materials Science and Engineering at Gwangju Institute of Science and Technology (GIST), Republic of Korea. She received her PhD and MS from the School of Energy and Chemical Engineering at Ulsan National Institute of Science and Technology (UNIST) in 2019 and her BS from the School of Nano-Bioscience and Chemical Engineering at UNIST in 2013. She worked as a postdoctoral fellow at Helmholtz-Zentrum Dresden-Rossendorfe (HZDR) in Dresden, Germany, from 2019 to 2020 and as a researcher at the Electronics and Telecommunications Research Institute (ETRI) in the Republic of Korea from 2020 to 2021. Her research interests include magnetic nanomaterials and stimulus-responsive soft composites for flexible sensors, soft actuators, and energy-harvesting devices.

tropic properties of these materials and maintaining the requisite softness of the corresponding soft robots. Finally, we examine how magnetic anisotropy contributes to enhancing the performances of magnetic sensors and actuators with a particular emphasis on the crucial roles of magnetic sensors and actuators in enabling various functions in soft robots.

2. Fundamentals of magnetic anisotropy

Magnetic anisotropy denotes the pinning of magnetic moments in a specific orientation, leading to directional dependence of the magnetization, which is observed in ferromagnetic (FM) materials. To understand this directional dependence, anisotropy energy needs to be considered. In other words, a preferred direction of magnetization, namely, the magnetic easy axis, arises to minimize the anisotropy energy. Various anisotropies originate from different mechanisms and the total energy of the system is determined by the interactions between them, rather than a single mechanism. The total energy in magnetic materials is expressed as follows:

$$E_{\text{total}} = E_{\text{Zeeman}} + E_{\text{crys}} + E_{\text{sh}} + E_{\text{me}} + E_{\text{ex}} \quad (1)$$

Note that the E terms in this review denote the energy density caused by the dominant mechanism of anisotropy while the E_{Zeeman} is associated with the interaction between the magnetic moments and external magnetic field (H_{ext}). Specifically, the magnetic anisotropy energy density originates from several key factors: crystal orientation (E_{crys}), dimension and shape (E_{sh}), magnetoelasticity (E_{me}), and interfacial exchange coupling (E_{ex}) of magnetic materials. The complex interplay of these energies elucidates how FM materials exhibit a magnetic easy axis resulting in directional responses under H_{ext} (Fig. 2). Therefore, we will discuss how the dominant energy term varies with respect to material size, dimension, shape, surface, and other relevant variables in this section (Fig. 2a). Subsequently, we discuss how the anisotropy energy influences the directional behavior and magnetization state (Fig. 2b), considering both intrinsic and extrinsic properties of magnetic materials.

2.1. Intrinsic magnetocrystalline anisotropy

Crystallographic orientations in magnetic materials yield preferential directions of magnetization for minimizing anisotropy energy known as magnetocrystalline anisotropy. This fundamental mechanism of magnetocrystalline anisotropy originates from spin–orbit coupling along with the interaction between the orbital motion of electrons and the crystal field of the lattice.[19,20] Assuming that the orbital contributions to magnetic moments are quenched, magnetic properties are primarily determined by the spin of the electron. Notably, the orientations of the crystal structures do not strongly affect the electron spin. However, spin–orbit coupling can bridge the gap between the spin and crystal lattice as the orbital orientation

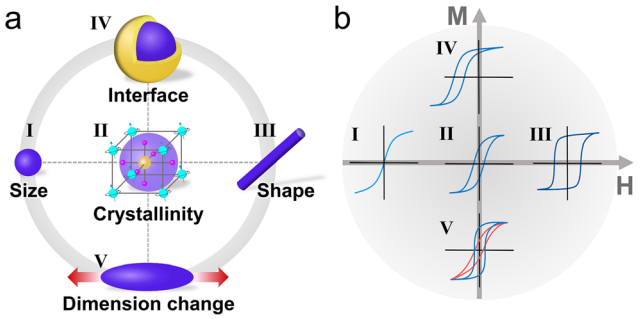

Fig. 2 Factors influencing the magnetization states of nanomaterials. (a) Magnetic properties induced by (I) size, (II) crystallinity, (III) shape, (IV) interfacial coupling, and (V) dynamic changes in the dimensions of magnetic nanomaterials. (b) Magnetization state verified by magnetization hysteresis loops based on the factors in (a): (I) a decrease of size led to superparamagnetism, (II) the crystal structure determined the inherent magnetizations of materials and hysteresis curve shapes, (III) shape anisotropy resulted in increasing coercivity and remanent magnetization, (IV) exchange coupling at the interface between different magnetic materials caused curve shifts, and (V) there were dynamic changes in the magnetization states according to the magnetostrictive properties of the materials.

becomes firmly fixed to the lattice.[21] This interaction leads to an anisotropy energy that defines the preferred orientation of magnetization.

Fig. 3 illustrates the magnetocrystalline anisotropy of magnetic materials, particularly for the simplest cases of hexagonal close-packed cobalt (hcp-Co), body-centered cubic iron (bcc-Fe), and face-centered cubic nickel (fcc-Ni). For cobalt, which has a hexagonal crystal structure, the easy axis is along the [0001] direction, while the hard axis is in the $\langle 10\bar{1}0 \rangle$ directions (Fig. 3a). The hard axis is defined as an unfavored direction of magnetization, requiring a higher field to be saturated in that direction. The behavior of hcp-Co can be explained by the energy of the system, which is described in the following equation:

$$E_{\text{crys,hexagon}} = K_0 + K_1 \sin^2\theta + K_2 \sin^4\theta + \ldots \quad (2)$$

where K_n (n = 0, 1, 2, 3...) is the n-th magnetocrystalline anisotropy constant, and θ is the angle between the magnetization and the c-axis of the hexagonal system.[22] Generally, K_0 is disregarded since it is an isotropic value. hcp-Co has a K_1 of 4.5 Merg cm^{-3} and K_2 of 1.5 Merg cm^{-3}.[23] Thus, the energy of hcp-Co is minimized when θ equals 0° or 180°, as described by eqn (2). This explains why the easy axis is aligned in the [0001] direction, while the hard axis is aligned in the $\langle 10\bar{1}0 \rangle$ direction. Since hcp-Co has a single easy axis along the c-axis, it exhibits uniaxial anisotropy.

The situation for bcc-Fe and fcc-Ni is quite different compared with hcp-Co (Fig. 3b and c). They have multiple easy axes, which can be also explained by the energy of the system. For cubic symmetry,

$$E_{\text{crys, cubic}} = K_0 + K_1(\alpha_1^2\alpha_2^2 + \alpha_2^2\alpha_3^3 + \alpha_3^2\alpha_1^2) + K_2(\alpha_1^2\alpha_2^2\alpha_3^2) + \ldots \quad (3)$$

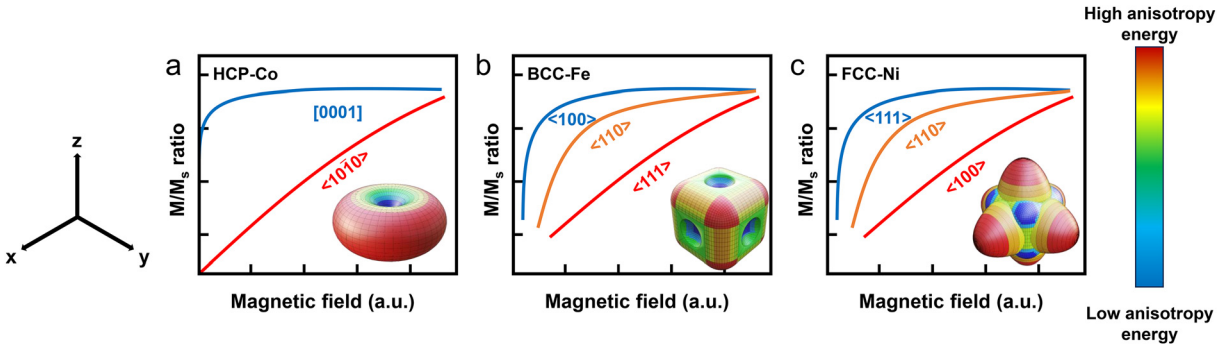

Fig. 3 Magnetocrystalline anisotropy of the simplest magnetic materials such as (a) hcp-Co, (b) bcc-Fe, and (c) fcc-Ni. The inset images in each figure represents magnetocrysalline ansisotropy energy. The red color represents high magnetic anisotropy energy resulting in a hard axis along that direction while the blue color represents low magnetic anisotropy energy forming an easy axis in the direction.

where the directional cosines of magnetization with cubic crystal axes are denoted as α_1, α_2, and α_3. The anisotropy energy of fcc-Ni and bcc-Fe is mainly determined by K_1, since higher order constants are relatively small. The K_1 value of bcc-Fe is 4.8×10^5 erg cm^{-3} resulting in an easy axis along the ⟨100⟩ directions (Fig. 3b), while the K_1 of fcc-Ni is -0.5×10^5 erg cm^{-3}, forming an easy axis along the ⟨111⟩ directions (Fig. 3c).[21] Notably, as bcc-Fe has three easy axes and fcc-Ni has four easy axes, they are not commonly described as exhibiting uniaxial anisotropy.[24] Thus, bcc-Fe and fcc-Ni have a less anisotropic structure than hcp-Co, resulting in a lower coercivity and remanence.

2.2. Shape anisotropy and finite size effect

The preferential magnetization direction induced by magnetic anisotropy energy is influenced by not solely the intrinsic crystallographic geometry, but also the shapes and sizes of the magnetic materials. Unlike the case of magnetocrystalline anisotropy, the energy derived from shape anisotropy can be deliberately adjusted by tailoring the designs of magnetic materials with specific structures and dimensions. All magnetic materials inherently possess a demagnetizing field (H_d) resulting from the magnetostatic interaction between the north and south poles in materials when they are subjected to H_{ext} (Fig. 4a).[25] Moreover, H_d is directly proportional to $-N_dM$, where N_d indicates the demagnetizing factor and M corresponds to the magnetization of the materials. N_d is a shape-dependent parameter, which provides an opportunity to modulate the magnitude of H_d in magnetic materials. For example, in the cases of isotropic and spherical magnetic particles, N_d is equal to 1/3. However, for an ellipsoidal magnetic particle, N_d varies depending on the axis of the particle (Fig. 4b). Along the longest axis, denoted as "c", N_c is less than 1/3 as the magnetostatic forces decrease with respect to the pole distance (r), demonstrating an inverse square relationship with r ($1/r^2$). Simultaneously, along the shortest axis, denoted as "a", N_a is larger than 1/3 because the sum of the demagnetizing factors is equal to 1 for each axis.[25,26]

The magnitude of the demagnetizing field resulting from the shape-dependent differences in N_d defines the shape anisotropy energy E_{sh}, which can be expressed as follows:

$$E_{sh} = -\frac{1}{2}\mu_0(M \cdot H_d) \quad (4)$$

$$E_{sh} = \frac{1}{2}\mu_0(N_a{M_a}^2 + N_c{M_c}^2) \quad (5)$$

$$E_{sh} = \frac{1}{2}\mu_0 M^2(N_c \cos^2\theta + N_a \sin^2\theta) \quad (6)$$

where μ_0 and θ represent the permeability of free space and angle of magnetization direction with respect to the longest axis, respectively.[27] N_c and N_a are the demagnetizing factors for each axis. When N_c converges to zero and the direction of magnetization aligns with the c-axis, E_{sh} becomes minimum. Consequently, the easy axis of magnetization aligns with the longest axis of the ellipsoidal particle to minimize the energy of the system, and it can be treated as uniaxial anisotropy. Thus, fine-tuning the apparent shape of magnetic materials by adjusting the aspect ratio leads to changes in the magnetic properties, representatively coercivity and remanence.[22]

The size of the magnetic materials is another key factor affecting the magnetic properties and even contributes to magnetic anisotropy, specifically with a decrease in dimensions (Fig. 4c and d).[28] Bulk magnets naturally form a multi-domain state to minimize the magnetostatic energy instead of involving all spins aligned in parallel.[29] However, when the size of a magnetic particle is reduced to the nanoscale, it transitions into a single-domain state upon reaching a specific diameter (D_{sd}). Assuming an uniaxial magnetic material for simplification, D_{sd} can be calculated as follows:

$$D_{sd} = \frac{18(AK_u)^{1/2}}{\mu_0{M_s}^2} \quad (7)$$

where A represents the exchange stiffness and K_u denotes an uniaxial anisotropy constant that is assumed to be sufficiently

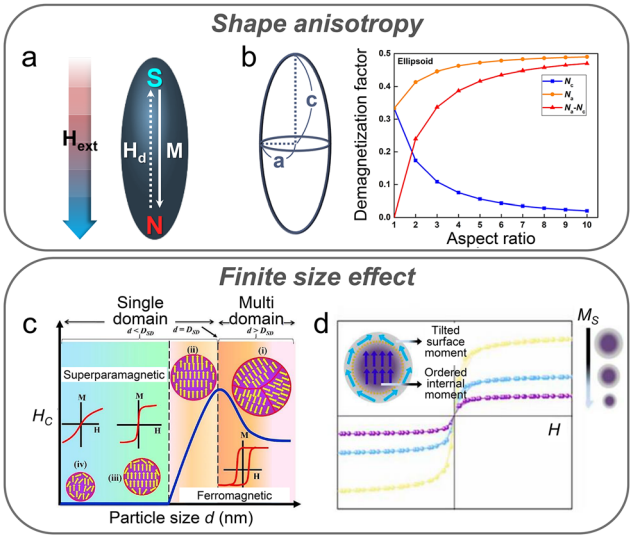

Fig. 4 Magnetism based on the shape and size of magnetic materials. Under external magnetic fields, (a) a demagnetizing field generated along the long-axis direction due to shape anisotropy. (b) Relationship between demagnetizing factors and the aspect ratio of a prolate ellipsoid. Reproduced with permission.[26] Copyright, the Creative Commons CC BY License. (c) Size-dependent behavior of coercivity in magnetic nanomaterials. Reproduced with permission.[28] Copyright, the Creative Commons CC BY License. (d) Decrease in saturation magnetization owing to magnetic dead layers with a decrease in the size of the magnetic nanomaterials. Reproduced with permission.[36] Copyright, the Creative Commons CC BY License.

strong. If materials have a small K_u, D_{sd} is defined by including the lattice constant "a" as follows:[23]

$$D_{sd} = 2\sqrt{\frac{9A}{\mu_0 {M_s}^2}\left[\ln\left(\frac{D_{sd}}{a}\right) - 1\right]} \quad (8)$$

In the single-domain state, the magnetization is uniformly aligned along a particular direction, and the magnetization reversal is caused by the coherent rotation of the magnetic moment which is described by the Stoner–Wohlfarth model, leading to higher coercivity than that in the multi-domain state.[30] With a decrease in the diameter of a magnetic particle to below the sub-nanometer scale, E_{crys} reduces across the entire volume of the particle. When E_{crys} falls below the thermal energy threshold, the magnetic orientation within the particle experiences thermal fluctuations, which are commonly observed in paramagnetic materials. This state is referred to as superparamagnetism.[31] The critical diameter (D_{sp}) at which a particle exhibits superparamagnetic properties can be defined as follows:

$$D_{sp} = \left(\frac{48 k_B T}{K_u}\right)^{1/3} \quad (9)$$

where k_B and T represent the Boltzmann constant and temperature.[32] For example, the magnetic domain configuration and associated magnetism of an Fe_3O_4 nanoparticle (NP) considerably shift from FM to superparamagnetic behavior with changes in the particle diameter, that is, D_{sd} (~80 nm) and D_{sp} (~25 nm) at room temperature, respectively.[33,34] Hence, the size of the magnetic particles at the nanoscale significantly affects the coercivity of the magnetic materials (Fig. 4c). Unlike coercivity, saturation magnetization (M_s) is not inherently dependent on material dimensions.[21] However, the presence of defects on material surfaces because of incomplete coordination or disrupted symmetry generates a magnetic dead layer characterized by spin canting and a disorder of magnetic moments. This, in turn, reduces the M_s (Fig. 4d).[22,35,36] Because of their high surface-to-volume ratio arising from the nanosize effect, magnetic NPs (MNPs) typically exhibit lower M_s values.

2.3. Exchange anisotropy

Interfacial coupling between magnetic bilayers or multilayers can be observed by an extrinsic factor, namely, exchange anisotropy. This phenomenon occurs at the interface between an FM material and an adjacent antiFM (AFM) material, resulting in a unidirectional magnetization orientation in the FM material.[37,38] This interfacial coupling is not limited to FM/AFM bilayers but extends to other magnetic configurations, such as FM/AFM superlattices,[39] ferrimagnet (FI)/AFM,[40] FI/FM,[41] soft FM/hard FM,[42] and FM/spin glass systems.[43] Unidirectional pinning of the magnetization notably alters the hysteresis loop of the FM/AFM coupled layers when compared with that of a standalone FM layer, where the center of the hysteresis loop shifts from the zero magnetic field position (Fig. 5a). This shift in the magnetic hysteresis loop is termed bias, which is a behavior associated with exchange anisotropy and is thereby called exchange bias. During magnetic-thermal treatment (Fig. 5a), the exchange bias appears after cooling the FM/AFM coupled system. Typically, critical temperature limits exist for both FM and AFM materials, denoted as the Curie temperature (T_C) and Néel temperature (T_N), at which magnetic materials exhibit phase transitions and subsequently change or lose their magnetism. Within the temperature range of $T_N < T < T_C$, the spins in the FM layer can align in the direction of H_{ext}, while the spins in the AFM layer randomly orient. When the temperature decreases below T_N, the spins in the AFM layer adjacent to the FM layer are oriented to the spin configurations of the FM layer. The other spin planes in the AFM layer follow the rule of antiparallel alignment for a zero net magnetization. If the magnetic field is reversed, the spins in the FM layer rotate, whereas those in the AFM layer remain unchanged. The stationary spins exert a torque that resists the spin rotation in the FM layer, holding the spins in their initial orientation. Thus, the complete reversal of the spins in the FM layer coupled with an AFM layer requires a larger field to overcome the torque. Owing to this interfacial coupling, the magnetic hysteresis loop shifts and coercivity changes.

Numerous models have been proposed to explain exchange bias in different systems. An early simple model was suggested by Meiklejohn-Bean to describe oxidized FM particles (Co/CoO).[44] This model assumed an atomically smooth FM/AFM

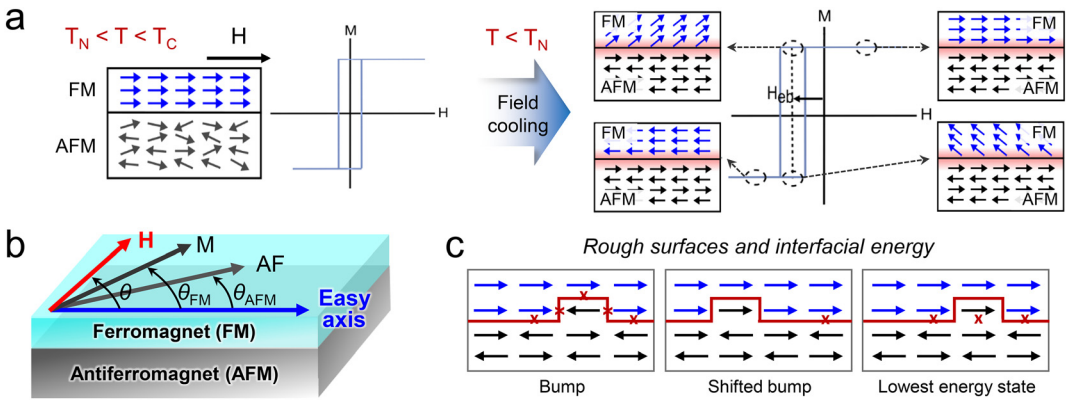

Fig. 5 Exchange bias in magnetic interlayers. (a) Spin configurations and magnetization curves of the FM/AFM bilayer. At $T_N < T < T_c$, the centered magnetization curve and the paramagnetic state of the AFM layer are alongside the aligned spin state in the FM layer (left). A field cooling process induces a shift in the magnetization curve, and this shift is known as exchange bias. Reproduced with permission.[37] Copyright 1999, Elsevier Science B.V. (b) Magnetic easy axis based on exchange anisotropy arising from FM/AFM interlayer coupling and angular relationships of the magnetization of the FM layer with respect to the external field direction. (c) Magnetic moment configuration at the FM/AFM interface with a bump. The cross symbol represents frustrated bonds. Starting from the fully compensated state of the AFM layer, the introduction of a bump generates AFM deviations. A shifted bump induces FM deviations resulting in a net interfacial energy difference. When the lowest energy state is achieved, the interfacial energy difference is reduced. Reproduced with permission.[46] Copyright 1987, American Physical Society.

interface, where both magnetic materials existed in a single domain. In the AFM material, the uncompensated spins are aligned in the same crystallographic plane and direction at the interface of FM/AFM, due to the aforementioned cooling step. Then, the exchange anisotropy energy required to overcome the resistance of spin rotation in the coupled FM material was calculated. This exchange bias model considered the total energy (E) originating from the coherent rotation of FM magnetization as follows:[37]

$$E = -HM_S t_{FM}\cos(\theta - \theta_{FM}) + K_{FM} t_{FM}\sin^2\theta_{FM} + K_{AFM} t_{AFM}\sin^2\theta_{AFM} - J_{eb}\cos(\theta_{FM} - \theta_{AFM}) \quad (10)$$

The sequence in eqn (10) presents the uniaxial anisotropy of FM and AFM materials, and exchange anisotropy energy. Here, H is the applied field, M_S is the saturation magnetization of the FM layer, and t_{FM} and t_{AFM} denote the thickness of the FM and AFM layers, respectively. K_{FM} and K_{AFM} represent the uniaxial anisotropy constants of the FM and AFM layers. As K_{AFM} is typically larger than K_{FM}, K_{FM} can be ignored. J_{eb} is the interlayer exchange anisotropy constant. In addition, θ, θ_{FM}, and θ_{AFM} denote the angles of the applied magnetic field, magnetization of the FM layer, and sublattice magnetization of the AFM layer with respect to the predetermined easy axis of the FM and AFM layers (Fig. 5b). Then, the exchange anisotropy energy was defined as follows:

$$E_{ex} = -J_{eb}\cos(\theta_{FM} - \theta_{AFM}) \quad (11)$$

The exchange anisotropy is often regarded as unidirectional anisotropy rather than uniaxial, since it is proportional to the first power of the cosine. When the spin alignment of the AFM layer matches the easy axis, that is, $\theta_{AFM} \approx 0$, the field required to switch the magnetization of the FM layer is defined as the exchange bias field, H_{eb}. Considering the energy stability condition ($\partial E/\partial\theta = 0$), H_{eb} can be obtained as follows:

$$H_{eb} = \frac{J_{eb}}{M_S t_{FM}} \quad (12)$$

According to eqn (12), the exchange bias field is inversely proportional to the thickness of the FM layer because of its association with interfacial characteristics.[37] However, in this model, the assumption regarding the presence of fully uncompensated spins at the interface causes differences in H_{eb} with experimental results.[45] In the uncompensated case, all AFM spins at the FM/AFM interface are aligned in the same direction and the J_{eb} is directly proportional to the FM exchange constant J_i. However, the actual spin configuration of the AFM surface is considerably complex due to a non-ideal FM/AFM layer.

Several models have been proposed to address this gap and elucidate the mechanism of exchange bias at the FM/AFM interface. According to the random field model proposed by Malozemoff, the dynamics of interfacial conditions, including defects at the interface between the FM and AFM layers, produces a randomness in the H_{eb} of the system.[46] In the presence of local bumps (Fig. 5c), the net interfacial energy difference decreases as the AFM spin in the bumps is inverted at the lowest energy state, thus affecting the total exchange anisotropy constants. For example, the net interfacial energy difference, which is calculated as $6 \times 2J_i = 12J_i$, is reduced by $5 \times 2J_i$ owing to the existence of the bump when the system reaches its lowest energy state. The energy difference $4J$ results from the summation of the FM exchange constant ($2J_i$) and AFM constant ($2J_A$), assuming $J \approx J_i \approx J_A$. Eventually, a perpendicular domain-like region is formed to minimize the net

random unidirectional interfacial anisotropy. In this model, H_{eb} is acquired as follows:

$$H_{eb} = \frac{\Delta\sigma}{2M_{FM}t_{FM}} = \frac{2z\sqrt{A_{AFM}K_{AFM}}}{\pi^2 M_{FM}t_{FM}} \quad (13)$$

Average interfacial energy is defined as, $\Delta\sigma = 4zJ/\pi aL$, where z, J, a, and L represent the number of antiparallel pairs, exchange coupling constant, cubic lattice parameter, and domain size, respectively. Furthermore, A_{AFM} is the exchange stiffness of the AFM layer, also represented as $A_{AFM} \equiv J/a$. The inherent randomness influences the behavior of the domain wall in the AFM layer, which weakens the H_{eb} strength.

Domain wall formation in the AFM layer bridges the theoretical and experimental differences in exchange bias. The random field model associates the exchange bias with a domain wall perpendicular to the FM/AFM interface, while Mauri's model assumes that the domain wall in the AFM layer is parallel to this interface. Thus, the calculated H_{eb} is lower than what is predicted by the Meiklejohn–Bean model.[47] Nevertheless, when t_{AFM} reduces below a critical level, the domain wall is not formed, leading to the disappearance of H_{eb}. As an ultra-thin AFM layer forms island-like grains rather than a continuous film, this layer is insufficient for coupling with the FM layer.[48] Moreover, the domain state model indicates that a domain is formed in the bulk AFM layer during magnetic thermal treatment.[49] In this process, the AFM layer experiences magnetic dilution due to non-magnetic (NM) defects. Domain wall formation is energetically favorable as this wall passes through the NM defects, causing its pinning. Subsequently, this pinned domain wall lowers H_{eb} by reducing the number of uncompensated spins at the FM/AFM interface. Consequently, t_{AFM} is a critical factor in determining the potential of the defects that may impact exchange anisotropy.

Although the interfacial conditions of the FM/AFM layers affect the exchange bias, the crystallographic orientation of the AFM material should also be considered for explaining exchange anisotropy because of the relationship between the bulk crystallinity and spin configurations at the interface of the FM/AFM layers.[50,51] Assuming that the AFM spins at the FM/AFM interface are similar to those in the bulk material, which are significantly affected by the crystallographic structure, an angle is inevitably formed between the AFM and FM spins. Then, the exchange bias depends on the angle between the AFM and FM spins. According to the Hamiltonian equation for exchange bias, $J_{int}|S_{AFM}||S_{FM}|\cos\alpha$, where $\alpha = 0°$ results in maximum H_{eb} and $\alpha = 90°$ indicates no exchange bias.[52] The crystal orientation of the AFM layer at the interface determines whether this layer is in a compensated or an uncompensated state. Consequently, the exchange anisotropy is not only evidently determined by the interfacial condition between the FM and AFM layers, but also significantly influenced by the thickness and crystal structure of these layers. By considering the factors associated with exchange bias, the strength and stability of H_{eb} can be controlled. This capability is of considerable importance as it tunes the behavior of the magnetic material based on exchange anisotropy according to the specific requirements of magnetic field sensors. For example, exchange bias is applied to anisotropic magnetoresistance (AMR)-based sensors to adjust the magnetization direction.[53,54] Furthermore, exchange bias is applied to spin valve[55] and magnetic tunnel junction devices[56] to appropriately pin the magnetization of the FM layer.

2.4. Stress-induced magnetic anisotropy

In the previous sections, the different parameters, including both intrinsic magnetocrystalline anisotropy and extrinsic influences such as adjusting the dimensions, shapes, and interlayer coupling of the magnetic materials, governing magnetic anisotropy and its associated energy are comprehensively discussed. Magnetic anisotropy has been explored in a static state without considering dynamic conditions, for instance, applied mechanical stress, temperature changes, and the different strengths and directions of stray fields. In this section, we investigate magnetic materials exhibiting dynamic behaviors in which anisotropy can be induced by mechanical stress.

Magnetostriction is a phenomenon where the dimensions of a material vary in response to alterations in its magnetization orientation, accompanied by domain wall motion under H_{ext}.[57,58] Magnetic materials exhibit strain of the saturation magnetostriction coefficient (λ_{si}) in the direction of the magnetic field during magnetization.[59] Thus, the presence of magnetostriction implies that mechanical stress can vary the magnetic domain and can be a new source of magnetic anisotropy.[60–62] This variation of magnetization under stress is known as inverse magnetostriction or, more commonly, the magnetoelastic effect.[62,63] The magnetoelastic effect is correlated with λ_{si} and the magnetic behaviour of a material under stress (σ). λ_{si} can be positive or negative depending on the crystal structure of the materials and composition of the alloys. For example, bcc-Fe exhibits a positive λ_{si}, whereas fcc-Ni shows a negative λ_{si}.[64] Conversely, $Fe_{20}Co_{80}$ alloys are in the fcc phase for a positive λ_{si} or bcc phase for a negative λ_{si} depending on the fabrication methods.[65] If a magnetic material has a positive λ_{si}, it will elongate during magnetization. This implies that applying a tensile stress to lengthen the material ($\lambda_{si}\sigma > 0$) increases the magnetization of the material, which facilitates the formation of a preferential orientation of the easy axis.[58,66] However, magnetization in a material may not always be parallel to stress, and the resulting M_s can be understood by considering the magnetic anisotropy energy of the system. Assuming a simple cubic crystal, the overall magnetic anisotropy energy can be expressed as

$$\begin{aligned} E = {} & K_1(\alpha_1^2\alpha_2^2 + \alpha_2^2\alpha_3^2 + \alpha_3^2\alpha_1^2) \\ & - \frac{3}{2}\lambda_{100}\sigma(\alpha_1^2\gamma_1^2 + \alpha_2^2\gamma_2^2 + \alpha_3^3\gamma_3^2) \\ & - 3\lambda_{111}\sigma(\alpha_1\alpha_2\gamma_1\gamma_2 + \alpha_2\alpha_3\gamma_2\gamma_3 + \alpha_3\alpha_1\gamma_3\gamma_1) \end{aligned} \quad (14)$$

where the first term depicts the E_{crys} of a cubic crystal, as shown in eqn (3), whereas the last two terms represent the

magnetoelastic energy E_{me}.[58,67] γ_1, γ_2, and γ_3 are the direction cosines of σ with respect to the crystal axes. Assuming an isotropic magnetostriction where $\lambda_{100} = \lambda_{111} = \lambda_{si}$ for simplification and that E_{me} is much larger than the first term in eqn (14), stress dominates in the energy of the system followed by determination of the M_s direction.[68] A general case where stress is applied to the cubic magnetic materials at an angle of θ with respect to M_s is shown in Fig. 6a. As the magnetostriction in the direction of stress (λ_θ) is deviated from λ_{si}, λ_θ is lower than λ_{si}. Subsequently, this difference in magnetostriction changes the energy of the system as follows:

$$dE_{me} = -\sigma d\lambda \quad (15)$$

Therefore, the total E_{me} can be derived by using a simple term:

$$\int_0^{E_{me}} dE_{me} = -\sigma \int_{\lambda_{si}}^{\lambda_\theta} d\lambda \quad (16)$$

$$E_{me} = -\sigma\left[\frac{3}{2}\lambda_{si}\left(\cos^2\theta - \frac{1}{3}\right) - \lambda_{si}\right] \quad (17)$$

$$E_{me} = \frac{3}{2}\lambda_{si}\sigma \sin^2\theta \quad (18)$$

eqn (18) can be simplified by introducing K_σ which is the stress anisotropy constant, and then E_{me} can be expressed as

$$E_{me} = K_\sigma \sin^2\theta \quad (19)$$

According to eqn (19), when a material has a positive K_σ, E_{me} is minimum at $\theta = 0°$ and maximum at $\theta = 90°$.[61] Thus, the magnetic easy axis is formed along the direction of stress to minimize the energy of the system. For a negative K_σ, the situation is reversed, as the magnetic easy axis is perpendicular to the system. Since external stress induces a single easy axis even in cubic materials, stress-induced anisotropy can be treated as uniaxial anisotropy.

A polycrystalline material typically demonstrates a weak crystal anisotropy without a preferential orientation, often existing in a demagnetized state (Fig. 6b-i and c-i).[69] An applied tensile stress initiates domain wall motion, increasing the volume of the domains magnetized in a stress-induced easy axis, thereby exerting the direction of M_s (Fig. 6b-ii and c-ii).[61] As all domains are aligned with the easy axis, E_{me} is minimized (Fig. 6b-iii and c-iii).[70,71] Upon applying H_{ext} (Fig. 6b-iv and c-iv), the magnetization curve of a positive K_σ would appear as the case of easy-axis magnetization of the uniaxial magnetic material, whereas for a negative K_σ, the magnetization curve would be similar to that of hard-axis magnetization (Fig. 6d).[58]

Representative materials with a magnetostriction effect include Co, Ni, Fe, permalloy (Ni–Fe alloys), Terfenol-D ($Tb_xDy_{1-x}Fe_2$), and Galfenol (Fe–Ga alloys).[59,72–74] However, the levels of magnetoelasticity in these materials may vary. Considering the total energy in eqn (14), materials with a relatively larger value of K_1 than λ_{si} are primarily influenced by crystal anisotropy rather than stress anisotropy. Modulation of the magnetic anisotropy in this crystal system *via* applied stress requires an energy contribution from stress anisotropy that is at least equal to that of the crystal anisotropy energy. Therefore, materials with a low λ_{si} value need significantly higher stress levels to achieve a high K_σ, as expressed by the relationship, $K_\sigma = 3/2\lambda_{si}\sigma$. This may exceed the yield stress of the materials, potentially causing failure. Thus, magnetic anisotropy is not determined by a single mechanism, but is affected by complicated relationships between various mechanisms. A summary of magnetic anisotropies ranging from intrinsic magnetocrystalline anisotropy to extrinsic magnetic anisotropies is presented at Table 1.

3. Synthesis and design strategies for anisotropy in magnetic materials

3.1. Anisotropic assemblies of zero-dimensional magnetic nanomaterials

Magnetic behaviors of spherical MNPs, characterized by isotropic morphologies and properties in all directions, exhibit size dependence instead of directional dependence. When reduced to the single-domain size, typically, below tens of nanometers, these MNPs commonly demonstrate superparamagnetism. This phenomenon is attributed to the fact that the thermal energy-induced transition of spin direction drives magnetic

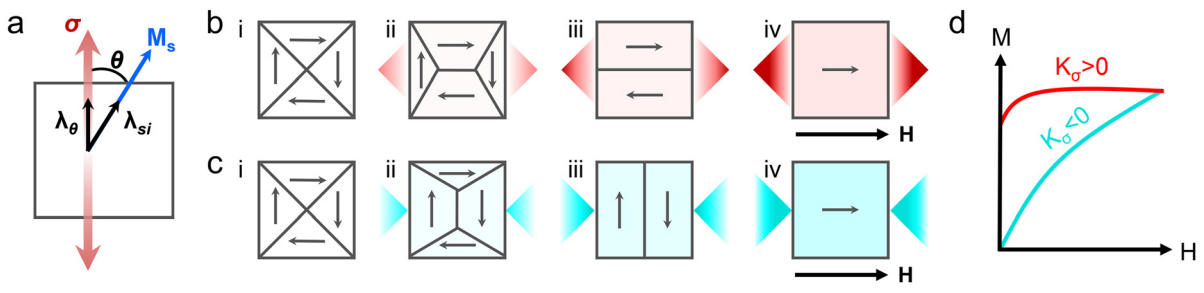

Fig. 6 Magnetic anisotropy induced by external stress. (a) The angle θ of the resultant saturation magnetization in magnetic materials involving magnetostriction coefficient (λ) under tensile stress (σ). Domain wall motion of a polycrystalline magnetic material under tensile stress with (b) positive K_σ ($\lambda_{si} > 0$, $\sigma > 0$) and (c) negative K_σ ($\lambda_{si} > 0$, $\sigma < 0$). (d) Corresponding magnetization curves of (b) iv (red) and (c) iv (blue) under an external magnetic field.

Table 1 Summary of various magnetic anisotropies

	Anisotropies in magnetic materials	Influencing factors	Origin of anisotropies	Energy equations
Intrinsic	Magnetocrystalline anisotropy	Crystal structures	Spin–orbit coupling	$E_{\text{crys, hexagon}} = K_0 + K_1 \sin^2\theta + K_2 \sin^4\theta + \ldots$ $E_{\text{crys, cubic}} = K_0 + K_1(\alpha_1{}^2\alpha_2{}^2 + \alpha_2{}^2\alpha_3{}^2 + \alpha_3{}^2\alpha_1{}^2) + K_2(\alpha_1{}^2\alpha_2{}^2\alpha_3{}^2) + \ldots$
Extrinsic	Shape anisotropy	Overall shape and aspect ratio	Demagnetizing field	$E_{\text{sh}} = \frac{1}{2}\mu_0 M^2(N_c \cos^2\theta + N_a \sin^2\theta)$
	Exchange anisotropy	Interfacial coupling between magnetic materials	Exchange interaction	$E_{\text{ex}} = -J_{\text{eb}} \cos(\theta_{\text{FM}} - \theta_{\text{AFM}})$
	Stress-induced anisotropy	External mechanical stress	Magnetoelastic effect	$E_{\text{me}} = K_\sigma \sin^2\theta$

fluctuations, resulting in decayed remanence and coercivity, as discussed in section 2.2. Therefore, the single-domain spin confinement of spherical MNPs presents challenges in maintaining ferromagnetism and achieving magnetic anisotropy. However, monodisperse MNPs with high magnetization values can achieve long-range ordering and transform into anisotropic MNPs *via* magnetic dipole–dipole interactions.[75] In addition to the magnetic dipole–dipole interactions, colloidal systems induce random agglomeration or clustering of monodisperse MNPs *via* physical interactions.[76] Magnetic anisotropy can considerably vary depending on the assembly processes and resulting chain orientations of MNPs. This variability in magnetic anisotropy expands the applicability for magnetic soft robots. Therefore, highly stabilized monodisperse MNPs are necessarily prepared because their arrangements can be appropriately controlled to prevent their random agglomeration.

Wet chemical synthesis of monodisperse MNPs provides many advantages such as controllability over the desired shape, size, and dimension of NPs and obtaining highly stabilized MNP dispersion by tailoring the solvents, additives, and capping surfactant. A variety of solution processing methods have been extensively employed for the synthesis of MNPs, including co-precipitation,[77] thermal decomposition,[78,79] and the solvothermal approach.[80] These well-established synthesis methods reliably produce high-quality and monodisperse MNPs. Nevertheless, the anisotropic assembly of MNPs has proved challenging owing to the weaker dipolar attractions when compared with thermal fluctuations or isotropic van der Waals interactions between MNPs.[76] Klokkenburg *et al.* discussed the potential for chain conformations in monodisperse MNPs, suggesting the requirement for magnetic dipole–dipole interactions more than that for thermal fluctuations.[75] As-synthesized magnetite NPs with a size of 21 nm obtained by thermal decomposition were successfully assembled into chain conformations in a ferrofluid. However, these assembled MNPs with the anisotropic geometry exhibited instability and disassociation, requiring further efforts to achieve prolonged stability in anisotropic chain conformations from the isotropic MNPs.

A straightforward approach to obtain sustainable and stable anisotropic configurations of isotropic MNPs involves one-dimensional (1D) template-assisted assembly. Correa-Duarte *et al.* used functionalized multi-wall carbon nanotubes (MWCNTs) as templates.[81] Layer-by-layer coating of poly (sodium 4-styrene sulfonate) (PSS) and poly(dimethyldiallylammonium chloride) (PDDA) on the MWCNT surface facilitated electrostatic interactions of positively charged MWCNTs with negatively charged γ-Fe_2O_3/Fe_3O_4 NPs (Fig. 7a). Since 1D MWCNTs served as templates for the anisotropic assembly of MNPs, γ-Fe_2O_3/Fe_3O_4 NP-decorated MWCNTs exhibited magnetic anisotropy and aligned in response to an external magnetic field (0.2 T, Fig. 7b). Fan *et al.* proposed an *in situ* attachment of MNPs to the surface of MWCNTs during the synthesis of MNPs *via* thermal decomposition.[82] Vacuum pumping during the thermal decomposition of the $Fe(CO)_5$ precursor afforded precise control over the size of the MNPs as

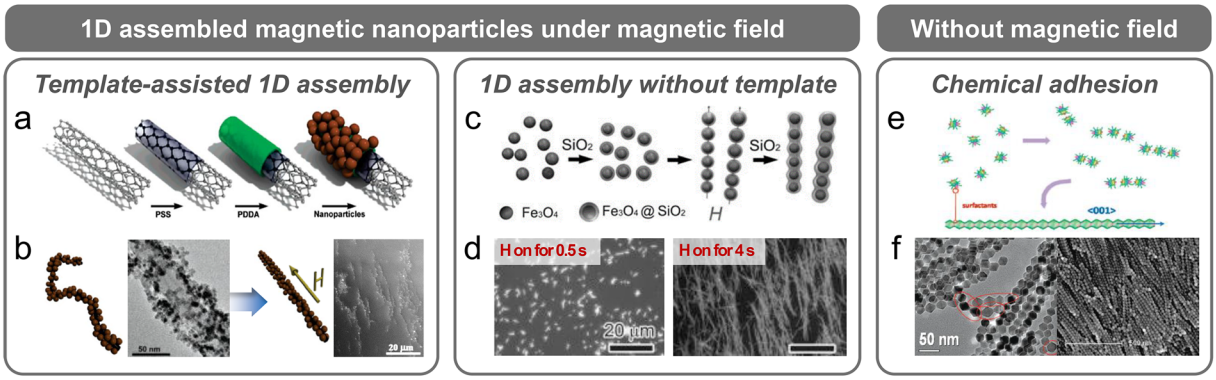

Fig. 7 Zero-dimensional MNPs and anisotropic assembly fabricated with various methods. (a) Template-assisted assembly of γ-Fe_2O_3/Fe_3O_4 on MWCNTs *via* layer-by-layer coating and (b) transmission electron microscopy (TEM) images of γ-Fe_2O_3/Fe_3O_4 compactly attached to an MWCNT and the alignment of γ-Fe_2O_3/Fe_3O_4 under a magnetic field of 0.2 T. The scale bars are 50 nm and 20 μm for the images on the left and right, respectively. Reproduced with permission.[81] Copyright 2005, American Chemical Society. (c) Anisotropic assembly of Fe_3O_4 achieved by applying an external magnetic field followed by fixation with a sol–gel reaction of silica and (d) variation in chain length by controlling the timing and duration of the magnetic field. The scale bar is 20 μm for both images. Reproduced with permission.[85] Copyright 2011, John Wiley and Sons. Anisotropic structure induced by chemical adhesion illustrated with (e) a mechanism indicating how the selective adhesion of organic surfactants leads to an α-Fe_2O_3 nanochain, and (f) TEM images showing the formation of a polyhedron particle by organic surfactants. The scale bars are 50 and 500 nm for the images on the left and right, respectively. Reproduced with permission.[90] Copyright 2010, American Chemical Society.

well as ensured a uniform attachment of MNPs to the MWCNT surfaces. Unlike the aforementioned methods based on the surface treatment of a template, a recent template-assisted assembly included the decoration of Fe_3O_4 NPs on MWCNTs without acid treatment. The mussel-inspired catechol chemistry enabled *in situ* attachment of Fe_3O_4 NPs to pristine MWCNTs *via* a co-precipitation process.[83]

However, in cases where the initially employed template becomes unnecessary in the system, its removal is challenging and requires a complex process. Thus, ongoing research aiming at anisotropic assembly of MNPs without templates is being conducted. An effective strategy for preparing a stable anisotropic assembly of MNPs without templates involves magnetic field-induced alignment, followed by immobilization of the aligned MNPs in a viscous polymer matrix. Sheparovych *et al.* fabricated magnetite nanowires (NWs) by aligning negatively charged superparamagnetic Fe_3O_4 NPs under a magnetic field, followed by the slow addition of a positively charged polyelectrolyte to preserve the alignment.[84] Hu *et al.* exploited a sol–gel reaction of silica to fix the anisotropic assembly of peapod-structured MNPs induced by an external magnetic field (Fig. 7c).[85] Notably, the morphology of the assembly could be finely tuned by regulating the periodicity and length of the assembly, which was determined by the size of the Fe_3O_4 NPs and the time for which the magnetic field was applied (Fig. 7d). Xiong *et al.* adopted polydopamine to lock the anisotropic assembly of Fe_3O_4 NPs induced by a magnetic field.[86] Dopamine can be uniformly deposited on various surfaces and subsequently transform into polydopamine *via* self-polymerization. This conformal polydopamine coating effectively confined the high-order arrangement of MNPs. As the polydopamine scaffold provided functional groups participating in secondary reactions such as Michael addition or Schiff base reaction,[87–89] this polydopamine-coated MNP assembly exhibited reactive functionalities under specific conditions for biosensing applications such as selective antibody capture and prevention of non-specific biofouling.

Under zero-field conditions, several organic compounds help in the fabrication of anisotropic assemblies of MNPs. Meng *et al.* fabricated a highly uniform α-Fe_2O_3 nanochain structure *via* selective adhesion of organic surfactants such as sodium oleate, oleylamine, and oleic acid (Fig. 7e).[90] This selective adhesion resulted in metastable polyhedron particles, where the cusp of particles were partially dissolved and bonded to adjacent particles, thereby minimizing the surface energy (Fig. 7f). To enhance the binding stability between particles, a covalent linkage between MNPs can be adopted in an anisotropic assembly. Nakata *et al.* introduced a binary mixture of immiscible molecules as shells for NPs, and these molecules were self-assembled on the NP shell, leading to a nano-worm structure.[91] To further secure the assembled structure, a molecular linker, 11-(10-carboxy-decyldisulfanyl)-undecanoic acid, was used to covalently bind NPs. This strong chemical bonding acted as the primary driving force for the anisotropic assembly of various MNPs, which is different from the magnetic dipole–dipole interaction. However, the chemical bonds that assist the assemblies might also form an undesirable random arrangement or bulk agglomeration of MNPs due to the absence of a guiding field.[92] To prevent the random attachment of MNPs, He *et al.* used maleic anhydride-grafted polypropylene (PP-*g*-MA), where MA functioned as a surfactant, whereas PP restricted the random aggregation of NPs.[93] Considering the co-existing conditions of attraction and repulsion, the weight ratio of PP-*g*-MA to the metal precursor should be optimized to form chain-like anisotropic assemblies of MNPs rather than a monodisperse or agglomerated MNPs.

3.2. Shape anisotropy of one-dimensional magnetic nanomaterials

Classic nanomaterials, such as nanorods (NRs), nanotubes (NTs), and NWs, characterized by morphological anisotropy demonstrate 1D structures with different length-to-diameter ratios. In cases of magnetic nanomaterials, which are typically crystalline, anisotropy occurs as a natural consequence of the intrinsic variations in interaction strengths among the constituent atomic or molecular building blocks along different directions.[94] Anisotropy in 1D magnetic nanomaterials provides a strong directional dependence in their magnetic properties, which is termed shape anisotropy, and notably increases the coercivity and remanence.[95–97] In this section, we investigate numerous methods with a specific focus on the preparation of single-crystalline 1D magnetic nanomaterials. Furthermore, we discuss the unique magnetic properties arising from the shape anisotropy inherent to single-crystalline 1D magnetic nanomaterials, which are distinct from those of the 1D assembled MNPs.[98]

Single-crystalline 1D iron oxides have been systematically investigated to exploit their high aspect ratio, leading to distinct magnetic properties because of the high shape anisotropy.[96,99] Template-mediated synthesis has yielded well-defined, monodisperse, and size-controlled 1D magnetic nanomaterials using both hard and soft templates, for instance, porous anodic aluminium oxide (AAO) and patterned block copolymer.[99,100] Although hard AAO templates have been extensively used to synthesize single-crystalline 1D β-FeOOH, which was further transformed to α-Fe_2O_3,[101] γ-Fe_2O_3,[99] and Fe_3O_4 [102] NWs *via* subsequent heat treatment, the resultant NWs exhibited quasi-1D characteristics and comprised small NPs. As mentioned earlier, classifying these quasi-1D nanostructures as assemblies of zero-dimensional (0D) NPs is more appropriate. The single-crystal growth of 1D nanostructured iron oxides has rarely been described because the corresponding mechanism is based on a "dissolution–reprecipitation" followed by dehydration.[103] However, Liu *et al.* demonstrated epitaxial growth of single-crystal magnetite NTs on a MgO core using pulsed laser deposition (Fig. 8a and b).[104] Using "bottlebrush-like block copolymers (BBCPs)" as soft templates, magnetite nanostructures with versatile anisotropic shapes were successfully synthesized.[100] Although the template-assisted method is advantageous for synthesizing precisely defined, monodisperse, and finely controlled 1D nanostructures, the post-treatment process required for template removal is challenging.

As alternative and straightforward approaches for the growth of 1D magnetic nanomaterials, template-free synthesis has been proposed for 1D anisotropic hematite (α-Fe_2O_3), maghemite (γ-Fe_2O_3), and magnetite (Fe_3O_4). These methods commonly involve anion absorption onto specific crystal planes,[105] the application of a magnetic field during the growth of magnetic nanomaterials,[106] and the use of complexing agents or ligands.[107] Jia *et al.* represented the synthesis of single-crystalline hematite and maghemite NTs. Hematite NTs were synthesized by a hydrothermal method using $NH_4H_2PO_4$, which resulted in hollow NT structures.[105] Phosphate ions supplied by $NH_4H_2PO_4$ preferentially adsorbed on the faces parallel to the c-axis of the hematite (Fig. 8c). This preference induced an anisotropic structure by restricting lateral growth (Fig. 8d).[108] However, an extended reaction at 220 °C led to dissolution or etching due to the acidic conditions. As a result, the (001) plane, which was less protected by phosphate ions, was more susceptible to dissolution and selectively dissolved, forming a unique NT morphology. Moreover, monodisperse maghemite NTs were synthesized *via* subsequent reduction and re-oxidation processes, but these methods exhibit limitations in increasing the aspect ratio. Wang *et al.* synthesized single-crystalline Fe_3O_4 NWs with a high aspect ratio (≈40) by applying an external magnetic field.[106] By varying the strength of the magnetic field using a permanent magnet positioned at the top and bottom of a Teflon-lined hydrothermal reactor, single-crystalline Fe_3O_4 with various shapes ranging from nanoplate to NW morphologies could be obtained (Fig. 8e and f). The single-crystalline Fe_3O_4 NWs were readily synthesized at a field strength of 0.35 T and grown along the direction corresponding to one of the magnetic easy axes.

The use of complexing agents or ligands enables the production of single-crystalline iron oxide NWs with a higher aspect ratio.[107] Xiong *et al.* synthesized maghemite NWs with an aspect ratio ≈ 150–300 in the presence of a complexing reagent, 1–10-phenanthroline. 1–10-Phenanthroline formed a stable complex with Fe^{2+}, namely, $[Fe(phen)_3]^{2+}$. Then, spontaneous oxidation of $[Fe(phen)_3]^{2+}$ to an octahedral-structured $[Fe(phen)_3]^{3+}$ caused the oriented growth of maghemite. With the progress of the reaction, $[Fe(phen)_3]^{3+}$ was first degraded to form $[Fe(phen)_2]^{3+}$, which demonstrated a two-dimensional (2D) structure exposing a bare *z*-direction without a complexing agent. Subsequently, growth primarily occurred along the *z*-direction, leading to NWs. Similarly, Palchoudhury *et al.* revealed that the ligand in the iron oleate complex could be selectively decomposed near 150 °C, as determined by density functional theory calculations and thermogravimetric analysis (Fig. 8g).[109] This decomposition behavior facilitated the directional growth of γ-Fe_2O_3 nanowhiskers with an ultrathin morphology (Fig. 8h).

Commercial permanent magnets, characterized by high coercivity and remanence, typically consist of alloys with rare-earth elements, due to their high magnetocrystalline anisotropy. Nevertheless, many researchers have tried to reduce the content of rare-earth elements and replace portions of them with 3d transition metals because of the supply problems of rare-earth metals and their thermal instability. Despite these efforts, magnetic materials fabricated solely from 3d transition metals have limited coercivity and remanence, owing to their limited magnetocrystalline anisotropy. In this context, introducing shape anisotropy into 3d transition metals presents an effective alternative. Among the 3d transition metals, Co has been frequently adopted because of its relatively high intrinsic magnetic anisotropy (*i.e.*, magnetocrystalline anisotropy), which further enhances the coercivity when combined with shape anisotropy. Although there are some technological and economic challenges in utilizing an-

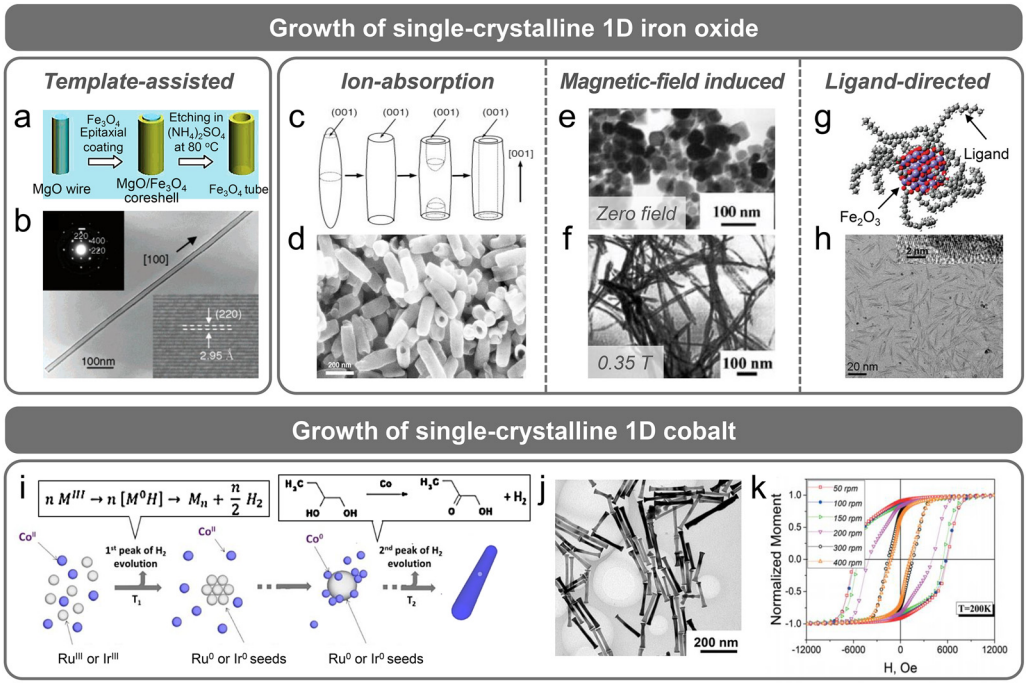

Fig. 8 Synthesis of single-crystal 1D magnetic nanomaterials. Template-assisted synthesis of (a) the epitaxial growth of Fe_3O_4 nanotubes (NTs) on a MgO core *via* pulsed laser deposition and (b) morphology of an Fe_3O_4 NT examined using TEM and the corresponding single crystallinity verified by selected area electron diffraction and high-resolution TEM (HR-TEM). The scale bar is 100 nm. Reproduced with permission.[104] Copyright 2005, American Chemical Society. Ion absorption during the synthesis of Fe_3O_4 NTs by (c) selective absorption of phosphate ions on the faces parallel to the c-axis for anisotropic growth of hematite NTs and (d) the anisotropic shape with an AR of 5–6 analyzed by scanning electron microscopy (SEM). The scale bar is 200 nm. Reproduced with permission.[105] Copyright 2005, John Wiley and Sons. (e and f) Magnetic-field-assisted growth of single-crystal Fe_3O_4 NWs during hydrothermal synthesis. (e) Square- or hexagonal-shaped Fe_3O_4 NPs were formed under zero-field conditions. (f) Fe_3O_4 NWs with a 20 nm diameter and 0.8 μm length were synthesized under 0.35 T. The scale bar is 100 nm for both (e) and (f). Reproduced with permission.[106] Copyright 2004, John Wiley and Sons. (g) Ligand-assisted synthesis of anisotropic Fe_2O_3 nanowhiskers. The selective decomposition of oleate ligands yielded ultrathin and anisotropic Fe_2O_3 nanowhiskers verified by (h) TEM and the single crystallinity of these nanowhiskers examined by HR-TEM. The scale bar is 20 nm. Reproduced with permission.[109] Copyright 2011, American Chemical Society. Synthesis of single-crystal Co NRs *via* (i) the polyol method. Reproduced with permission.[114] Copyright 2019, American Chemical Society. (j) Synthesized Co NRs showing an AR of 10 in the TEM image. Increasing the stirring rate during the synthesis of Co NRs caused stacking faults resulting in decreasing AR. The scale bar is 200 nm. (k) Magnetic hysteresis curves of Co NRs with different AR obtained at a controlled stirring rate during synthesis. Reproduced with permission.[115] Copyright 2017, The Royal Society of Chemistry.

isotropic Co for permanent magnet applications, there are advantages in soft robotic applications, which will be explained in section 4.2.2.

Dumestre *et al.* successfully synthesized Co NRs *via* the thermal decomposition of an organometallic complex, [Co(η^3-C_8H_{13})(η^4-C_8H_{12})], in anisole with ligands under a H_2 atmosphere.[110,111] The shapes of the synthesized particles were considerably influenced by the H_2 atmosphere and amount of ligands, while the organometallic complex ensured mono-dispersity. However, the preparation and reaction of such organometallic complexes always require a particular gas condition.[112] To be free from these strict requirements, Viau's group suggested the polyol method for the synthesis of Co NRs (Fig. 8i).[95] In this method, precursors in a reducing agent (1,2-butanediol) were transformed into a solid phase that served as a cation (Co^{2+}) reservoir for the gradual release of Co^{2+} in an alkaline solution. Controlled liberation of Co^{2+} from this cation reservoir allowed precise modulation of the growth rate of Co NRs on pre-existing Ru seeds *via* heterogeneous nucleation. Furthermore, the morphology of Co NRs was diversified by regulating several parameters such as the basicity of the solution, heating/stirring rate, and chain length of the Co precursor.[113–115] These Co NRs exhibited high remanence and coercivity in the longitudinal direction, and the further enhancement of magnetic properties could be controlled by modifying the aspect ratio (Fig. 8j and k).[116,117] Additionally, Co NRs demonstrated high thermal stability up to 525 K, which was higher than that of the predominantly used permanent magnet, NdFeB. However, owing to the large surface-to-volume ratio in the nanoscale range, Co NRs undergo frequent coalescence and oxidation, which causes a lower T_c than that of pure bulk Co (≈1300 K).[118]

3.3. Layered magnetic nanomaterials and exchange anisotropy

Numerous magnetic nanomaterials and nanostructures have been proposed to induce exchange anisotropy. Starting with core–shell MNPs,[44] a range of alloy and compound systems

including Laves phases,[119] Mn-based binary alloys,[120] and Heusler alloys[121] are being investigated.[122] In a core–shell NP system, an oxide shell is obtained by the oxidation and chemical surface treatment of NPs.[123] For example, when O_2 is diffused into a colloidal solution containing Co NPs, NPs with an average diameter of 9 nm are oxidized.[123] After undergoing a 4 days' oxidation process, the average diameters of the core and oxide shell were 3.7 and 3.1 nm, respectively (Fig. 9a). Then, when the magnetization was measured during field cooling from 5 to −5 T, a negative exchange bias of NPs occurred between the FM and AFM layers, where the temperature reduced from 300 to 3 K (Fig. 9b). However, oxidizing the surface of MNPs is challenging because of difficulties in controlling the uniformity of the core size and shell thickness. Therefore, the desired FM ratio is not achieved during the transition from the FM phase to the AFM phases. In this regard, an alternative approach is the *in situ* oxidation of magnetic nanoclusters during physical vapor deposition (PVD) under controlled O_2 gas flow conditions, which offers advantages such as fine-tuning of shell thickness and synthesis of monodisperse core–shell magnetic nanoclusters.[124–126] Otherwise, by implanting FM NPs into an AFM matrix or AFM NPs into an FM matrix, interfacial interaction is facilitated for exchange bias through the surface doping of MNPs.[127] For example, embedding of FI-$NiFe_2O_4$ NPs in an AFM-NiO matrix as a granular system, which is synthesized by high-temperature phase precipitation from an Fe-doped NiO matrix, leads to exchange bias resulting from the pinned ferri-clusters due to frozen spins in the spin-glass-like phase along the cooling-field direction.[128] However, interfacial complexities, irregular size, and a broad shape distribution result in limited homogeneity and reproducibility of exchange anisotropy in this type of particle–particle interlayer coupling.

Layered structures of 2D FM and AFM thin films hold a prominent position in the field of spintronic applications based on exchange bias. These layered 2D magnetic thin films provide relatively large-area controllability and easy-tuning of their geometry (dot,[129,130] ring,[131] stripe,[132,133] and wire[134]), which can be fabricated using various patterning processes including photolithography,[53] and electron beam lithography[130,131] for micro/nano-fabrication. Moreover, the sequential deposition of FM/AFM layers enables the adjustment of surface roughness,[135–137] layer thickness,[138–142] and interfacial lattice by regulating the crystallinity of each magnetic thin-film layer.[50,143]

Exchange anisotropy caused by interlayer coupling is highly dependent on the interfacial properties and surface roughness of the 2D magnetic thin films consisting of layered structures.[37,46] A rough and textured surface on 2D magnetic thin films contributes to the reduction of uncompensated spins at the interface within the layered structures, resulting in a decrease in interface magnetization and subsequent contraction of domains to lower the exchange anisotropy energy.[46,144] For example, Wu *et al.* highlighted the effect of surface roughness on the exchange bias field. The root mean square (RMS) roughness (3.7 Å) increased with an increase in the thicknesses (80 nm) of the AFM-CoO films (Fig. 9c).[144] As the CoO film thickness increased from 5 to 40 nm, the exchange bias field decreased from −350 to −90 Oe (plotted as red open squares in Fig. 9d) owing to the uncompensated spins at the interface. Dunz *et al.* investigated the influence of the interaction of a Ta/MnN/CoFeB system with a Ta buffer layer on the exchange bias in the system.[145] Thicker Ta layers led to a higher exchange bias field, because this approach improved the crystallinity of MnN and decreased N_2 diffusion during annealing. Thus, various approaches have been explored for

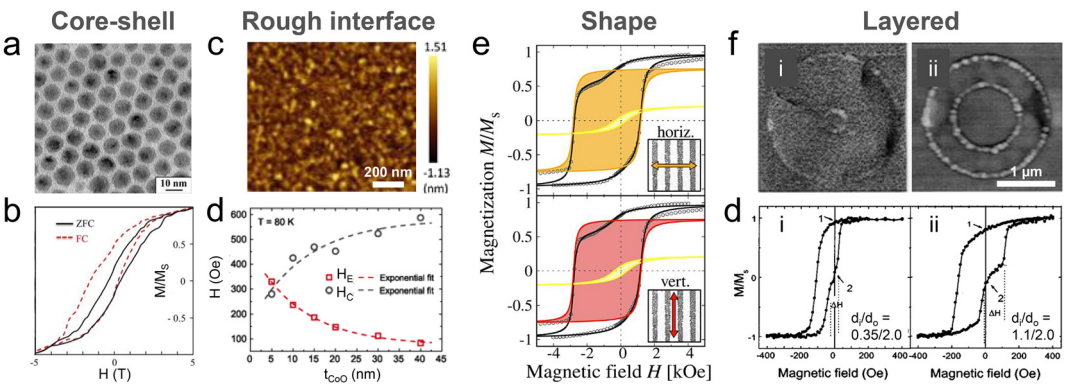

Fig. 9 Exchange anisotropy in magnetic interlayers and diverse structures. (a) Interface of Co/CoO core–shell NPs verified using a TEM image and (b) magnetization hysteresis curves exhibiting exchange bias with a red dashed line under field-cooling conditions (5 T with the temperature decreasing from 300 to 3 K). The black solid line represents magnetization hysteresis in the zero-field cooling state. Reproduced with permission.[123] Copyright 2023, Elsevier. (c) Atomic force microscopy images of CoO films with 80 nm thickness. (d) Dependence of the exchange bias field (H_{eb}) and coercive field (H_C) on the CoO thickness at 80 K. The exchange bias field decreases from −350 to −90 Oe with an increase in CoO film thickness from 5 to 40 nm. Reproduced with permission.[144] Copyright 2020, American Physical Society. (e) Exchange bias of the laser-patterned Co/CoO stripes. The upper and lower loops were measured under horizontal and vertical magnetic fields relative to the length direction of the stripes at 10 K, respectively. Reproduced with permission.[132] Copyright 2022, IOP Publishing. (f) SEM images of Ta (5 nm)/NiFe (20 nm)/IrMn (7 nm)/Ta (5 nm) rings with inner diameters of (i) 0.35 and (ii) 1.10, and an outer diameter of 2.0 μm. (g) Exchange bias of NiFe/IrMn rings measured at 300 K for each ring (i) and (ii) in (f). Reproduced with permission.[131] Copyright 2004, AIP Publishing.

the roughness control of growing materials, including the thickness control of the buffer layer,[135] annealing processes to form oxide layers,[136,137] and use of reactive ion-etched substrate.[135]

Layer thickness not only determines the characteristics of interfacial roughness, but also affects the exchange anisotropy associated with the domains of each layer. The layer thickness can be adjusted by controlling the deposition rate and time during PVD *via* sputtering or evaporation.[139–142] Meinert *et al.* examined the effect of a variation in the AFM-MnN layer thickness on exchange anisotropy.[141] The exchange bias field in the MnN/CoFe bilayer system increased up to a critical MnN layer thickness of approximately 30 nm, while an MnN layer thickness below 6 nm resulted in a zero exchange bias field. This ultrathin MnN–AFM layer (less than 6 nm) was attributed to spin instability and rendered the domain walls either unavailable or extremely small in the confined space.[146] Another reason is the temperature-blocking capability of the layered system that depends on the thickness of the AFM layer. With a decrease in the AFM layer thickness, the system loses the capacity to block external temperature variations. Thermal fluctuations destabilize the spins in the AFM layer, which affects the exchange anisotropy. This thickness-dependent change in exchange anisotropy is observed in the FM layer as well.[37,147,148] Thus, the most critical factor in interlayer coupling is regulating the thickness of both the AFM and FM layers with the formation of continuous films, rather than isolated island-like grains during deposition.

The crystal orientation in the interlayer region between 2D magnetic thin-film layers is also an important parameter in determining exchange anisotropy. Kohn *et al.* studied the exchange anisotropy of chemically ordered bcc Fe on $L1_2$-$IrMn_3$ and chemically disordered fcc γ-$IrMn_3$ on bcc Fe, grown *via* molecular-beam epitaxy (MBE).[143] The exchange bias field of $L1_2$-$IrMn_3$ was considerably greater than that of γ-$IrMn_3$ because of the strong exchange coupling between the Mn atoms and magnetic spins in the ordered crystal lattice. Thanks to the atomic-scale layer-by-layer growth with precise control of the substrate temperature and atom flux during MBE, each layer exhibits a specific plane direction that includes uncompensated spins. This approach was developed to establish crystalline compatibility between the magnetic interlayers. For instance, bilayers such as Fe_3O_4/NiO[149] and CoFe/MnIr[50] were fabricated using MBE to ensure a perfect alignment with a (001) crystalline plane at their interface. In addition, exchange anisotropy can be manipulated by tailoring deposition conditions and altering the deposition angle.[150,151] Controlling the deposition angle promotes the grain growth in the form of columnar structures, which enables the attainment of uniaxial anisotropy. The controlled aspect ratio of these columns and the resultant crystalline texture collectively contribute to the development of uniaxial anisotropy. Such anisotropy is influenced by both shape and magnetocrystalline anisotropies. For instance, in a study where a NiFe/IrMn bilayer was deposited at an oblique angle between 31° and 45°, the dominant factor contributing to uniaxial anisotropy was the combined effects of shape and magnetocrystalline anisotropy instead of the exchange anisotropy from interlayer coupling.[151]

As mentioned previously, conventional deposition and patterning processes are highly suitable for manufacturing layered structures in 2D magnetic thin films. This compatibility of fabrication allows for the customizing of shape and size, ranging from the submicron[129,130,132] to the nanometer scale,[152] in the development of high-performance spintronic devices including spin valve magnetic field sensors,[54,153] magnetic storage devices, and non-volatile magnetic random access memories.[55,154] Optimization of the geometry and size of patterned magnetic thin-film layers can boost the exchange bias field for spintronics applications.[129,155,156] When the dimensions of the patterned layout closely match the domain size of the magnetic layers, the exchange anisotropy energy in the interlayer may be diminished according to the domain state model.[157] However, designing patterned magnetic interlayers with small yet optimized sizes can increase the number of uncompensated spins per unit area, thereby strengthening the exchange anisotropy. Perzanowski *et al.* studied the relationship between patterns of magnetic thin-film layers and exchange bias.[132] The hysteresis curve of a striped pattern exhibited a bias of 0.8 kOe away from the center (Fig. 9e), which was higher than that of a flat film. When the dimensions of the patterns were reduced to those of a smaller rectangle, measuring 9.1 μm in length and 4.5 μm in width (SEM images in the inset of Fig. 9e), a larger exchange bias appeared under the vertical field as compared with that in the case of the horizontal field due to the demagnetizing field. This directional difference became more significant with a decrease in the size of the patterns. In contrast, the isotropic square pattern exhibited no difference in exchange bias field with respect to the direction of the applied magnetic field. Thus, high aspect ratio patterns with sizes in the range of several micrometers can exhibit a high exchange bias field. Moreover, the exchange bias field can be varied by modulating the interfacial contact between the magnetic layers. To explore this further, ring-patterned magnetic thin-film layers were designed with different inner and outer diameters (Fig. 9f).[131] Ring-patterned magnetic interlayers with a larger inner diameter exhibited a higher exchange bias field as compared with those of the interlayers with a smaller inner diameter, ascribed to the confinement of magnetic domains in the rings.

Layered structures of 2D magnetic thin films are beneficial for fine-tuning the interlayer properties with the goal of adjusting the exchange bias. However, several complexities associated with intermixing, defects, contamination, and lattice mismatches at the interface of bi- or multi-layered structures still exist. Although various comprehensive models have been proposed to explain the mechanisms of exchange anisotropy in different systems and materials, these models are insufficient to offer a complete interpretation of exchange anisotropy. Consequently, the effective management of key parameters, as discussed earlier, is imperative for attaining a reliable exchange anisotropy effect in customized systems and mag-

netic layers, ensuring the successful application of exchange-biased spintronic devices in practical implementations.

3.4. Synergistic dynamics of magnetic anisotropy in composites

Crystalline magnetic nanomaterials typically maintain a relatively stable magnetic anisotropy, unless severe changes in environmental conditions, such as heating/cooling, pressure, and strong magnetic fields, alter the free energy of the system.[158–160] However, ferromagnets, a distinct category of magnetic materials, either undergo dynamic transitions in their magnetic properties in response to mechanical tension or exhibit mechanical strain when subjected to applied magnetic fields.[161,162] This section covers three magnetomechanical effects: magnetostriction, magnetoelasticity, and magnetorheology, which are observed in FM materials when these materials are exposed to mechanical forces or when their magnetization states are altered by H_{ext} (Fig. 10a). FM crystals have an easy axis of magnetization, which is determined based on magnetocrystalline anisotropy.[163] When a magnetic field is applied along this easy axis, substantial shifts in the domain boundary and the rotation of magnetic domains within the crystals occur.[164] Deformation of materials takes place because of magnetic fields and is referred to as the magnetostrictive effect. A similar physical effect is known as the magnetorheological effect, in which the stiffness or modulus of a magnetic soft composite or fluidic system changes when an external magnetic field is applied.[165,166] The magnetorheological effect is induced by magnetic forces aligning magnetic nanomaterials within a viscous medium, thereby resisting mechanical deformation. This resistance originates from the dipole–dipole interactions between the magnetic nanomaterials, which are affected by an applied magnetic field.[8,167] As mentioned in section 2.4, the phenomenon in which magnetic properties change due to external forces is referred to as the magnetoelastic effect, which is opposite to the magnetostrictive effect. In the case of the magnetoelastic effect, the FM nature considerably affects the stress-induced magnetic anisotropy. Thus, the stress-induced magnetic anisotropy is dependent on other magnetic anisotropies in addition to external stress. The stress-induced response of magnetic properties in conjunction with the other magnetic anisotropies results in a substantial anisotropic response.[168] This synergistic anisotropy is also valid for magnetostriction and magnetorheological effects, inducing a remarkable mechanical deformation and strain in response to external fields. The behaviour of a magnetomechanical effect is of great importance for applications in both actuators and sensors.[59,169–171]

Since the discovery of the magnetostriction effect in Ni by Joule in 1842 and the giant magnetostriction effect in Fe or rare-earth-metal-based alloys by Clark and Belson in 1972, extensive studies have been conducted to synthesize materials with a high λ_{si}.[172,173] Single-crystal Terfenol-D ($Tb_{0.3}Dy_{0.7}Fe_2$), exhibiting an exceptionally high λ_{si} exceeding 1500 ppm owing to its intrinsic magnetocrystalline anisotropy, has found numerous applications such as in sensors, motors, and transducers.[174–177] However, a pre-magnetization process is required for domain alignment in polycrystalline Terfenol-D for an optimal magnetostriction effect.[178] To address this issue, various efforts aimed at enhancing the magnetic anisotropy in Terfenol-D *via* several techniques such as free-stand zone melting, modified Bridgman method, sintered powder compact, and mixing polymer matrix with Terfenol-D powder have been made.[179–182] Nevertheless, the ordering of

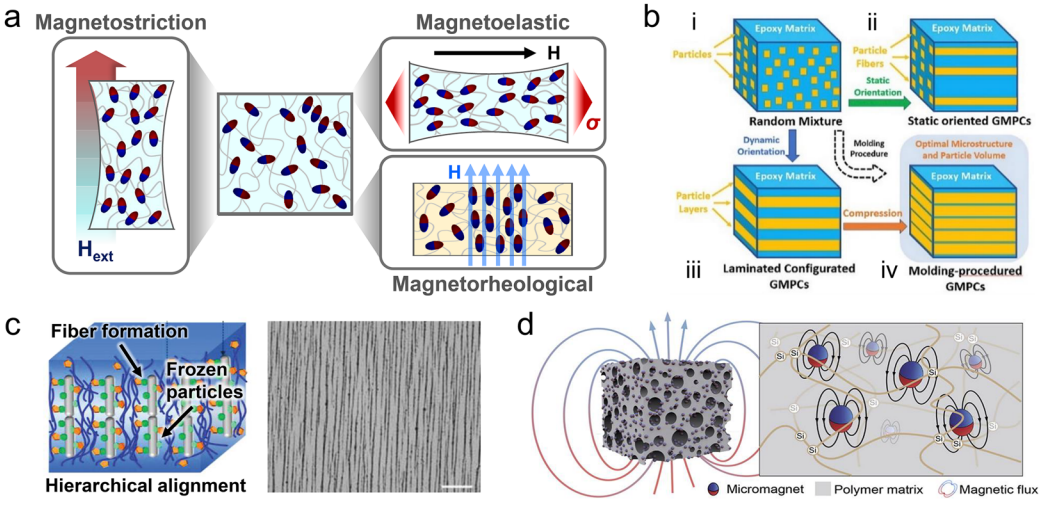

Fig. 10 Various magnetomechanical effects based on an anisotropic structure of composites. (a) Stress-induced magnetomechanical effects: magnetostriction, magnetoelastic, and magnetorheological effects. (b) Schematics of isotropic and alignment anisotropic structures: (i) random distribution, (ii) magnetostatic orientation and (iii and iv) routine for the two-step (magnetodynamic orientation and compression) formation of laminated-like structures of Tb–Dy–Fe particles. Reproduced with permission.[202] Copyright 2019, Elsevier. (c) Enhanced alignment of an anisotropic structure *via* a combination of magnetic fields and electrostatic interactions. The scale bar is 50 μm. Reproduced with permission.[205] Copyright 2022, John Wiley and Sons. (d) Giant magnetoelastic effect in a soft composite system. Reproduced with permission.[213] Copyright 2022, Elsevier.

polycrystalline Terfenol-D has limitations including the use of expensive elements Tb and Dy, the mechanical brittleness of the resulting materials, and processing challenges.

Oxide-based magnetic materials, such as polycrystalline cobalt ferrite, have emerged as alternatives to Terfenol-D because of their cost effectiveness, superior magnetomechanical coupling factors, and large deformative behaviors under low magnetic fields.[183,184] Unlike single-crystal magnetostrictive materials, polycrystalline magnetic materials comprise numerous grains with grain boundaries.[185,186] These grain boundaries serve as nucleation sites for stable-to-metastable phase transitions and domain switching triggered by an external field. Accordingly, grains with smaller sizes offer a larger number of nucleation sites, resulting in a more pronounced magnetostriction effect.[187] Bhame *et al.* investigated λ_{si} values across cobalt ferrite NPs with different grain sizes that were prepared by different methods, namely, combustion, reagent addition, coprecipitation, and calcination.[188] Cobalt ferrite NPs with grain sizes of 8 μm (combustion), 17 μm (reagent addition), 23 μm (coprecipitation), and larger than 25 μm (calcination) exhibit the maximum λ_{si} values of 197, 184, 159, and 135 parts per million (ppm), respectively. The enriched grain boundaries in the small-grained system induced large domain reversibility and increased the strain response to magnetostriction under low external fields. The λ_{si} value of polycrystalline cobalt ferrite depends on the uniform and smaller grain size. Therefore, the microstructures in polycrystalline cobalt ferrites should be controlled to achieve a high λ_{si}. Despite these efforts, polycrystalline cobalt ferrites still exhibit low λ_{si} values in the range of 130–200 ppm due to the different orientations of magnetic easy axes in the corresponding domains. Magnetic annealing facilitates the production of a higher λ_{si} and strain derivative based on a uniaxial anisotropic structure in the magnetic domains. Wang *et al.* determined the orientation of polycrystalline cobalt ferrite by applying a magnetic field during calcination.[189] A semisolid slurry containing Fe_2O_3 and Co_3O_4 powders in a polyvinyl alcohol solution was oriented under a strong magnetic field of 2 T. Thereafter, the mixture was sintered to produce $CoFe_2O_4$ with crystal grains of 30 μm oriented in the ⟨001⟩ direction, a relatively high λ_{si} of 270 ppm, and a strain derivative of 7.7×10^{-9} m A^{-1}.

Nevertheless, the inherent lack of ductility and mechanical resilience in bulk FM materials hinders their practical use in magnetomechanical applications requiring materials that can withstand repeated deformation.[190–192] To overcome this vulnerability, FM materials have been combined with soft polymer matrices aiming for more robust and improved mechanical properties.[193–195] To induce a magnetostrictive effect in these soft composite systems, the FM materials are randomly distributed in a polymer matrix *via* straightforward fabrication (Fig. 10b–i).[196] However, randomly-distributed ferromagnets lack magnetic anisotropy, leading to a low magnetostrictive effect.[197] In this case, the formation of an anisotropic geometry, composed of aligned FM particles in a fluidic or viscoelastic matrix, enhances the magnetostriction.[58] In a soft composite system, when the FM materials are sufficiently close to each other in an appropriate volume ratio, these materials can form an anisotropic structure in the direction of an external magnetic field.[198] Consequently, a strong magnetostrictive effect can be generated in the direction of the applied magnetic field. Both isotropic and anisotropic FM materials have been used for anisotropic aligning in a viscous polymer matrix.[182,199] A precise alignment of these FM materials commonly requires a fluidic medium that permits the free movement of FM materials while simultaneously guiding these materials under a magnetic field.[200,201] For example, Li *et al.* proposed a method where giant magnetostrictive materials comprising Tb–Dy–Fe were aligned in an epoxy polymer under a magnetic field of 1 T to induce magnetic anisotropy.[202] Tb–Dy–Fe particles were manufactured in the form of chain-like structures using a static magnetic field (Fig. 10b-ii), and laminate-like structures *via* a two-step process based on the combination of a dynamic magnetic field and compression (Fig. 10b-iii). Particularly, an anisotropic composite was produced using a two-step molding process (Fig. 10b-iv), resulting in an optimized microstructure characterized by high density and well-aligned particles. These magnetostrictive composites, which embedded anisotropically aligned FM materials, exhibited superior magnetomechanical properties compared with a random dispersion model. This enhancement in magnetic anisotropy results in a comparable λ_{si} of 1500 ppm to that of a single monolithic Terfenol-D, even with a particle volume fraction of as low as 57%.

The dimensions of FM materials with a relatively low λ_{si} values minimally change with respect to the applied magnetic field.[203] However, the anisotropic structure, achieved by the subtle reorientation of magnetized particles, demonstrates the capability to induce a macroscopic magnetostrictive effect, caused by the stretching of the matrix in the direction of the magnetic field.[198,204] Guan *et al.* reported a magnetostrictive effect in a soft composite system containing carbonyl iron particles (CIPs) mixed with silicone rubber.[193] CIPs are FM materials with fairly small λ_{si} values (lower than 10 ppm). However, when CIPs are magnetized under a magnetic field, magnetic interactions occur between particles, aligning these particles in the silicone rubber matrix. Consequently, subtle rearrangements of CIPs produce a magnetostrictive effect that allows stretching of the flexible silicone matrix, exhibiting strains of up to 184 ppm. When high-viscosity polymers lack co-solvents for dilution, the anisotropic alignment of magnetic materials in these polymers become challenging, and a strong magnetic field is needed to attain the desired morphology. Furthermore, additional driving forces are required to assist with alignment and freely construct a suitable configuration of magnetic materials. Chen *et al.* developed a magnetic soft composite in which negatively charged, magnetically responsive Fe_3O_4 NPs were vertically oriented in a biomimetic hydrogel (Fig. 10c).[205] Coupling of the magnetic field and electrostatic repulsion forces MNPs to vertically orient, even when magnetic fields as low as 20 mT are applied. Although Fe_3O_4 NPs demonstrate a relatively low λ_{si} value of approximately 40 ppm, the densely packed and highly anisotropic configur-

ation indicates their potential to exhibit a magnetostrictive effect.

Soft composite systems where a magnetorheological effect is induced can exhibit high stiffness under a magnetic field, and the magnitude of the reinforcement is influenced by the anisotropic nature.[206,207] By controlling the magnetic field during the curing of the matrix, either an isotropic or anisotropic structure is readily introduced, changing the magnetorheological properties.[208,209] Jung *et al.* fabricated two different types of isotropic and anisotropic structure by incorporating CIPs into natural rubber.[210] In the case of the anisotropic soft composite, CIPs were aligned in the direction of the applied magnetic field by applying an external magnetic field during the curing process. Although both isotropic and anisotropic composites represented a high modulus after magnetic field application, the anisotropic composite was higher than that of the isotropic composite, by nearly 60%. These results are attributed to the fact that the particle chains are aligned in a similar manner to that of rod-shaped fillers, resulting in a significantly high storage modulus.

The magnetoelastic effect, whose mechanism is opposite to that of magnetostriction, alters the magnetic properties of an FM material in response to external stress and is triggered by a variation in the magnetic domain. Kurita *et al.* fabricated a soft composite by randomly dispersing Fe–Co–V alloy particles in a polyurethane matrix, and magnetic flux changes were caused by the magnetoelastic effect.[211] The fabricated soft composite induced a magnetoelastic effect when subjected to a bending load. An approximately 0.05 mT change in magnetic flux was measured using a Hall sensor positioned at the bottom of the composite. However, variations in the magnetization of FM materials are limited due to the stress distribution in the soft matrix.[212,213] To overcome these limitations and enhance the magnetoelastic effect, the concept of the giant magnetoelastic effect was introduced (Fig. 10d). This effect includes a synergistic system of particle movement and rotation, along with changes in the magnetic domain of the FM material in the matrix. Zhou *et al.* reported a soft composite exhibiting a giant magnetoelastic effect based on a silicone elastomer matrix, which was embedded with both NdFeB hard magnets and Fe_3O_4 soft magnets.[213] In a composite system, magnetic particles with a single dipole configuration could form a unique distribution as "wavy-chains", even when a polymer and magnetic particles were homogeneously mixed. This was ascribed to the gradual decrease in polymerization degree from the polymer to the particle direction, where the monomeric solution near the FM nanomaterials was not fully polymerized. Therefore, mobile magnetic particles could still survive, and hence change direction and move in response to an applied magnetic field, even after the nanomaterial was solidified from a macroscopic view. Unlike the typical magnetoelastic effect, which is magnetic domain rearrangement for magnetic anisotropy, this magnetic soft composite introduced a different mechanism. In this system, stress led to a relative disordering of the initially well-aligned wavy-chain micromagnets. This disordering changed the magnetic anisotropy and magnetic flux density of the soft composite. Compared with the magnetoelastic behaviors of standalone ferromagnets, the remarkable change in magnetic anisotropy due to elastic deformation highlights the giant magnetoelastic effect. Through this giant magnetoelastic effect, the soft composite achieved high magnetic flux density variations of up to approximately 9 mT. These approaches to enhance magnetoelasticity introduce a new paradigm for the practical applications of magnetostrictive materials in sensing and actuating technologies.

4. Magnetic anisotropy for sensing and actuation in soft robotic applications

Numerous types of magnetic nanomaterial characterized by their magnetic anisotropy have been extensively studied owing to their substantial contributions to the development of both magnetic sensors and actuators. The inherent magnetization direction of these magnetic nanomaterials provides key benefits, including high selectivity, enhanced accuracy, operational efficiency, and customizability, to sensors and actuators in robotic manipulations.

In addition, magnetic sensors and actuators are appropriate for tracking motions and subsequently controlling the operations of robots with minimal physical contact in remote sites. Yet, achieving these capabilities with other types of sensor and actuator is quite challenging. The notable features of magnetic sensors and actuators based on magnetic anisotropy demonstrate widespread implications in various fields such as soft manufacturing grippers, rehabilitation robots, advanced prosthetics, human-interactive devices, and the Internet of Things. These contemporary electronic technologies necessitate ultrathin, lightweight, and form-factor-free designs that enable their compact integration and high compatibility with components having irregular shapes and surfaces. Specifically, sensing and actuating devices in the soft robotic systems should possess the capabilities to freely deform and effectively follow the dynamic motions of their pliable bodies to minimize disturbances. In this section, we discuss the numerous advantages of magnetic anisotropy in sensing and actuation. We also explore how magnetic materials can attain the desired softness and flexibility in magnetic sensors and actuators, particularly in the soft robotic applications.

4.1. Flexible and stretchable magnetic sensors

4.1.1. Magnetic proximity sensors. Magnetic field sensors are extensively used for position and gesture sensing in a wide range of fields, such as robotics, automobiles, industrial machinery, and consumer electronics. A notable advantage of magnetic field sensors is their touchless sensing capabilities, which enables motion sensors to be placed on any part of an object to interact with the targets. Contrary to conventional motion sensors such as accelerometers and gyroscopes, magnetic field sensors can be designed to be compact, miniatur-

ized, lightweight, ultra-thin, and ultra-flexible.[214,215] These design attributes significantly enhance the versatility of magnetic field sensors, facilitating their application to uneven surfaces and deformable objects. Particularly, integrating these flexible magnetic field sensors onto soft robotic bodies is promising for untethered robots and their unrestricted mobility.[216] Unlike hard-bodied robots that rely on predefined hinges between rigid components, soft-bodied robots mainly consist of elastic and compliant materials, enabling limitless deformation to various in-plane and out-of-plane angles without complex mechanical constraints. Due to the absence of stationary and motionless parts in soft robots, magnetic field sensors should be seamlessly integrated into the bodies of these robots to ensure conformal contact and tracking of robotic operations, for example, changes in displacement and orientation, and sensing the proximity of objects, without impeding movement or facing the risk of sensor delamination from the body. Flexible magnetic field sensors, which are based on metallic or semiconducting nanomaterials with magnetic or NM properties, allow highly selective field sensing regardless of mechanical deformation. They also enable ultra-sensitive motion detection through several sensing mechanisms and systems, such as the Hall effect, MR, and magnetoimpedance.[214,216] The performances of flexible magnetic field sensors are listed in Table 2.

Hall effect sensors. In fact, the Hall effect may not exhibit a significant correlation with the aforementioned properties of magnetic anisotropy. Nevertheless, it is worth discussing because of its traditional use in most proximity-sensing devices in industry and numerous consumer electronics. In a Hall sensor, a varying external magnetic field orients at right angles to the current flow in a thin-film conductor or semiconductor, generating a Hall voltage. This Hall voltage can be used to detect the presence and magnitude of the magnetic field, as illustrated in Fig. 11a.[217] Remarkable progress in the synthesis of 2D nanomaterials and their Hall coefficients has contributed to the development of ultra-thin, mechanically compliant, and field-sensitive Hall sensors (Fig. 11b). Semiconducting 2D bismuth thin films were directly grown and patterned into Hall cross-contact and sensor arrays on plastic substrates including polyimide (PI) and polyetheretherketone, which enabled Hall sensors to be placed on curved surfaces (Fig. 11c–i).[218] The flexible bismuth Hall sensor maintained its sensitivity even when subjected to bending stress, with a maximum bending radius of 6 mm (Fig. 11d). By attaching this sensor to the fingertips, magnetic field profiles could be monitored relative to the distance from the sensors on the finger to the magnet (Fig. 11c-ii).

Two-dimensional nanomaterials, particularly graphene, with its unique electronic properties and mechanical flexi-

Table 2 Performances of flexible magnetic field sensors

Types of magnetic sensors	Magnetic materials and device structures	Detection field limit (minimum/maximum)	Linear sensitivity	Flexibility (minimum bending radius/number of bending or stretching cycles/maximum strain)
Hall sensors	Hall cross, bismuth film[218]	—	−0.47, −2.29 V/AT	6 mm/50 cycles with a bending radius of 8 mm/1.25%
	Hall cross, laser-scribed graphene[219]	—	~1.12 V/AT	5 mm/1000 cycles with a bending radius of 5 mm/1.6%
Anomalous Hall sensors	Hall cross, Ta/Co/Pt[222]	—	500 μV kOe^{-1}	NA/NA/NA
AMR sensors	Barber pole, Ta/Py/Ta[226]	150 nT/0.2 mT	42 T^{-1}	5 mm/50 bending cycles with a radius of 5 mm /0.5%
	Barber pole, Py[229]	50 nT/—	0.54% mT^{-1}	150 μm/2000 cycles with a bending radius of 1 mm/1.33%
Printed AMR sensors	Printed Ta/Py microflake[244]	1 mT/400 mT	12% T^{-1} above 5 mT/190% T^{-1} below 5 mT	2 mm/NA/NA
GMR/GMR spin valve sensors	Stripe, Co/$[Co/Cu]_{50}$ and Py/$[Py/Cu]_{30}$[241]	—	—	3 μm/100% stretching for 1000 cycles/~270%
	Meander, $[Py/Cu]_{30}$[242]	—	—	2 mm/NA/NA
	Wrinkled, Ta/IrMn/[Py/CoFe]/Cu/[CoFe /Py][318]	1.2 mT/NA	0.8% Oe^{-1}	NA/10% stretching for 500 cycles/~29%
	Wheatstone bridge, Ta/[Py/CoFe]/Cu/[CoFe/Py]/IrMn[319]	2 mT/12 mT	—	30 μm/NA/4%
Printable GMR sensors	Printed $[Py/Cu]_{30}$ microflake[245]	1 mT/20 mT	0.43% mT^{-1}	16 μm/NA/100%
TMR sensors	Ta/Ru/Ta/NiFe/IrMn/CoFe/Ru/CoFeB/MgO /CoFeB/Ta/Ru[251]	—	—	5 mm/1000 cycles with a bending radius of 15 mm/NA
	Ta/Ru/Ta/CoFe/Ru/MgO/CoFeB/Ta/Ru[320]	—	—	NA/0.2% bending for 20 cycles and 0.4% bending for 20 cycles /~0.4%
	$[Ta/CuN]_6$/Ta/Ru/IrMn/CoFe/Ru/CoFeB/MgO /CoFeB/Ta/NiFe/Ru/IrMn/Ru/Ta/Ru[321]	—	250 μV Oe^{-1}	5 mm/NA/NA

1 Oe = 0.1 mT. Py = NiFe. Current normalized sensitivity = $V_H/(I_{bias} \times B)$ [V/AT].

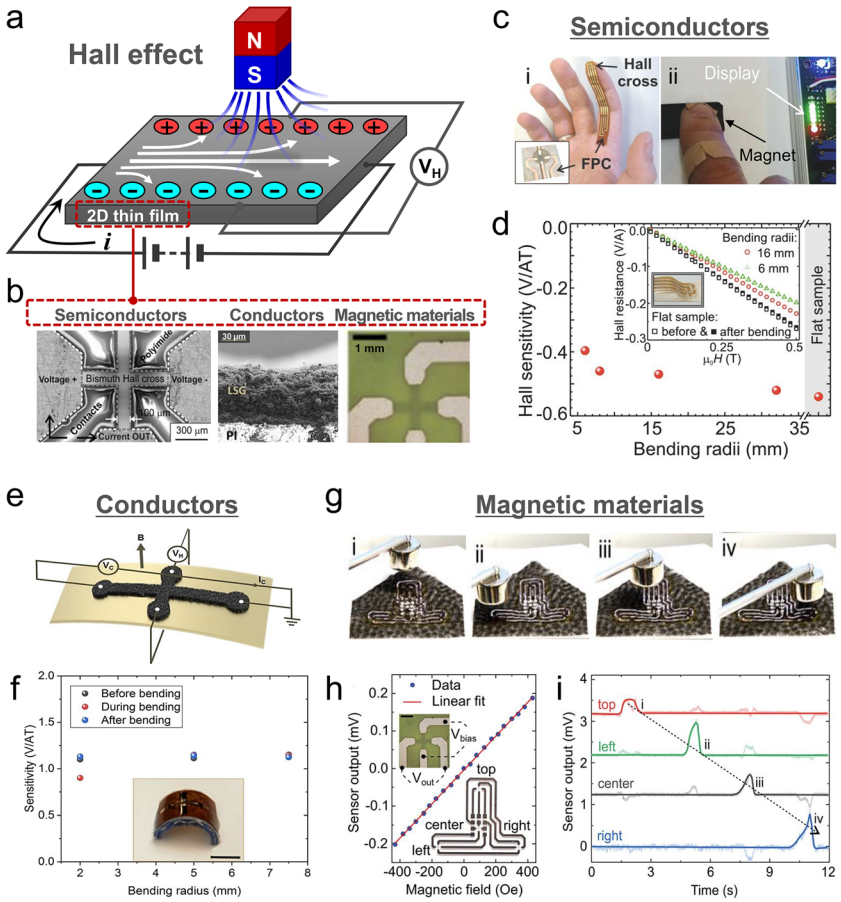

Fig. 11 Hall effect sensor. (a) Schematic of a traditional Hall effect sensor. (b) Components for a 2D thin-film Hall effect sensor, including semiconductors, conductors, and magnetic materials. (c) (i) Flexible printed circuit (FPC) with a bismuth Hall sensor applied to a curved finger. (ii) Real-time monitoring of magnetic field profiles relative to the distance from the Hall sensor on the fingertips to the magnet. (d) Hall sensitivity measured after bending the sensor at various radii, demonstrating consistent sensitivity of the sensor even after bending to a radius of 6 mm. Reproduced with permission.[218] Copyright 2014, John Wiley and Sons. (e) Illustration depicting the Hall measurement configuration of a laser-scribed graphene Hall sensor. (f) Sensitivity of the graphene Hall sensor at different bending radii. Reproduced under the Creative Commons CC BY License.[219] (g) Images of anomalous Hall sensors mounted on a soft magnetic origami actuator. The magnet approaches the Hall sensors on the soft magnetic origami actuator in the following order: (i) top, (ii) left, (iii) center, and (iv) right. (h) Linear voltage signal response to the external magnetic field and schematic of the four-Hall sensor connection. (i) The voltage output of the anomalous Hall sensors in response to the moving magnet with time. Reproduced under the Creative Commons CC BY License.[222]

bility, are promising for the development of flexible Hall sensors.[219,220] A graphene layer grown *via* chemical vapor deposition and subsequently transferred onto a 50 μm-thick Kapton film demonstrated a maximum voltage and current normalized sensitivities of 0.093 V/VT and 75 V/AT, respectively.[220] The sensitivity was stable even after the layer was bent 1000 times with a 5 mm bending radius. Laser-scribed graphene offers a simple and rapid maskless method for the fabrication of Hall crossbars on desired plastic substrates.[219] This method involves direct conversion of carbon-rich materials into graphene (Fig. 11e) which is capable of achieving high mechanical stability and a sensitivity of 1.12 V/AT even after being bent with a radius of up to 5 mm (Fig. 11f).

Regarding the enhancement of the Hall coefficient, magnetic nanomaterials offer an anomalous Hall effect (AHE) based on spin-dependent scattering of charge carriers. FM thin films characterized by magnetic anisotropy greatly influence AHEs by altering the path of electrons *via* interactions of electrons with the localized magnetic moments of the atoms in the FM material. Depending on whether the magnetic field is aligned parallel or perpendicular to the easy axis of magnetization in the FM material, it enables sensitivity adjustments, directional sensing, and performance tunability of AHE sensors for more versatile and effective field-sensing applications.[221] Ultra-thin AHE sensors have been proposed for conformal attachment to uneven polymeric surfaces through a series of fabrication processes comprising the deposition of metal-stacked layers with a sub-nanometer thickness onto a 3 μm-thick plastic foil (Fig. 11g).[222] Typically, 2D and monolithic Hall sensors measure the Hall voltage that occurs when a magnetic field is perpendicularly applied. However, this planar dimension limits the capability of these sensors to

detect changes in magnetic fields along all three spatial coordinate axes. To address this issue, flexible AHE sensor arrays were designed and firmly integrated onto 3D soft deformable composites. The compliant AHE sensor arrays exhibited a high linear sensitivity across a wide range of magnetic field variations, ranging from −400 to 400 Oe (Fig. 11h). The integrated AHE sensor on the three different deformable parts mapped the magnetic field profile with respect to the distance from the center of a fixed reference AHE sensor (Fig. 11g and i). Furthermore, these AHE sensor arrays did not interfere with the motions of magnetic soft actuators. Instead, these AHE sensors supervised the sequential shape-morphing process of actuators by monitoring the sensor output signals resulting from magnetic field changes.

In the case of MR sensors, the dominant influence of magnetic anisotropy leads to variations in the principles of magnetic field detection. These variations depend on the magnetism or magnetization of materials and device structures of the MR sensors. Thus, the extent of resistance changes and magnetic field sensitivity accordingly vary.[223] Three representative types of MR sensor are available in terms of device structures and their corresponding operational principles: anisotropic magnetoresistance (AMR), giant magnetoresistance (GMR), and tunnelling magnetoresistance (TMR) sensors.

Anisotropic magnetoresistance (AMR) sensors. First, the AMR effect is significantly dependent on magnetic anisotropy as it varies the electrical resistance of magnetic materials based on the angle between the current and magnetization directions, as illustrated in Fig. 12a. In most materials with positive AMR coefficients, the orientation of the electron orbitals is determined by the direction of the magnetic field originating from spin–orbit coupling. This phenomenon induces greater scattering of a transport electron as the current flows parallel to the applied field.[224] As a result, AMR sensors typically consist of thin-film magnetic materials with specific magnetic anisotropy to detect in-plane angular changes of an applied field. However, the straightforward design of AMR sensors exhibits several drawbacks, such as a near-zero sensing capability at low fields. Unlike magnetization, which easily aligns with the magnetic easy axis, guiding the current flow in the uniaxial direction relative to the magnetization direction requires a specific device geometry.[225] To ensure linearity in response to changes in the applied field, a barber pole structure is commonly designed to set the angle between the current flow and initial magnetization at 45°. Moreover, a Wheatstone bridge circuit is prevalently used to offset cancellation effects (Fig. 12b). The periodic barber poles on the AMR cells effectively guide the current at either 45 or 135° in alignment with the magnetic easy axis. This configuration exhibited a substantially linear response in terms of variations in output voltage when subjected to a magnetic field ranging from −200 to 200 μT.[226] This device structure guarantees that resistance changes are only caused by the magnetic field for improving field sensitivity, reducing thermal noise, and signal calibration and adjustment.[152,225–227] The flexible and highly sensitive AMR sensors could detect an extremely low stray field (81 μT)

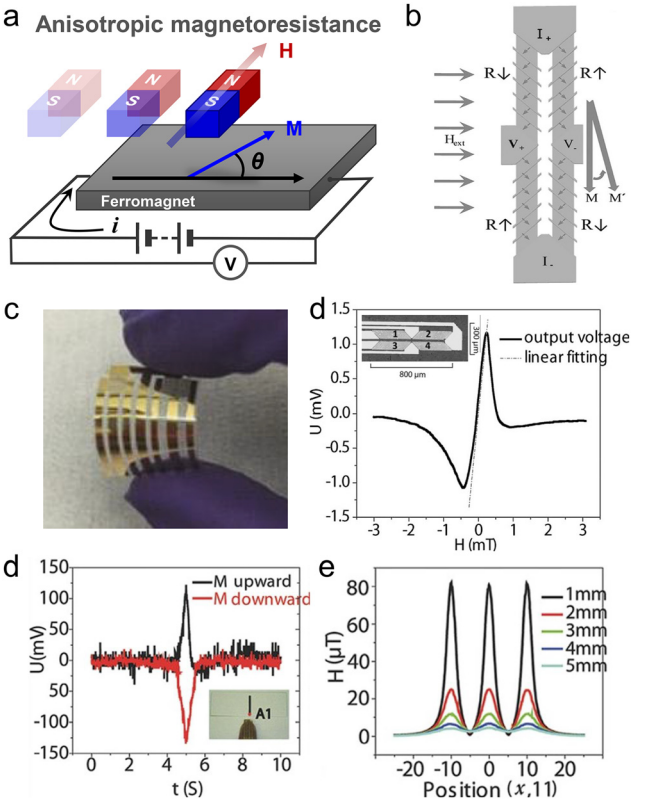

Fig. 12 Anisotropic magnetoresistance (AMR) sensor. (a) Schematic of AMR sensor, where θ is the angle between the current flow and the magnetization direction of the ferromagnet. (b) Illustration of the barber pole structures and Wheatstone bridge. Periodic barber poles with AMR cells effectively guided the current at either 45 or 135° in alignment with the magnetic easy axis. (c) Image of a flexible AMR sensor on PET foil. (d) Linear voltage response plotted against magnetic field. (e) Voltage output from the flexible AMR sensor on a finger. The magnetic field approached a single magnetic strip, with voltage changes corresponding to the initial upward or downward magnetization direction of the magnet. (f) Simulation results of the magnetic field profile measured at various distances from the top of the three magnetic strips. Reproduced with permission.[226] Copyright 2016, John Wiley and Sons.

from magnetic strips at a far distance (5 mm, Fig. 12c–f), rendering them suitable for safe and practical applications. Although the barber pole structure enhances the stability and linear sensitivity, challenges occur when dealing with a large area occupied by a complex pattern.[53] To address this issue, the AFM layer has been utilized to pin the magnetic moment of the FM layer, within the FM/AFM layered structure, to the predefined magnetization direction of the AFM layer through exchange coupling, thereby achieving self-biasing.[53,228] The initial magnetization direction of the FM layer was biased to 45° by optimizing the AFM layer thickness. Consequently, self-biased AMR sensors showed linear sensitivity without the barber pole structure. An ultra-thin AMR sensor consisting of 50 nm-thick FM stripes was developed by combining a Wheatstone bridge circuit with a barber pole structure to assist in thermal noise compensation and to linearize the sensor response.[229] This AMR sensor could perceive geomagnetic fields

as low as 50 μT and detect in-plane angular variations for an electronic compass, even when placed directly on curved skin.

Giant magnetoresistance (GMR) sensors. Unlike AMR sensors, GMR sensors with multilayered structures that consist of alternating FM and NM conductive nanomaterials have been proposed, as illustrated in Fig. 13a. The GMR effect significantly changes the electrical resistance compared with the case of the AMR effect due to the spin-dependent scattering mechanism. When the magnetization of these FM layers is parallel, electron scattering is minimized, leading to lower overall resistance (Fig. 13a-i). In contrast, a higher resistance is observed in the GMR multilayer when electron scattering increases owing to the antiparallel alignment of the magnetization in adjacent FM layers (Fig. 13a-ii).[230] The performance of GMR sensors is quantified using the GMR ratio, $(R_{AP} - R_P)/R_P$, where switching occurs with a shift in the magnetization configuration between the parallel and antiparallel states. R_{AP} and R_P represent the resistances for the antiparallel and parallel states, respectively. The field sensitivity of a GMR sensor is calculated as follows:[231]

$$S(H_{op}) = \left[\frac{1}{R}\frac{\partial R}{\partial H}\right]_{H=H_{op}} \quad (20)$$

where H_{op} is the operation field. Eqn (20) indicates that the field sensitivity relying on the GMR effect greatly increases with a significant change in resistance changes over a very narrow range of the external magnetic field. If the FM layer exhibits high coercivity because of magnetic anisotropy and interlayer interaction, the switching field will be higher, thus lowering the sensitivity of the GMR sensors. However, the uniaxial anisotropy in the FM layer is important for maintaining a stable magnetization direction minimizing susceptibility to external disturbances, and accomplishing a selective response to specific magnetic field directions. Therefore, multi-stacked FM layers with controlled magnetization have been fabricated *via* various methods such as positioning a permanent magnet during deposition,[232] magnetic post-annealing,[233,234] and application of external stress.[235]

The GMR ratio varies with the thickness of the FM and NM layers because of the oscillatory exchange coupling effect that can be described by both the Ruderman–Kittel–Kasuya–Yosida theory and quantum confinement effect.[236–240] Although stacking multi-layer films with FM and NM layers is necessary for achieving the GMR effect, each layer is still less than a few nanometers in thickness. Therefore, the multilayered yet ultrathin GMR sensors demonstrate not only high field sensitivity as compared with AMR sensors, but also conformal integration onto curved surfaces. Melzer *et al.* developed multilayered GMR sensors consisting of Py (1.5 nm)/[Py (1.5 nm)/Cu (2.3 nm)]$_{30}$ on a 1.4 μm-thick polyethylene terephthalate foil (Fig. 13b). These GMR sensors demonstrated remarkable resilience to repeated stretching even at 270% strain.[241] Laminating GMR sensors onto biaxially pre-stretched membranes led to the formation of surface wrinkle patterns driven by a large modulus mismatch between the sensors and membranes and imposed strain (Fig. 13c). The biaxial-wrinkled GMR sensors could be stretched in all lateral directions by applying an areal strain of up to 175% (Fig. 13d) without degradation of the GMR performance under multidimensional deformation. The resistance of the GMR sensor on the palm was monitored by adjusting the distance of the magnet from the sensor (Fig. 13e). The real-time monitoring of the magnetic sensor on the skin implied stable resistance with low noise and rapid resistance change over time. The imperceptible and stretchable GMR sensors on a fingertip also demonstrated proximity-sensing capability by monitoring resistance changes, irrespective of the distance of the permanent magnet, thereby activating a light-emitting diode (LED) light (Fig. 13f). Kondo *et al.* presented a novel active magnetosensory matrix (MSM) system comprising thin-film GMR sensor arrays integrated with a complementary organic thin-film transistor circuit on a 1.5 μm-thick parylene film.[242] The flexible MSM system based on an ultrathin plastic substrate with polymer encapsulation demonstrated excellent mechanical stability under severe loading and high surface compliance on uneven skin. The imperceptible and active MSM system performed low-voltage and high-speed operations with multiple integrated components enabling the real-time mapping of the magnetic field. An autonomous battery-powered system and a wireless communication module were incorporated into the MSM system to promote the practical application of the imperceptible MSM system in tracking the 2D magnetic field distribution for position sensing.

Typically, magnetic sensors consisting of rigid-metal thin films on a plastic foil have limited stretchability because of the difference between the Young's modulus of the metal and substrate. The use of ink composed of additives in an elastomeric binder for printing can solve this mechanical property mismatch. The minimal mismatch between the elastomeric substrate and viscoelastic ink results in a printed device that is stretchable and stable when deformed.[243] These advantages have led to recent proposals for printable magnetic sensors based on magnetoresistive paste.[244,245] A GMR sensor composed of Py/Cu multilayer flakes and a poly(styrene–butadiene–styrene) matrix was printed on an ultrathin plastic foil (Fig. 13g). This printed GMR sensor demonstrated high stability in terms of GMR performance (1.5%) and sensitivity (3.0 T^{-1}) under mechanical impact even with a bending radius of up to 16 μm.[245] Due to the surface-wrinkle formation on the pre-stretched substrates, the printed GMR sensors could be repeatedly stretched and released without degrading their magnetic field sensing performance (Fig. 13h). The key function of printed GMR sensors was magnetic field sensing regardless of the angular changes of the sensors (Fig. 13i), which allowed mounting of the sensors on any part of an object. Therefore, these compliant GMR sensors attached to the fingertip demonstrated the potential for augmented reality applications, where the virtual object is controlled by the remote and contactless detection of the magnetic field (Fig. 13j).

Linear sensing capability is important to sensors for predictable, accurate, and simplified data acquisition without

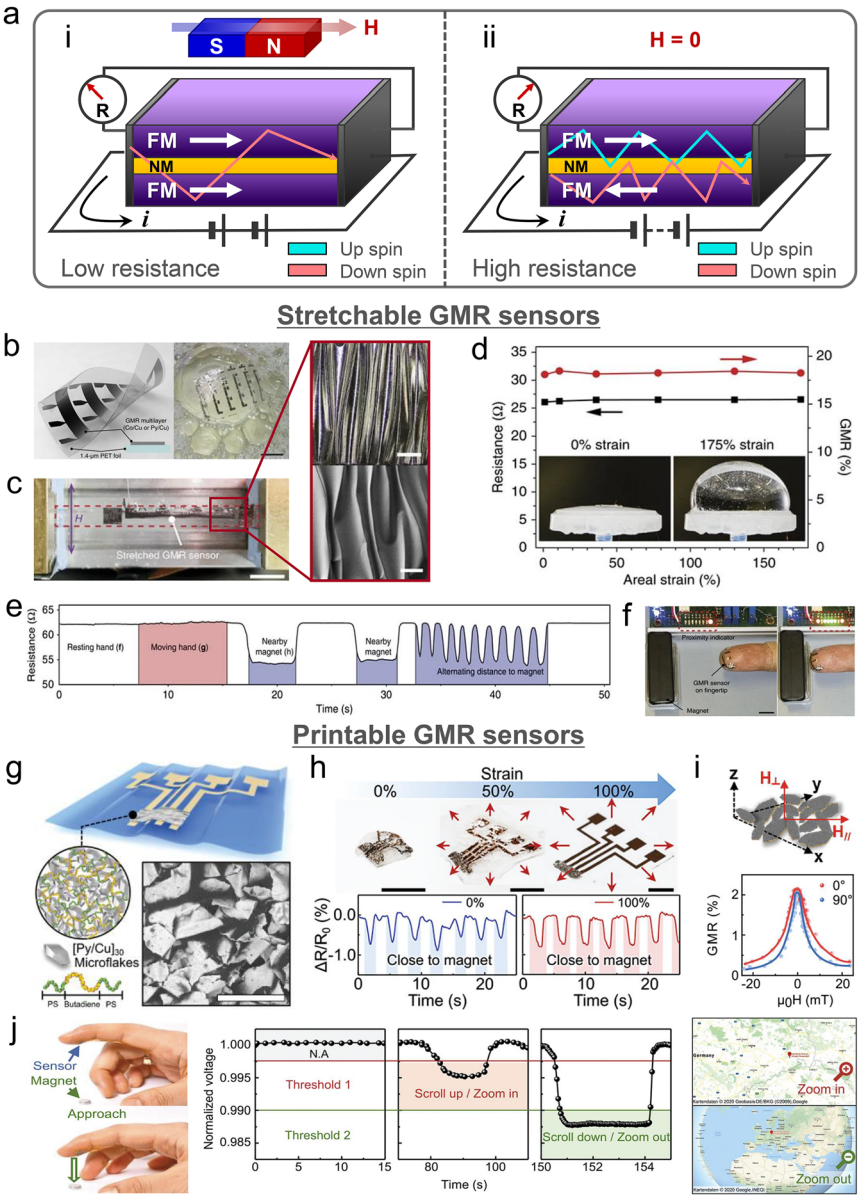

Fig. 13 Giant magnetoresistance (GMR) sensor. (a) Schematic of the GMR structure: (i) low-resistance state, where a larger magnetic field than antiFM coupling results in a parallel magnetization configuration, minimizing electron scattering. (ii) High-resistance state, where without an external magnetic field, the magnetization of the FM layers is anti-parallel due to the antiFM coupling, increasing electron scattering. (b–f) Stretchable GMR sensors. (b) Illustration (left) and image (right, scale bar: 10 mm) of the GMR sensor mounted on an ultrathin polyethylene terephthalate (PET) foil. (c) Uniaxial stretching test of the GMR sensor. The GMR sensor was attached to a pre-stretched elastomer substrate and compressed by 50%. Optical image (upper, scale bar: 200 μm) and SEM image (bottom, scale bar: 100 μm) of the wrinkled surface in a compressed state. (d) Resistance measured under various areal strains. The biaxial-wrinkled GMR sensors can be stretched in all lateral directions with an areal strain of up to 175%. (e) Real-time monitoring of resistance from the sensor on the palm by adjusting the distance of the magnet from the sensor. (f) Proximity sensing demonstration of a flexible GMR sensor on the fingertip. The LED light turns on when a permanent magnet is in close proximity. Scale bars: 10 mm. (b–f) are reproduced under the Creative Commons CC BY License.[241] (g–j) Printable GMR sensors. (g) Printed GMR sensor composed of Py/Cu multilayer flakes and a poly (styrene–butadiene-styrene) (SBS) matrix on an ultra-thin plastic foil. (h) Stretchability of the GMR sensor. Scale bar: 100 μm. Normalized resistance graph measured under 0 and 100% strain with an approaching magnet. (i) Schematic of the magnetic field direction for resistance measurement of random microflakes and the GMR graph. Random microflakes exhibit magnetic-field sensing capability regardless of the angular change of the sensors. Scale bar: 5 mm. (j) Demonstration of GMR sensor application for augmented reality. When the sensor attached to the finger is close to the magnet, the voltage drops. Below the threshold voltage 1/threshold voltage 2, the map was zoomed in/zoomed out. (g–j) are reproduced under the Creative Commons CC BY License.[244]

complex signal processing. The aforementioned AMR and GMR sensors cannot achieve linear sensitivity near the zero magnetic field range without the barber pole structure. Without the barber pole structure and 45° biasing, the resistance increases as the external magnetic field strengthens when the easy magnetization is aligned along the long or short

axis. Thus, the resistance becomes proportional to external magnetic fields, and weak external fields cause low sensitivity according to eqn (20).[53] Furthermore, the operation field is limited to the small coercive field of the AMR sensor.[223] Therefore, a strategy was proposed to modify the device structure by inserting pinning layers into the GMR multilayers, and the resulting device is known as a GMR spin valve device.[246] The basic structure of the GMR spin valve device comprises FM_1/NM/FM_2/AFM multi-stacked layers, as illustrated in Fig. 14a. In this configuration, the magnetization direction of the FM_2 layer is guided by the exchange anisotropy originating from the interaction between the AFM and FM_2 layers, as discussed in section 2.3. Notably, only the magnetization direction of the FM_1 layer readily undergoes rotation in response to an external magnetic field in the range of the effective anisotropy field. Once the field exceeds the anisotropy threshold, the FM_2 layer begins its rotation. As this switching behavior leads to a linear response of the MR sensor within a broad range of magnetic fields, several attempts can be made to adapt the multilayer-stacked GMR spin valve sensors. The GMR spin valve device was composed of a [Py/CoFe]/Cu/[CoFe/Py]/IrMn heterostructure and designed with two Wheatstone bridges and a well-defined magnetic anisotropy axis.[229] The inner and outer bridges included in the spin valve sensors that were reverse biased provided a bipolar sine output. The output signals were dependent on the angle between the direction of the applied magnetic field and the magnetic anisotropy of each bridge. Analysis of the arctangent correlation between the two output signals facilitated the real-time reconstruction of the in-plane magnetic field, where the permanent magnet continuously rotated around the spin valve sensor. Furthermore, the spin valve arrays were transferred onto an ultrathin PI foil and encapsulated by polydimethylsiloxane (PDMS). Positioning the GMR multilayers in a neutral plane enhanced the mechanical stability of these multilayers because the GMR multilayers were subjected to bending where both stress and strain were minimized. Thus, the GMR spin valve sensors were conformally attached to the skin and could detect the magnetic field orientation for the touchless manipulation of interactive devices such as a virtual keypad and virtual bulb.

However, the limitation of MR sensors is that they are only sensitive to the in-plane magnetic field. To address the need for measuring a more complex and 3D magnetic vector field, Becker *et al.* recently proposed a self-assembled GMR spin valve for 3D magnetic field vector angular encoders.[247] A self-assembly method transforms a planar structure into a 3D structure, offering a simpler fabrication process that is cost-effective as compared with the case of direct fabrication of the 3D design. The entire layer stack of the device is shown in Fig. 14b. The synthetic AFM (SAF) spin valve effectively cancels the stray field at the edges of the FM layers (Fig. 14b). After etching the sacrificial layer and inducing swelling of the hydrogel, the thin PI layer was rolled. Thus, four spin valve sensors were integrated into the 3D Swiss-roll structure. In the planar

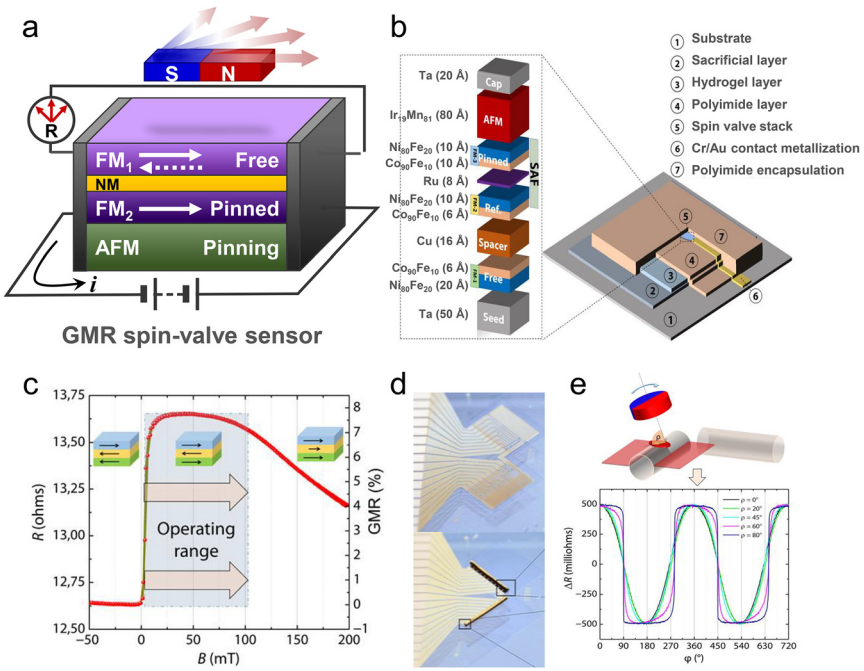

Fig. 14 GMR spin valve sensor. (a) Schematic of the spin valve structure. (b) Overview of the entire stack of the device and synthetic antiferromagnet (SAF) spin valve stack for the self-assembled 3D magnetic field vector angular encoder. (c) Resistance curve during a field sweep in the planar state. The operating range is between 5 and 50 mT, exclusively sensitive to the magnetic field direction. (d) Planar state of a device (upper image) and its transformation into a Swiss-roll structure (lower image). After transformation, the device contains two orthogonal tubes of 250 μm diameter and 8 spin valve sensors. (e) Graph depicting the angular dependence of resistance. ρ is the tile angle of the magnetic field plane with respect to the spin valve. Reproduced with permission.[247] Copyright 2019, AAAS.

state prior to transformation, the resistance curve was measured using a field sweep (Fig. 14c). The spin valve sensors exhibited a superior GMR ratio (~8%) and large plateau, indicating a constant resistance range. In this resistance range, the sensors were sensitive to the magnetic field direction rather than to the field strength, making them suitable for angle encoder applications. After transformation, the device contained two orthogonal tubes of 250 μm diameter and eight spin valve sensors (Fig. 14d). The dependence of the resistance on the angle is related to the variation of the tilt angle of the magnetic field plane with respect to the spin valve sensors (Fig. 14e). The results reveal that the sinusoidal angular response remained up to a tilt angle of 45°. After carefully designing the diameter of the Swiss roll, three pairs of spin valve sensors were placed in the two orthogonal tubes, with two sensors in each pair having 90° angular relationships of the pinning directions. This configuration allowed coverage of the 3D orthogonal planes (*XY*, *YX*, and *XZ*). Consequently, the self-assembled 3D magnetic field sensors detected any angular orientation of the magnetic field, magnetic field strength, and distance between the sensors and magnet.

Tunneling magnetoresistance (TMR) sensors. Magnetic field sensors based on the TMR effect are beneficial for detecting weak magnetic fields with high field sensitivity because of their significant MR ratios when compared with those of the AMR and GMR sensors, which are ascribed to the thin-insulating tunneling barrier. TMR devices comprise a magnetic tunnel junction (MTJ) with a FM/tunneling barrier/FM multilayered configuration, as illustrated in Fig. 15a. When two FM layers are parallel (Fig. 15a-i), more electrons tunnel through the layers than when the two FM layers are antiparallel (Fig. 15a-ii), resulting in a lower resistance. Similar to the case of a spin valve device, the magnetization direction of the FM layer is pinned with that of the AFM layer in an MTJ structure based on exchange anisotropy. Conversely, the adjacent FM layer can freely rotate in response to the magnetic field.[248] Controlling the magnetization direction of the pinned FM layer with a crossed configuration of the neighboring FM layer results in a linear response of resistance change to the external magnetic field. In an MTJ device structure, the crystalline tunnel barrier and an epitaxial interface between the FM and barrier layers are critical factors. For instance, the largest TMR ratio is 631% in CoFeB/MgO/CoFeB even without an AFM pinning layer at room temperature owing to the optimized sub-nanometer thickness CoFe and Mg, which led to enhanced interface crystallinity.[249] Such TMR devices that are capable of weak magnetic field sensing have been widely used in diverse applications including the read heads of hard disk drives,

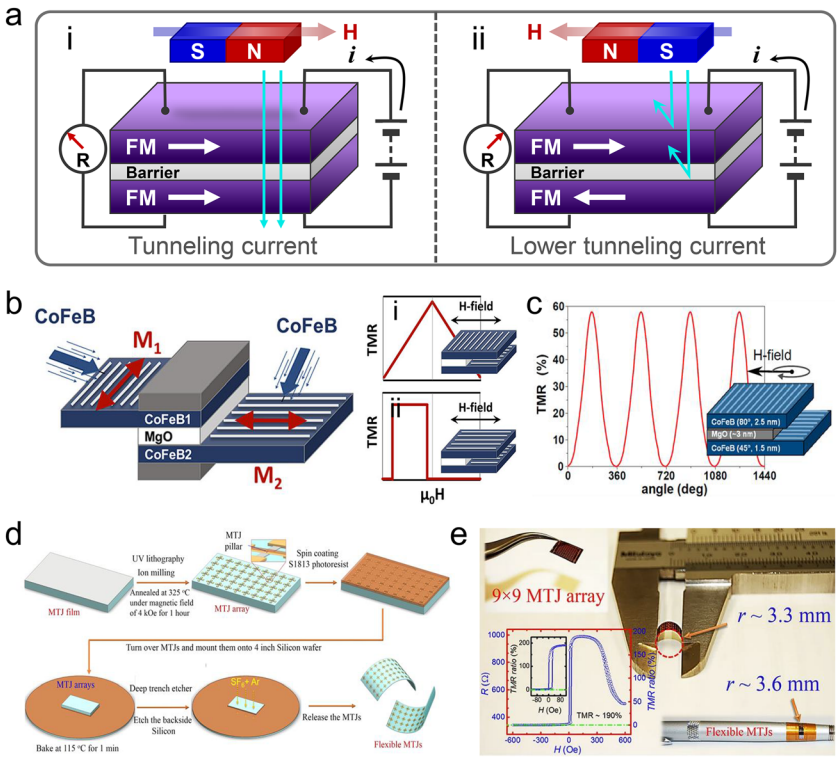

Fig. 15 Tunneling magnetoresistance (TMR) sensor. (a) Schematic of the TMR sensor, illustrating the difference between the tunnel current of parallel (i) and antiparallel (ii) states of the FM layer. (b) Schematic of the TMR sensor deposited using oblique incidence deposition with a periodic wave pattern is perpendicular to the deposition direction: (i) triangular-shaped TMR graph and (ii) square-shaped TMR graph. (c) Graph depicting the dependence of resistance on sinusoidal angle. Reproduced under the Creative Commons CC BY License.[252] (d) Schematic of flexible MgO barrier magnetic tunnel junction (MTJ) fabrication. (e) Flexible MTJs bent to a radius of 3.3 mm. The TMR graph in the inset shows that the unbent MTJ array demonstrates a TMR ratio of approximately 190%. Reproduced under the Creative Commons CC BY License.[251]

position measurements in industrial robots, and navigation of automotive systems. Willing *et al.* demonstrated new sensing functionalities of TMR devices with arbitrary intrinsic in-plane anisotropy in each CoFeB layer in the multi-stacked TMR layers formed using oblique-incidence deposition.[250] Oblique deposition with an angle of over 70° resulted in highly anisotropic surface roughness and periodic wavy patterns with wavefronts that were perpendicular to the deposition direction (Fig. 15b). The magnetization direction in thin magnetic layers was parallel to the wave-fronts, which was attributed to in-plane uniaxial magnetic anisotropy originating from shape anisotropy. In the configuration of this TMR device, when the uniaxial anisotropy directions of the two FM layers were perpendicular to each other, the TMR graph took on a triangular shape (Fig. 15b-i). Conversely, when two FM layers shared the same uniaxial anisotropy direction, the TMR graph demonstrated a square shape (Fig. 15b-ii). When the uniaxial anisotropy directions were perpendicular, the TMR response became sinusoidal with respect to the angle of the applied magnetic field (Fig. 15c). Therefore, the ability to manipulate the shape and the exchange anisotropy of the magnetic layers provides a method to customize TMR sensors for diverse applications, offering versatility in sensor design and performance optimization. The remarkable field-sensing capability of the TMR sensor also holds substantial potential for perceiving minute biological magnetic signals. However, the development of TMR devices has primarily focused on improving the MR ratio, and limited efforts have been directed toward the flexibility of these devices.

Although oxide barriers, such as MgO, are primarily fabricated *via* PVD, MBE, and atomic layer deposition, the achievement of defect-free, pinhole-free high-quality sub-nanometer oxide barriers still requires high state-of-the-art thin-film technology, which is an expensive and complicated process. Moreover, the fabrication of TMR sensors requires a high-temperature annealing process for the oxidation of the barrier growth, post-annealing for CoFeB crystallization, and pinning of the AFM layer by inducing exchange anisotropy. Commonly used polymer substrates to be applied for thin-film device fabrication have a limited working temperature range and exhibit a relatively higher roughness than those deposited on to Si wafers due to prevention of the growth of high-quality single crystals. Therefore, Chen *et al.* suggested an alternative for developing flexible TMR sensors by using the transfer method (Fig. 15d).[251] It was a sequential fabrication process with the following steps: deposition of magnetic and NM layers on a Si wafer, patterning on the Si wafer, post-annealing for CoFeB crystallization, and magnetic annealing for exchange bias. After finishing the conventional process, the back of the Si wafer was etched, resulting in the only thin MTJ film that could be transferred to a flexible substrate. This flexible MTJ with the MgO barrier demonstrated complete functions with a TMR ratio of approximately 190% before bending. The flexible MTJ could be bent at a radius as small as 3.3 mm without damage (Fig. 15e).

The aforementioned magnetic field sensors exhibit the advantage of maintaining their magnetic performance under bending conditions, making them effective for measuring proximity on curved surfaces. However, MR sensors composed of magnetostrictive materials are affected by stress if they are not engineered in a neutral plane. When subjected to stress, the magnetic domains are aligned by the magnetoelastic effect, and the magnetic anisotropy direction of the FM layer changes. It modifies the angular relationship of external magnetic fields with the easy magnetization direction and induces a change in the resistance output. This resistance variation can be used to determine the strain magnitude or direction with respect to the initial resistance. When the GMR spin valve sensor with positive magnetostrictive $Co_{50}Fe_{50}$ in the free layer is subjected to tensile stress, the anisotropy field increases in the direction of the strain.[252] Due to the anisotropy field, the stress increases the coercive field in the magnetization hysteresis curve, and the increasing trend is saturated at 12% strain. Moreover, Ota *et al.* performed comprehensive research by measuring the magnitude and direction of strain using a Co/Cu/NiFe GMR strip.[253] The bottom NiFe layer was in the single-domain state as the assisting external magnetic field exhibited insensitivity to stress. However, the upper Co layer was strain sensitive. This flexible GMR sensor fabricated on a polyethylene naphthalate sheet showed a resistance change depending on the strain direction and easy magnetization direction angle, confirming the possibility of realizing strain direction sensing using the GMR sensor. FeB-based MTJ as a free layer was designed to integrate spintronics strain gauge sensors with a microelectromechanical systems microphone.[254] The magnetization of FeB undergoes rotation in response to both tensile and compressive strains, with a drastic change in the resistance owing to the high λ_{si} of FeB.[255] This MTJ also features a high TMR ratio of 190%, resulting in a high strain gauge factor ($(\Delta R/R)/\Delta\varepsilon$ = 5072). Consequently, a series-connected strain gauge array can promptly respond to diaphragm vibratory motions, even at high frequencies of up to 1 kHz.

4.1.2. Magnetoelastic touch sensors. Proximity and touch sensors serve distinct purposes and each of them offers unique advantages. Proximity sensors are particularly useful in scenarios where touch input is either undesirable or impractical, such as in sterile environments.[256,257] In contrast, touch sensors provide a tactile and intuitive means for users to interact with electronic devices and for a more precise detection of stimuli.[258–260] Thus, combining both proximity and touch sensing capabilities results in excellent functionalities and greater accuracy in the field of electronics and feedback-controlled robots. Previously, we have introduced the various types of flexible magnetic field sensor that can verify magnetic field changes and thus acquire proximity information. In this section, we explore the magnetic sensors based on touch-sensitive approaches using a magnetoelastic effect.

Touch sensors based on piezoresistive, triboelectric, capacitive, and piezoelectric effects have been extensively examined in various fields due to their distinctive signal generation mechanisms.[261–266] However, their sensitivity to moisture restricts their application as wearable or implantable sensors

in specific environments, such as high-humidity conditions and human skin.[267,268] Moreover, touch sensors based on triboelectric and piezoelectric effects rely on the alignment of electric dipoles (capacitive conduction) caused by dielectric polarization at the material interface, thus exhibiting low current densities and high impedance values, leading to high signal-to-noise ratios.[269,270] In contrast, the magnetic field, which activates a touch sensor using the magnetoelastic effect, remains consistent regardless of moisture and the sensors can operate stably in a wet environment without additional post-processing, including encapsulation. Simultaneously, magnetoelastic-based sensors form an alternating alignment of magnetic dipoles both on and inside the material, which allows them to achieve low impedance.[213,271] Magnetoelastic touch sensors exhibit a wide sensing range that is 10 times broader than that of other types of sensor and responds to stimulation ranging from subtle pressure at a low level to intense pressure at a very high level.[272]

An anisotropic arrangement of magnetic materials in a polymeric matrix is a common feature of magnetoelastic materials. Thus, the touch perception based on the magnetoelastic effect is achieved by detecting the variations in magnetic flux resulting from changes in the net magnetization moment of magnetoelastic materials during mechanical impacts and deformation. For example, in a macroscopic aspect, magnetoelastic composites with an anisotropic arrangement of magnetic particles embedded into the polymers alter the magnetic flux density by disordering the arrangement of magnetic particles under external mechanical stress. At the atomic level, the magnetic domains rotate and move because of the mechanical impact. To reduce the magnetic potential energy, the magnetic moment deviates from the original direction and even jumps to another easy axis created by stress. Thus, the applied pressure varies the magnetic flux density, which can be converted into electrical signals *via* electromagnetic induction. Zhao *et al.* proposed stretchable and self-powered biomonitoring sensors by coupling the giant magnetoelastic effect with electromagnetic induction (Fig. 16a).[272] As the well-oriented micromagnet wavy chains in the polymer matrix were disrupted because of mechanical deformation, the rearrangement of the magnetic chains significantly affected the difference in magnetic flux, which is termed the giant magnetoelastic effect (Fig. 16a-i). The maximum magnetomechanical coupling factor caused by the giant magnetoelastic effect was 4.16×10^{-8} TPa^{-1} (Fig. 16b), which was approximately 3.3 times greater than that of Fe–Co alloys. The variations in magnetic flux induced electric currents within coil-type liquid metal microfibers (Fig. 16a-ii). The fully soft platform combining the giant magnetoelastic composites and electromagnetic coils exhibited high mechanical endurance with a lateral strain of up to 440% and could be worn on all body parts to monitor the different bio-mechanical signals (Fig. 16c). In addition,

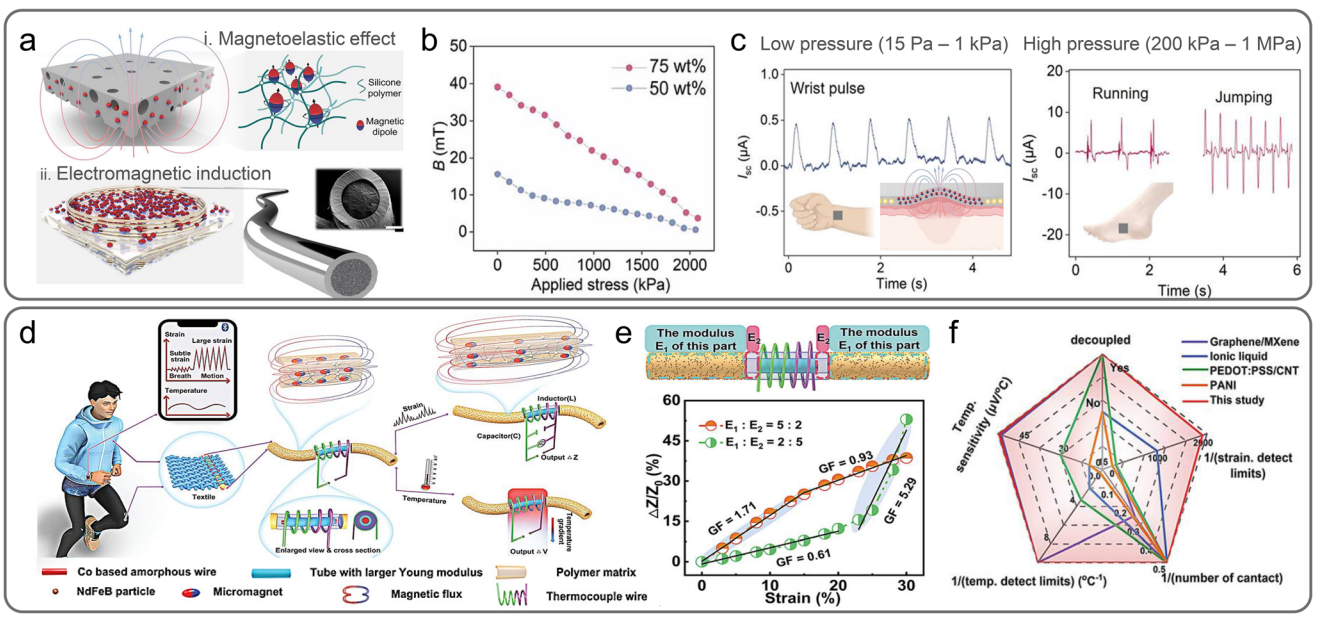

Fig. 16 Biomonitoring sensor utilizing the giant magnetoelastic effect. (a) Schematic of the self-powered biomonitoring sensor based on the combination of the (i) giant magnetoelastic effect and (ii) magnetic induction effect, and the internal structure of each component. (b) Magnetic flux density variations of the sensor under different pressures. (c) Output current induced by low-pressure (wrist pulse) and high-pressure (running and jumping) motions with representative diagrams. Reproduced with permission.[272] Copyright 2022, American Chemical Society. (d) Schematic of a wearable strain and temperature sensitive dual-mode sensor (STDMS) capable of accurately detecting strain and temperature changes. (e) Schematic of the heterogeneous structure of STDMS and change of relative impedance when strain is applied to the STDMS ($E_1 : E_2 = 2 : 5$ (green symbols) and $E_1 : E_2 = 5 : 2$ (orange symbols)). E_1 and E_2 represent the Young's modulus of magnetic composites and non-magnetic cylinders, respectively. The slope of the linear fit is the gauge factor (GF). (f) Comparison of the performance of this sensor with those of other various dual-mode sensors. Reproduced with permission.[277] Copyright 2023, John Wiley and Sons.

electromagnetic induction endows the sensors with self-powered operation without a power supply for the prolonged operation of implantable bio-monitoring devices and untethered robots.

For intelligent behaviors of robots, the ability to distinguish various stimuli is essential. Sensors in soft robots whose abilities are equivalent to the multi-functional sensing of human skin have been developed based on the concept of multimodal sensors.[273,274] The combination of magnetic sensors with other types of sensing approach has also been suggested to enhance the accuracy, reliability, and functionality of the sensors.[275,276] Xiao *et al.* demonstrated a multimodal sensor combining the giant magnetoelastic and thermoelectric effects (Fig. 16d).[277] The multimodal sensor was constructed by wrapping a CuNi-Cu (CNC) thermocouple coil around a magnetoelastic composite in which NdFeB particles were embedded in PDMS. The outputs of the CNC thermocouple coil changed the magnetic flux of the magnetoelastic composite under the applied strain, which was verified by a change in impedance (Fig. 16e). Simultaneously, with a change in temperature, the output voltage varied because of the Seebeck effect caused by the temperature difference between the CuNi and Cu. Therefore, the fabricated textile-type multimodal sensor could detect both strain and temperature gradients, which revealed magnetic field variations of 30 mT under a 30% strain and an output voltage of 2.997 mV in response to a change in temperature from room temperature to 55 °C. Fig. 16f depicts a comparison between the performances of this sensor and various other dual-mode sensors, specifically focusing on the interference-free output for two different stimuli. The strain- and temperature-sensitive dual-mode sensor (STDMS) with a tubular heterogeneous structure detects strain based on the temperature-dependent magnetic field variation and the permeability of Co-based amorphous wires (CoAWs). With an increase in temperature, the remanence of the STDMS originating from strain change was stable, and the permeability of the CoAWs was retained when the temperature was decreased from 100 °C to room temperature. Similarly, the voltage measured by the STDMS thermocouple remained unaffected by the mechanical strain occurring in the wires, and the wires exhibited an identical thermoelectric effect. As a result, the STDMS achieved excellent strain and temperature sensing performances, clearly decoupled the input signals and avoided crosstalk.

For tracking the touch trajectory, magnetoelastic composite-based pressure sensors integrated with Hall sensors were used as multimodal sensing devices.[258] Hu *et al.* demonstrated a wireless magnetic tactile sensor capable of transmitting information about the position and area where external forces were applied (Fig. 17a).[278] The integration of Hall sensors with force-sensitive magnetic sensors based on the giant magnetoelastic effect enabled the detection of both the applied force and proximity of the magnetic field. The magnetoelastic composite consisted of permanent NdFeB magnetic particles embedded in a silicone elastomer, which was magnetized in numerous directions to achieve different magnetic flux densities in the x, y, and z directions (Fig. 17b). The difference in the magnetic flux density was monitored in a touchless manner using a Hall sensor located underneath the magnetoelastic composites. Both the tactile and proximity sensing data provided a specific magnetization profile using a clustering k-nearest neighbors algorithm model. The acquired sensing signals were pre-decoded to confirm different contact forces and changes in the magnetic field along the z-direction at 36 to 10 000 points, which offered insights into the contact points and corresponding magnitudes for the dexterous and remote manipulation of robots (Fig. 17c). Liu *et al.* demonstrated a bimodal flexible sensor based on the combination of triboelectricity and the giant magnetoelastic effect, which facilitated touch and touchless sensing according to two distinct modes (Fig. 17d and e).[279] In the touchless mode, as a negatively charged external object approaches the magnetoelastic conductive film, potential generation was induced from the charge generation based on contact electrification. Therefore, free electrons flow from the magnetoelastic conductive film to the ground, yielding current. However, when the magnetoelastic conductive film came into contact with an external object, the film underwent deformation because of contact pressure (Fig. 17e). During mechanical deformation, the micromagnet chain structure in the film changed, and thus reduced the surface magnetic flux density (Fig. 17f). Simultaneously, the electromagnetic induction effect caused a liquid metal coil to generate a current that corresponded to changes in the magnetic flux density. A sensor mounted on a soft robotic hand obtained signals regarding the surface roughness of the object, by sliding the robotic hand over the surface of the object and scanning the shape in a non-contact mode (Fig. 17g). The system also included a convolutional neural network (CNN) model that was pre-trained using the distinct electrical signals generated by the triboelectric effect, which depended on the shape of the object. Furthermore, when the robotic hand slid on the surface of objects with different roughnesses, the magnetic flux change caused by the magnetoelastic effect was converted into an electrical signal *via* electromagnetic induction. The CNN was also pre-trained using the different electrical signals generated according to the surface roughness. Consequently, the object was recognized by combining the electrical signals acquired as the robotic hand approached a specific material and slid on its surface. The combination of these two sensing modes (Fig. 17h-i and ii), coupled with a CNN model, resulted in a sensor with superior sensitivity and high accuracy (Fig. 17h-iii). These findings highlight the potential of soft electronic systems in response to multiple stimuli and are used for the development of intelligent magnetoelastic devices, which are essential for object recognition and discrimination.

4.2. Magnetic soft actuators

Soft actuators have great importance for qualifying key parameters of locomotion, manipulation, and safety in soft robotics, which mimics the dexterity and adaptability of natural organisms.[4,280,281] Unlike traditional electrical, pneu-

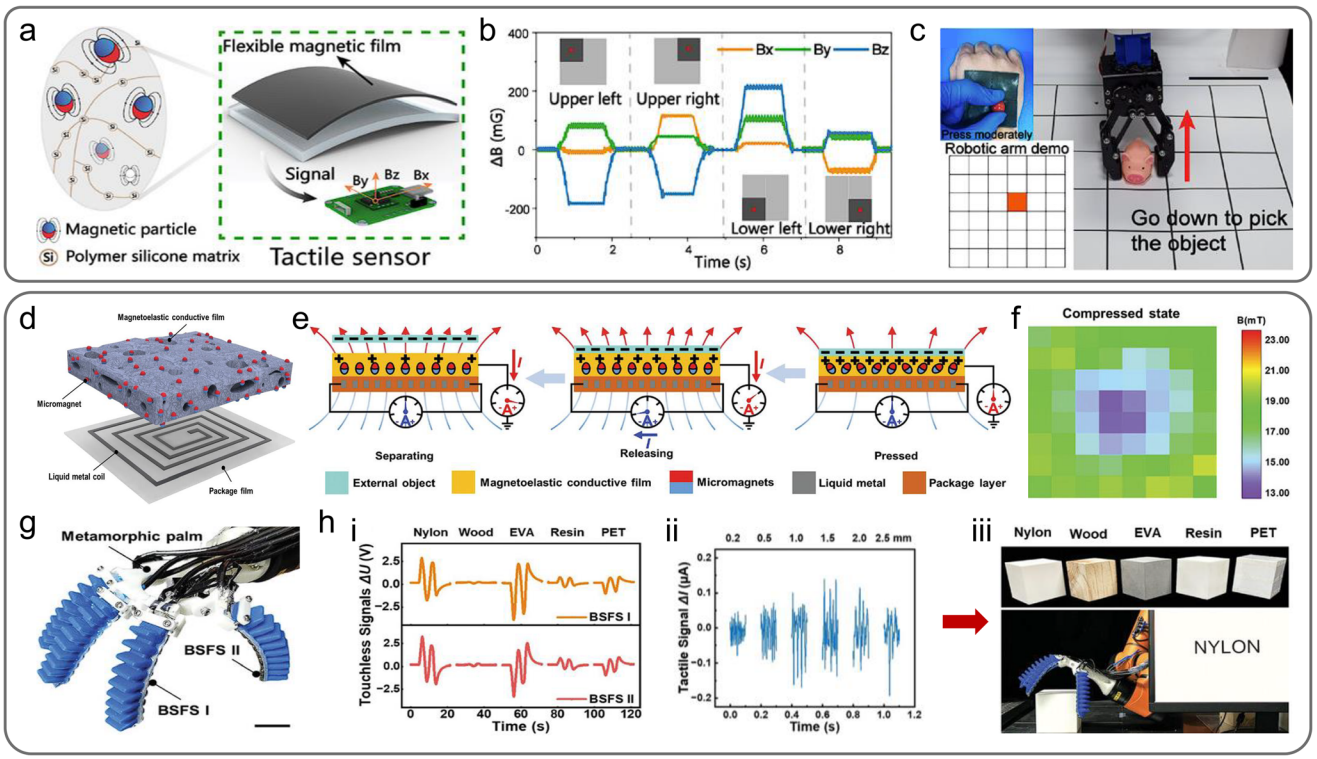

Fig. 17 Multifunctional sensor based on the giant magnetoelastic effect. (a) Configuration of a wireless flexible magnetic tactile sensor (FMTS) with its internal structure, and the directions of the magnetic flux density signals (B_x, B_y, and B_z). The left inset image exhibits the distribution of magnetic particles (red and blue spheres) in the polymer matrix (orange lines). (b) Various magnetic flux density signals generated in the *x*, *y*, and *z* directions upon touching different regions of a "symmetrical up and down" magnetized FMTS. (c) Demonstration of a real-time remotely operated robotic arm control system based on the FMTS. Reproduced with permission.[278] Copyright 2022, American Chemical Society. (d) Components of a bimodal self-powered flexible sensor (BSFS): a packaged liquid metal coil and a magnetoelastic conductive film. (e) Operating mechanism based on the triboelectric and giant magnetoelastic effects of the BSFS. (f) Variation of magnetic flux density mappings under pressure in a soft magnetoelastic film. (g) Schematic of a flexible robotic hand equipped with a BSFS. The scale bar is 3 cm. (h) Demonstration of an intelligent robotic system capable of sensing and describing various objects. (i) Triboelectric output signals, (ii) giant magnetoelastic output signals, and (iii) an image of a robotic hand recognizing various objects. A total of five materials are included: nylon, wood, ethylene vinyl acetate (EVA), photosensitive resin, and polyethylene terephthalate (PET). Reproduced with permission.[279] Copyright 2023, John Wiley and Sons.

matic, or hydraulic motor-mounted robots, soft actuators facilitate dynamic motion and enable robots to navigate through intricate and unpredictable environments. Owing to their high compliancy, soft actuators can conform to irregular shapes and handle fragile items for delicate manipulation. Moreover, compatible soft actuators can accommodate variations in the environments with good adaptability and minimize the risk of damage when the robots come into contact and interact with humans or soft objects. Considering their significant importance, a lot of strategies have been proposed for soft actuators using stimuli-responsive soft materials that are activated by heat,[282] humidity,[283] pH,[284] electric field,[285,286] and magnetic field.[287,288] Among these stimuli-responsive materials, magnetic field-responsive soft materials offer many advantages such as remote manipulation of actuators, fast response time, and versatility for operation across a wide range of environments, even in water.[289,290] Forces that trigger the mechanical responses of magnetic soft composites can be classified into translational force, magnetostriction effect, and torque. However, the translational force and magnetostriction exhibit some limitations in application for magnetic actuators. Translational force is referred to as a mechanical source that causes spatial movements of magnetic materials under a gradient magnetic field. Although the strength of the force is relatively high, it rarely induces deformation of a matrix, thus resulting in limited freedom of magnetic actuators. Magnetostriction in magnetic soft composites changes in the dimensions of the material under a uniform magnetic field due to the magnetostrictive properties of the filler or its tendency to be aligned along the magnetic field. However, magnetostriction cannot generate a large deformation as the unit of strain is typically measured in ppm, as presented in section 3.4. Meanwhile, the magnetic torque that induces the rotation of magnetic materials under a uniform magnetic field causes a large deformation. The deformation can be finely tuned by programming magnetic anisotropy resulting in a complex shape-morphing capability. In this section, we review the recent advances in magnetic soft actuators achieved by manipulating magnetic anisotropy to control the deformation of magnetic soft composites based on the torque.

4.2.1. Rare-earth magnet-based soft composites for high degrees of freedom of actuation. The classical approach to induce motion in magnetic soft actuators involves embedding magnets in deformable elastomers. Typically, the embedded magnets are randomly dispersed in the elastomers for ease of process and to ensure equivalent magnetic properties throughout the composites. However, complex shape morphing is challenging in the presence of randomly distributed magnets in the elastomers as this composite experiences a simultaneous and mono-functional response to an applied magnetic field.[291] To overcome this lack of controllability, elastomers are substituted with stimulus-responsive polymers that offer one or more additional functionalities.[292] These highly functionalized magnetic composites can alter their behaviors in response to a combination of two or more stimuli, thereby providing diversity and enabling complex actuations. To achieve a selective response and controllable actuation with bi-functional switching properties, Ha *et al.* suggested magnetic composites comprising NdFeB microparticles embedded in a thermo-responsive shape memory polymer that could modulate its elastic modulus according to changes in the surrounding temperature and a pre-programmed magnetization state (Fig. 18a).[222] The control of bi-functional actuation in this context relied on both magnetic fields and light. Embedded NdFeB micro-particles exhibited responsiveness to magnetic fields, while simultaneously converting light energy into heat through the photothermal effect. Therefore, the thermo-responsive shape memory polymer selectively adjusted its elastic modulus in a specific area, thereby allowing control of part of the composite by both illumination and an applied magnetic field. Specifically, magnetic origami could modulate sequential shape morphing based on a position-sensing feedback system (Fig. 18b). The supervised and localized activation facilitated reconfigurable origami actuation, which could decide the actuation sequence and successfully execute a mission only guided by light and a magnetic field without hinges and pre-defined structures (Fig. 18c). However, complex manipulation of actuation and shape morphing to transform

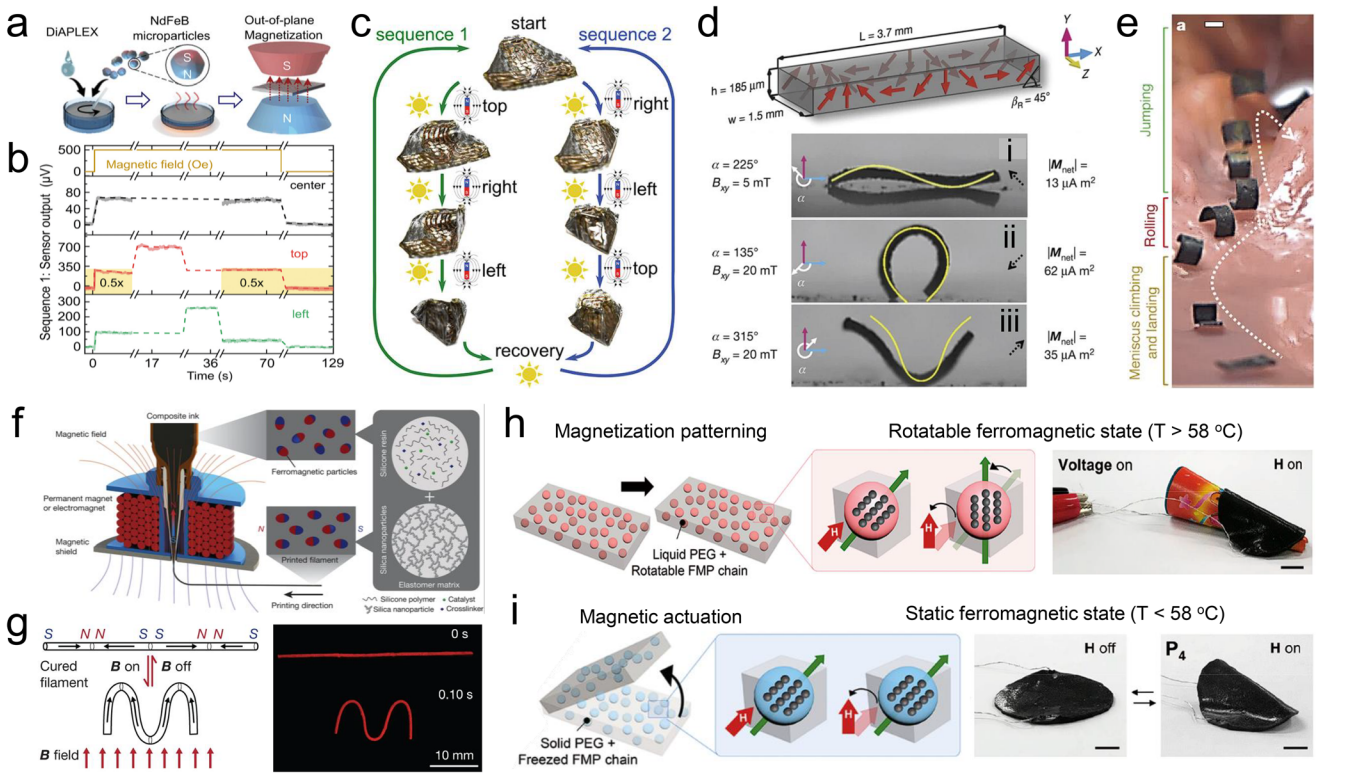

Fig. 18 Magnetic soft actuators with rare-earth magnet-based soft composite. Reconfigurable soft origami actuator with responsiveness to light and magnetic field fabricated by (a) mixing a shape memory polymer with NdFeB particles followed by out-of-plane magnetization, (b) position sensing capability by integrating a flexible anomalous Hall effect sensor into the soft composite, and (c) localized actuation without hinges by light and magnetic field. Reproduced with permission.[222] Copyright, the Creative Commons CC BY License. Small-scale magnetic soft actuator with (d) the harmonic magnetization profile enabling (i) sine-shape, (ii) C-curve, (iii) V-shape deformations by modulating the strength and direction of the magnetic field and (e) locomotion in an artificial stomach. Reproduced with permission.[294] Copyright 2018, Springer Nature. (f) 3D printing method to encode a complex magnetization profile with pre-magnetized NdFeB particles and (g) a simple filament case showing how the generated magnetization profile makes a deformation under an external magnetic field. Reproduced with permission.[288] Copyright 2018, Springer Nature. (h) Reprogrammable magnetic moment above the T_m owing to the mobility in medium (left) and encoding magnetization profile simply by wrapping the soft composite around a certain object during magnetization (right). (i) Fixing oriented magnetic moments by cooling under T_m (left) and reproduction of the shape of the wrapped object under an external magnetic field resulting from the programmed magnetic profile (right). Reproduced with permission.[296] Copyright 2020, American Chemical Society.

the desired morphologies remains difficulty owing to the lack of directional control.

To enhance DoFs and controllable actuation, strategies to assign directionality have been studied by varying the magnetization states of soft magnetic materials.[293,294] Hu *et al.* proposed small, untethered, and soft bodies composed of NdFeB microparticles embedded in a silicone elastomer and programmed a harmonic magnetization profile by simply wrapping these soft composites around a cylinder (Fig. 18d).[294] The programmed soft robot was controlled using a time-varying magnetic field to realize different locomotion modes. According to the magnetization direction of the soft bodies with respect to the strength and orientation of the applied field, these magnetic soft composites could be deformed into various structures and complex transformation like a sinewave shape, C-curve or V-shape (Fig. 18d-i, d-ii, and d-iii). This complex 3D shape morphing can propel magnetic soft bodies for forward movement, which can be applied to a magnetic swimmer in underwater conditions. The soft robot demonstrates its potential in navigating across unstructured and moist environments by executing a series of movements to explore a surgical stomach phantom (Fig. 18e).

In the aforementioned studies, magnetic nanomaterials are typically dispersed randomly in solidified polymer matrices, thereby lacking the alignment of their magnetic easy axes. Therefore, the net magnetic moment in the direction of magnetization tends to be relatively modest when the external magnetic field is removed, attributed to the diminished remanence. To enhance the net magnetic moment, the magnetic easy axis should be oriented along the magnetization direction. Thus, the re-orientation of pre-magnetized magnetic fillers has been proposed before the magnets are fixed within a polymer matrix. The pre-magnetization of magnets along their magnetic easy axes is easily conducted to maximize the net magnetic moment because magnets are suspended in a viscous polymer solution with high mobility during the curing process.[295] Kim *et al.* demonstrated a novel 3D printing method combined with a magnetic field to reorient pre-magnetized NdFeB microparticles along the field using fumed silica as a rheological modifier (Fig. 18f).[288] Upon switching the direction of the magnetic field wrapped around the nozzle, the magnetic composite encoded a complex magnetic moment profile (Fig. 18g). Furthermore, the fumed silica additives in the composite ink enabled the as-printed resin to maintain its reoriented magnetic moment due to the presence of yield stress originating from the rheological properties of the fumed silica (Fig. 18f). Encoding for a high-resolution magnetic moment profile was proposed by using ultraviolet (UV) lithography.[291] Pre-magnetized particles were initially aligned in a UV-curable resin, and then UV light was illuminated on the confined region to achieve a localized magnetic moment profile as small as 250 μm. In this method, a highly responsive magnetic actuator with a digitalized magnetic moment profile can be fabricated enabling complex shape morphing.

Since soft robots are required to be versatile and have an adaptive configuration for task-specific morphing and adaptation to environmental changes, reconfigurable and reprogrammable actuations are necessary. Reversible locking–unlocking processes have been suggested to reprogram actuations by encapsulating magnetic particles with phase-transition materials. Song *et al.* designed oligomeric polyethylene glycol (PEG)-encapsulated NdFeB microparticles, and embedded the encapsulated particles in a silicone matrix to develop reprogrammable magnetic soft actuators (Fig. 18h and i).[296] Because the PEG shell with a low melting temperature (T_m) of 58 °C facilitated the solid-to-liquid phase transition over the T_m for the mobility of NdFeB microparticles, this phase transition resulted in the easy reorientation of NdFeB microparticles along the direction of the external magnetic field. During this process, a particular magnetization profile was simply encoded by wrapping the soft composite around a specific object (Fig. 18h). A cooling process triggered a liquid-to-solid phase transition of the PEG, which then locked the orientation of the magnetic moments, endowing the magnetic composites with the ability to respond to a magnetic field. Interestingly, the magnetic soft composite could be deformed into the shape of the object that was wrapped during encoding, highlighting its potential for use as a surface-copying device (Fig. 18i). Thermally induced phase transition and a subsequent increase in the mobility of magnets enabled the decoding of the magnetization profile and reprograming of a new profile. For a similar yet more localized transition of the magnetization profile, Deng *et al.* adopted a photothermal process with laser scanning, because a high spatial resolution of the laser beam can heat a specific region, inducing the

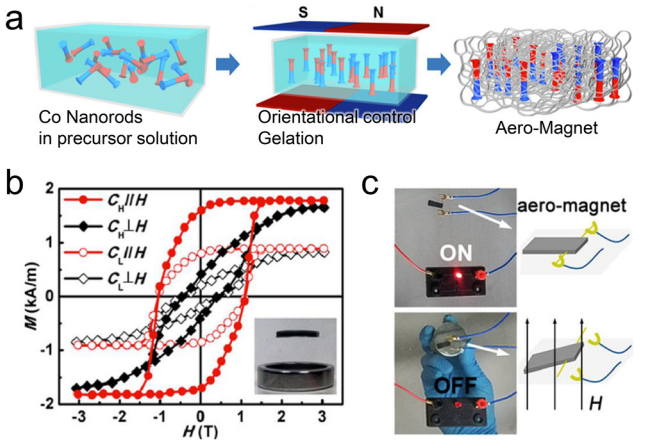

Fig. 19 Ultralight magnetic soft composite with an anisotropic magnetic nanomaterial. (a) Fabrication of a silica-aerogel-based ultralight magnetic composite. Mixing Co NRs with an AR of 9 in a precursor solution (left), aligning Co NRs during gelation by applying a magnetic field (middle), and the aero-magnet achieved by subsequent solvent exchange and critical point drying (right). (b) Magnetic hysteresis curves of the aerogel composite with a high doping ratio of 30 wt% (C_H) and low doping ratio of 15 wt% (C_L) under parallel and vertical magnetic fields. Levitating behavior above the hollow ring magnet (~11 mT) resulting from the light weight of the aerogel matrix (inset image). (c) Possible application of the ultralight magnet in a switching device. Reproduced with permission.[298] Copyright 2019, American Chemical Society.

photothermal effects of NdFeB microparticles.[295] The NdFeB microparticles were encapsulated with polycaprolactone (PCL) that underwent a solid-to-liquid phase transition above its T_m (~60 °C) *via* localized laser irradiation. After the phase transition in the selected space, the external magnetic field could align the magnetic moment of NdFeB microparticles in a certain direction and the microparticles were fixed immediately after removing the laser source. The programmed patterns showed a high resolution of ~300 μm due to the fast and reversible phase transition of the PCL shell and highly localized laser spot for phase transition.

4.2.2. Anisotropy in magnetic nanomaterials for highly controllable actuation. NdFeB particles are the most widely used hard magnetic materials to develop magnetic soft actuators owing to their large net magnetic moment and superior resistance to demagnetization. However, the synthesis of micro/nano-scale NdFeB using a bottom-up approach with low-temperature processes is challenging. Since the available option to reduce the size of NdFeB is top-down mechanical grinding, obtaining hard magnets with small and uniform sizes is difficult. The different dimensions of NdFeB particles result in a broad range of magnetic properties for each particle. This variability is unfavorable for the precise control of magnetic soft actuators due to the unpredictable and non-uniform magnetic properties of the magnetic composite. Therefore, a large quantity of NdFeB particles should be distributed in the matrix to acquire a uniform magnetization state of the magnetic composite. For the precise control of magnetic soft actuators with a low doping ratio of filler, monodisperse magnetic nanomaterials can be a good alternative. However, these monodisperse MNPs are typically characterized by soft magnets, which indicates that MNPs lack sufficient magnetocrystalline anisotropy. The generation of torque under a magnetic field relies on the magnetic easy axis aligning with the field. Owing to the absence of magnetic anisotropy, soft MNPs can just produce translational force but not torque. Using single-crystalline 1D-magnetic nanomaterials enhances the magnetic anisotropy, which is dominantly assisted by shape anisotropy. For example, Li *et al.* fabricated magnetic hydrogel composites by embedding Ni NWs and spiropyran into photocurable hydrogels.[297] During photopolymerization, Ni NWs were aligned in the hydrogel matrix following the direction of an external magnetic field. Then, the magnetic hydrogel composites were soaked in acidic water under dark conditions. When the surface of the magnetic hydrogel composites was exposed to illumination, the soft actuators bent toward the light source as the hydrophilic moiety isomerized to hydrophobic spiropyran, resulting in shrinkage of the gel matrix. The difference between the swellings of the illuminated and unilluminated parts induced a bending strain and generated a magnetization profile in 3D space during shape morphing. Moreover, due to the high magnetic anisotropy of the Ni NWs, a low content of magnetic fillers (0.5 wt%) was sufficient for activating the gel matrix under a relatively weak magnetic field (~16 mT) for coordinating the walking and steering motions. Li *et al.* fabricated an ultralight magnetic soft composite by aligning Co NRs in a silica-aerogel host (Fig. 19a).[298] The high AR (~9) and uni-axial alignment of the

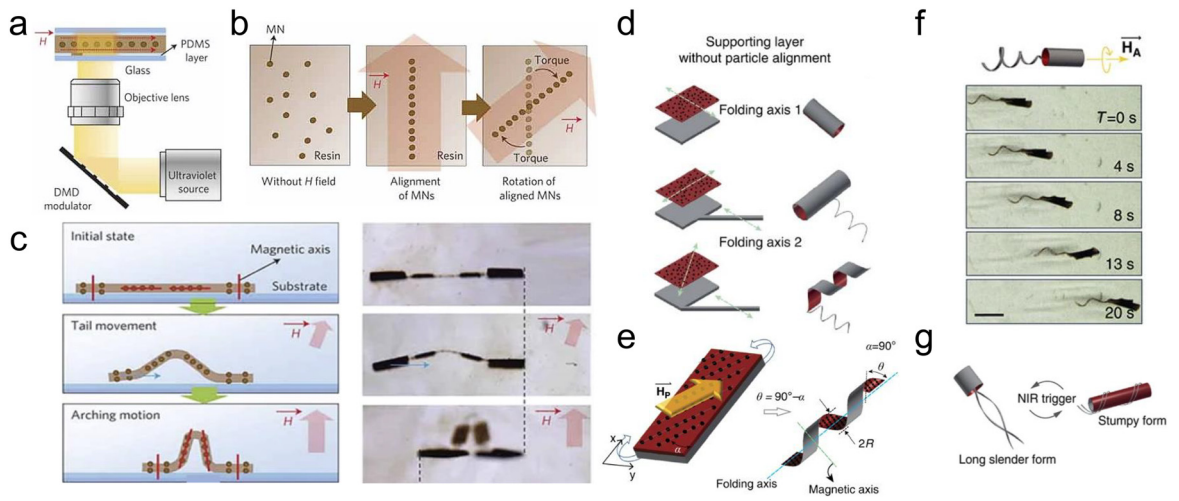

Fig. 20 Magnetic soft actuators with an anisotropic assembly of SPIONs. (a) Polymeric magnetic micro-actuators with an anisotropic assembly of SPIONs prepared by photolithography. (b) SPIONs during fabrication and actuation: randomly dispersed SPIONs under a zero-magnetic field (left), alignment of SPIONs under a magnetic field followed by fixation during curing (middle), and torque generation of the fixed assembly by an external magnetic field (right). (c) Application for a micro-actuator mimicking "looper caterpillar". Configuration of the micro-actuator composed of two elements with in-plane aligned SPIONs as the body and another two elements with vertically aligned SPIONs as the head and tail (left). Real images of the actuation of the micro-actuator (right). Reproduced with permission.[287] Copyright 2011, Springer Nature. Microorganism-inspired actuator with versatile motility appropriate for certain environments: (d) structure of the actuator and its self-folding behavior which is determined by the location of the tail and shape of the body. (e) Controlling the self-folding behavior by programming the alignment of the MNPs. (f) Propulsion of the micro-actuator under a rotating magnetic field and (g) versatile designs of the micro-actuator upon heat treatment enabling various shape morphing modes. Reproduced with Creative Commons CC BY License.[302]

Co NRs provided a significant shape anisotropy, thus effectively controlling the magnetization and the directional response to the external magnetic field (Fig. 19b). The anisotropy of the Co NRs facilitated adequate actuation performance of the magnetic composite with lower contents of Co NRs in the silica-aerogel matrix, which allowed the design of lightweight soft actuators. Therefore, ultralight magnets could float on top of a ring magnet even with a weak field strength of ~11 mT (Fig. 19b-inset), which was applied as a switch in a circuit (Fig. 19c).

Uniaxial arrangements of 0D MNPs can be adopted for manipulating magnetic soft actuators by inducing magnetic anisotropy. For example, superparamagnetic iron oxide NPs (SPIONs) are extensively used magnetic nanomaterials as this MNP exhibits various advantages such as high saturation magnetization,[299] cost-effective production,[300] and biocompatibility when compared with the other magnetic nanomaterials like Co and Ni.[301] However, individual SPIONs do not exhibit coercivity and remanence, which can only show a translational force under an external magnetic field but not torque. The absence of a magnetization orientation limits the programmability of magnetic composites and decreases the complexity of actuation modes.[8] However, if SPIONs can be aligned by a magnetic field to form a chain configuration, the ensemble of SPIONs can undergo a torque following the applied field.[287] Initially, SPIONs mixed in photocurable resins formed a chain configuration in the direction of the external magnetic field and were subsequently fixed in the resin *via* photopolymerization (Fig. 20a). As a result, the magnetic easy axis appeared along the longitudinal direction of the SPION assembly, similar to the magnetic anisotropy. When applying an external magnetic field, a torque could be generated as the longitudinal direction of SPION assemblies has a tendency to rotate, aligning their easy axes along the magnetic field (Fig. 20b). Finally, by connecting two elements where SPIONs were aligned along the in-plane direction and another two elements with vertically aligned SPIONs, a micro-actuator mimicking a "looper caterpillar" was fabricated showing potential for application in micro-actuators (Fig. 20c).

The assembled SPIONs can act as stiffness reinforcing agents.[302] Inspired by microorganisms, a micro-robot consisting of body and tails was designed with motility under a magnetic field by incorporating SPIONs into a hydrogel matrix (Fig. 20d). Microorganisms adjust their shape in response to an environmental change appropriate for the surroundings. The robot body mimicking these functions was made of a bilayer structure comprising a thermo-responsive hydrogel and passive hydrogel matrix, which could be self-folded into a 3D structure. However, the folding sequence was mainly affected by the geometric constraints imposed by the body and tail configuration, which, then, restricted the flexibility in designing the actuation mode. To achieve a high DoF in shape morphing, MNPs were aligned in a specific direction, and the self-folding behavior was manually controlled, irrespective of the body–tail configuration (Fig. 20e). Furthermore, the anisotropic alignments of the MNPs produced a torque upon exposure to an external magnetic field, enabling the propulsion of the micro-actuator in a fluidic environment (Fig. 20f). The thermo-responsive matrix allowed a reversible transition in the structure, facilitating precise control of the actuation

Table 3 Magnetic soft actuators with various magnetic materials

Materials	Polymer matrix	Magnetization or alignment step	Magnetization profile/ encoding method	Content of magnetic particles/dimension of actuators
NdFeB	Shape memory polymer[222]	Magnetization after solidifying	—	40 wt%/50 × 50 × 0.06 mm
	Ecoflex[294]	Magnetization after solidifying	3D profile/wrapping cylinder under a magnetic field	50 wt%/1.5 × 3.7 × 0.185 mm
	UV resin[291]	Reorientation of pre-magnetized particles	3D profile/UV lithographic method	50 wt%/millimeter-scale
	PCL for encapsulation Ecoflex matrix[295]	Reorientation of pre-magnetized particles	3D profile/encapsulating PCL and laser reprogramming	50 wt% for NdFeB@PCL 50 wt% of NdFeB@PCL in Ecoflex/millimeter scale
	Ecoflex[287]	Reorientation of pre-magnetized particles	3D profile/magnetic field-assisted 3D printing	20 vol%/millimeter-scale
Ni nanowires	Spiropyran[297]	Magnetization during solidifying	3D profile/deformation of matrix	5 mg ml^{-1}/millimeter-scale
Co nanorods	Silica aerogel[298]	Magnetization during solidifying	Two domains/two opposite magnetic field	30 wt%/centimeter-scale
Co nanowires	Ecoflex[322]	Magnetization during solidifying	—	10 wt%/4.5 × 15 mm
Fe_3O_4	PEGDA[287]	Magnetization during solidifying	3D profile/UV lithographic method	—/micrometer-scale
	Thermal responsive matrix: PNIPAAm-Aam-PEGDA Passive matrix: PEGDA[302]	Magnetization during solidifying	3D profile/deformation of matrix	4.7 wt% for thermally responsive matrix 1.2 wt% for passive matrix /micrometer-scale
Commercial iron oxide ferrofluid	Gelatin methacryloyl hydrogel[323]	Magnetization during solidifying	3D profile/alignment under a gradient field	2.9 vol%/millimeter-scale

mode in response to external conditions (Fig. 20g). Magnetic soft actuators with various magnetic materials and magnetization profiles are summarized in Table 3.

The stiffness of the anisotropic assembly of MNPs could be further strengthened by subjecting this assembly to an external magnetic field because of the magnetic dipole–dipole interaction, a phenomenon known as the magnetorheological effect, introduced in section 3.4. In the field of robotics, the ability to adjust stiffness is important for gripper technologies.[303–305] While soft grippers offer benefits, such as safer handling and adaptability to different object shapes due to their flexibility, they often lack sufficient grasping force.[306] To address this issue, recent research has focused on soft grippers whose stiffness can be varied to enhance their grasping power.[307] Thus, magnetic soft composites demonstrate potential for application in soft grippers owing to stiffness tunability arising from magnetorheological effects. To maximize the change of stiffness, magnetic soft composites embedded with magnetorheological fluid have been used.[308] Without a magnetic field, the composite shows a very low modulus, enabling conformal attachment to various shapes. Subsequently, by switching on the magnetic field, the magnetic particles in the fluid align into chains along the field lines, significantly increasing the stiffness of the composites. This transformation results in a higher grip strength, thus improving the ability of the gripper to securely hold objects. When the magnetic field is switched off, the stiffness of the composites reduces to its original state, facilitating the release of the gripped object. Therefore, the magnetomechanical effects induced by magnetic anisotropy not only enhance the functionality of magnetic soft actuators but also expand their potential applications.

As magnetic anisotropy in soft actuating materials can be achieved by numerous strategies, precise and digitalized programming of the magnetization profile can be realized. Not only hard magnets but also soft magnets can enhance the actuation performance with high selectivity and controllability based on the magnetic anisotropy. Furthermore, the magnetic anisotropy in magnetic soft composites contributes to the decrease of magnetic filler contents required in the composites and the strength of magnetic field for triggering actuation. The magnetomechanical effect driven by magnetic anisotropy provides additional functionality to the actuators which can be favorable for certain applications including soft grippers. Therefore, actuators with magnetic anisotropy behavior can be applied to wearable rehabilitation robots, ultralight inspection drones, untethered explorers, and intelligent humanoids.

5. Conclusions and future perspective

In summary, this review highlighted the critical role of the magnetic anisotropy of various materials in flexible sensors and soft actuators for granting advanced features and functions to soft robots. Initially, we discussed the fundamental principles of magnetic anisotropy, driven by intrinsic and extrinsic factors including the crystallographic nature of magnetic materials, dependency on shape and dimension, interlayer coupling for exchange bias, and external stress-induced magnetic anisotropy. Magnetic anisotropy does not arise from a single, isolated factor among the aforementioned influencing factors; rather, it emerges as a result of a complex interplay of these factors, with certain dominant elements governing the overall energy of the system. Moreover, we presented and categorized strategies to enhance magnetic anisotropy *via* alignments, shapes, layered structures, and external energy sources. We examined the magnetic anisotropy effects caused by magnetic domain alignment or the arrangement of magnetic nanomaterials across different dimensions and the related novel fabrication methodologies. Such recent breakthroughs in the implications of magnetic anisotropy have significantly improved the performance of magnetic sensors and actuators for their applications in soft robotics. Thanks to magnetic anisotropy, which boosts the magnetic properties of materials toward a specific orientation, magnetic sensors demonstrate outstanding sensitivity, precision, and selectivity. This sensing capability is particularly evident in the detection of changes in both the direction and intensity of magnetic fields. Moreover, magnetic anisotropy facilitates the programming of magnetization in actuating soft bodies. The anisotropy nature of soft actuators enables complex shape transformations without predesigned hinges and effective operation even in weak magnetic fields. These advancements are highly advantageous for magnetic soft robots, which can enhance their response speeds, facilitate both proximity and touch sensing, offer remote control and adjustable actuation, and lead to overall better performance. Therefore, magnetic soft robots have potential applications in fields like biomedical micro-robots, microswimmers, and soft grippers. Among them, biomedical microrobots have been thoroughly explored and are considered the most promising application in the field of implantable and therapeutic robots. With a biocompatible soft matrix, magnetic soft robots can aid in targeted drug delivery and minimally invasive surgery. Additionally, there is a growing need to remove microplastics from the ocean environment. In this context, micro-swimmers capable of navigating through the water environment and collecting microplastics would be another practical application. Also, soft grippers, with the ability to manipulate various materials delicately, offer a feasible application of magnetic actuators by taking advantage of remote controllability, stiffness tunability from the magnetorheological effect, and the softness of the matrix. These applications are anticipated to contribute to improving medical devices, resolving environmental pollution, and enhancing efficiency in industrial lines.

However, several challenges should be addressed for the practical applications of magnetic soft robots in real-world scenarios. Firstly, the high compatibility of these integrated sensors and actuators with surrounding electronic devices, which often face electromagnetic interference (EMI), should be considered.[309–311] The implementation of suitable EMI

shielding materials is necessary to ensure reliable signal transmission between sensors and actuators with the precise control of magnetic soft robots, irrespective of the environmental conditions. Novel design and fabrication methods, such as inducing magnetic anisotropy in managing the geometry of materials or device structures, are essential to minimize external EMI and achieve the selective manipulation of magnetic components in soft robots.

Secondly, safety and biocompatibility are significant concerns, particularly because magnetic soft robots are designed for human interaction in cooperative tasks or for biomedical applications like micro-robotic drug delivery and surgical assistance. While the assistance from highly flexible and functionalized materials combined with the feedback control systems makes soft robots highly relevant in our daily lives, the biocompatibility of magnetic elements remains a debated topic. SPIONs, preferred for their relatively lower toxicity,[312,313] do not offer substantial benefits in terms of biocompatibility *versus* performance for robotic applications.[314] Although encapsulating magnetic components in biocompatible materials is a potential solution, ensuring the inherent biocompatibility of magnetic materials is crucial for long-term and harsh environment applications.[315] Developing low-toxicity magnetic NPs with adjustable spin states can provide safer and more biocompatible options for magnetic soft robots.[316,317]

Finally, the development of wearable and untethered soft robots aims to assist human movement or replace manpower in risky environments. To establish these features, the required strength of the magnetic field source should be minimized for efficient and high DoF operation. Traditional magnetic actuators, which operate in response to the strong and uniform magnetic fields generated by bulky electromagnetic coils, have limitations in terms of their versatility and being bound to ground. To overcome this obstacle, compact electromagnetic coil systems need to be integrated into robot bodies serving as actuation sources. Combining these systems with sensors and actuators is crucial for efficient signal processing and feedback control of soft robots. Moreover, additional components such as wireless communication modules, signal processors, and permanent power sources, all governed by sophisticated closed-loop signal-processing algorithms, ultimately find a way to develop an autonomous, untethered, and intelligent soft robot.

Conflicts of interest

There are no conflicts to declare.

Acknowledgements

This work was supported by the National Research Foundation of Korea (NRF) grant funded by the Korea government (MIST) (No. NRF-2022R1C1C1004845, RS-2023-00207836).

References

1 A. Billard and D. Kragic, *Science*, 2019, **364**, eaat8414.
2 X. Dong, X. Luo, H. Zhao, C. Qiao, J. Li, J. Yi, L. Yang, F. J. Oropeza, T. S. Hu, Q. Xu and H. Zeng, *Soft Matter*, 2022, **18**, 7699–7734.
3 W. Dou, G. Zhong, J. Cao, Z. Shi, B. Peng and L. Jiang, *Adv. Mater. Technol.*, 2021, **6**, 2100018.
4 N. El-Atab, R. B. Mishra, F. Al-Modaf, L. Joharji, A. A. Alsharif, H. Alamoudi, M. Diaz, N. Qaiser and M. M. Hussain, *Adv. Intell. Syst. Comput.*, 2020, **2**, 2000128.
5 Z. Shen, F. Chen, X. Zhu, K.-T. Yong and G. Gu, *J. Mater. Chem. B*, 2020, **8**, 8972–8991.
6 B. Chen and Z. L. Wang, *Small*, 2022, **18**, 2107034.
7 I. Apsite, S. Salehi and L. Ionov, *Chem. Rev.*, 2022, **122**, 1349–1415.
8 Y. Kim and X. Zhao, *Chem. Rev.*, 2022, **122**, 5317–5364.
9 H. Kim, S.-k. Ahn, D. M. Mackie, J. Kwon, S. H. Kim, C. Choi, Y. H. Moon, H. B. Lee and S. H. Ko, *Mater. Today*, 2020, **41**, 243–269.
10 P. Won, K. K. Kim, H. Kim, J. J. Park, I. Ha, J. Shin, J. Jung, H. Cho, J. Kwon, H. Lee and S. H. Ko, *Adv. Mater.*, 2021, **33**, 2002397.
11 H. Lee, H. Kim, I. Ha, J. Jung, P. Won, H. Cho, J. Yeo, S. Hong, S. Han, J. Kwon, K. J. Cho and S. H. Ko, *Soft Robot.*, 2019, **6**(6), 760–767.
12 H. Kim, H. Lee, I. Ha, J. Jung, P. Won, H. Cho, J. Yeo, S. Hong, S. Han, J. Kwon, K.-J. Cho and S. H. Ko, *Adv. Funct. Mater.*, 2018, **28**, 1801847.
13 C. Hegde, J. Su, J. M. R. Tan, K. He, X. Chen and S. Magdassi, *ACS Nano*, 2023, **17**, 15277–15307.
14 C. Han, Y. Jeong, J. Ahn, T. Kim, J. Choi, J.-H. Ha, H. Kim, S. H. Hwang, S. Jeon, J. Ahn, J. T. Hong, J. J. Kim, J.-H. Jeong and I. Park, *Adv. Sci.*, 2023, **10**, 2302775.
15 H. Wang, M. Totaro and L. Beccai, *Adv. Sci.*, 2018, **5**, 1800541.
16 A. Tsay, T. J. Allen, U. Proske and M. J. Giummarra, *Neurosci. Biobehav. Rev.*, 2015, **52**, 221–232.
17 Z. Lin, Z. Wang, W. Zhao, Y. Xu, X. Wang, T. Zhang, Z. Sun, L. Lin and Z. Peng, *Adv. Intell. Syst. Comput.*, 2023, **5**, 2200329.
18 D. Alatorre, D. Axinte and A. Rabani, *IEEE Trans. Robot.*, 2022, **38**, 526–535.
19 P. Gambardella, S. Rusponi, M. Veronese, S. S. Dhesi, C. Grazioli, A. Dallmeyer, I. Cabria, R. Zeller, P. H. Dederichs, K. Kern, C. Carbone and H. Brune, *Science*, 2003, **300**, 1130–1133.
20 P. Bruno, *Phys. Rev. B: Condens. Matter Mater. Phys.*, 1989, **39**, 865–868.
21 B. D. Cullity and C. D. Graham, in *Introduction to Magnetic Materials*, ed. L. Hanzo, Wiley, New Jersey, 2nd edn, 2009, ch. 7, pp. 197–239.
22 Q. Fan, Z. Li, C. Wu and Y. Yin, *Precis. Chem.*, 2023, **1**, 272–298.
23 R. C. O'handley, *Modern magnetic materials: principles and applications*, Wiley, 2000.

24 J. M. D. Coey, in *Magnetism and Magnetic Materials*, Cambridge University Press, Cambridge, 2010, ch. 5, pp. 128–194.
25 L. Sagnotti, in *Encyclopedia of Solid Earth Geophysics*, ed. H. K. Gupta, Springer, Netherlands, Dordrecht, 2011, pp. 717–729.
26 Z. Yang, Y. Chen, W. Liu, Y. Wang, Y. Li, D. Zhang, Q. Lu, Q. Wu, H. Zhang and M. Yue, *Nanomaterials*, 2022, **12**, 1261.
27 A. P. Guimarães, in *Principles of Nanomagnetism*, ed. A. P. Guimarães, Springer Berlin Heidelberg, Berlin, Heidelberg, 2009, pp. 57–104. DOI: **10.1007/978-3-642-01482-6_3**.
28 J. Mohapatra, M. Xing and J. P. Liu, *Materials*, 2019, **12**, 3208.
29 J. Mohapatra and J. P. Liu, in *Handbook of Magnetic Materials*, ed. E. Brück, Elsevier, 2018, vol. 27, pp. 1–57.
30 E. C. Stoner and E. P. Wohlfarth, *Nature*, 1947, **160**, 650–651.
31 A.-H. Lu, E. L. Salabas and F. Schüth, *Angew. Chem., Int. Ed.*, 2007, **46**, 1222–1244.
32 Z. Ma, J. Mohapatra, K. Wei, J. P. Liu and S. Sun, *Chem. Rev.*, 2023, **123**, 3904–3943.
33 M. D. Nguyen, H.-V. Tran, S. Xu and T. R. Lee, *Appl. Sci.*, 2021, **11**, 11301.
34 J. S. Lee, J. M. Cha, H. Y. Yoon, J. K. Lee and Y. K. Kim, *Sci. Rep.*, 2015, **5**, 12135.
35 M. Unni, A. M. Uhl, S. Savliwala, B. H. Savitzky, R. Dhavalikar, N. Garraud, D. P. Arnold, L. F. Kourkoutis, J. S. Andrew and C. Rinaldi, *ACS Nano*, 2017, **11**, 2284–2303.
36 F. Chen, N. Ilyas, X. Liu, Z. Li, S. Yan and H. Fu, *Front. Energy Res.*, 2021, **9**, 780008.
37 J. Nogués and I. K. Schuller, *J. Magn. Magn. Mater.*, 1999, **192**, 203–232.
38 W. H. Meiklejohn, *J. Appl. Phys.*, 2004, **33**, 1328–1335.
39 M. Tsunoda, M. Naka, D. Y. Kim and M. Takahashi, *J. Magn. Magn. Mater.*, 2006, **304**, e88–e90.
40 Z. Swiatkowska-Warkocka, K. Kawaguchi, H. Wang, Y. Katou and N. Koshizaki, *Nanoscale Res. Lett.*, 2011, **6**, 226.
41 M. Heigl, C. Vogler, A.-O. Mandru, X. Zhao, H. J. Hug, D. Suess and M. Albrecht, *ACS Appl. Nano Mater.*, 2020, **3**, 9218–9225.
42 H. Singh, R. Gupta, T. Chakraborty, A. Gupta and C. Mitra, *IEEE Trans. Magn.*, 2014, **50**, 1–4.
43 W. B. Rui, Y. Hu, A. Du, B. You, M. W. Xiao, W. Zhang, S. M. Zhou and J. Du, *Sci. Rep.*, 2015, **5**, 13640.
44 W. H. Meiklejohn and C. P. Bean, *Phys. Rev.*, 1957, **105**, 904–913.
45 R. Jungblut, R. Coehoorn, M. T. Johnson, J. aan de Stegge and A. Reinders, *J. Appl. Phys.*, 1994, **75**, 6659–6664.
46 A. P. Malozemoff, *Phys. Rev. B: Condens. Matter Mater. Phys.*, 1987, **35**, 3679–3682.
47 D. Mauri, H. C. Siegmann, P. S. Bagus and E. Kay, *J. Appl. Phys.*, 1987, **62**, 3047–3049.
48 T. Ambrose and C. L. Chien, *J. Appl. Phys.*, 1998, **83**, 6822–6824.
49 U. Nowak, K. D. Usadel, J. Keller, P. Miltényi, B. Beschoten and G. Güntherodt, *Phys. Rev. B: Condens. Matter Mater. Phys.*, 2002, **66**, 014430.
50 T. Kobayashi, H. Kato, T. Kato, S. Tsunashima and S. Iwata, *J. Phys.: Conf. Ser.*, 2010, **200**, 072052.
51 W. Zhang and K. M. Krishnan, *Mater. Sci. Eng., R*, 2016, **105**, 1–20.
52 J. Nogués, T. J. Moran, D. Lederman, I. K. Schuller and K. V. Rao, *Phys. Rev. B: Condens. Matter Mater. Phys.*, 1999, **59**, 6984–6993.
53 W. Su, Z. Wang, T. Wen, Z. Hu, J. Wu, Z. Zhou and M. Liu, *IEEE Electron Device Lett.*, 2019, **40**, 969–972.
54 M. F. Hansen and G. Rizzi, *IEEE Trans. Magn.*, 2017, **53**, 1–11.
55 J. C. S. Kools, *IEEE Trans. Magn.*, 1996, **32**, 3165–3184.
56 S. S. P. Parkin, K. P. Roche, M. G. Samant, P. M. Rice, R. B. Beyers, R. E. Scheuerlein, E. J. O'Sullivan, S. L. Brown, J. Bucchigano, D. W. Abraham, Y. Lu, M. Rooks, P. L. Trouilloud, R. A. Wanner and W. J. Gallagher, *J. Appl. Phys.*, 1999, **85**, 5828–5833.
57 E. W. Lee, *Rep. Prog. Phys.*, 1955, **18**, 184.
58 B. D. Cullity and C. D. Graham, in *Introduction to Magnetic Materials*, ed. L. Hanzo, Wiley, New Jersey, 2nd edn, 2009, ch. 8, pp. 241–273.
59 A. G. Olabi and A. Grunwald, *Mater. Des.*, 2008, **29**, 469–483.
60 N. B. Ekreem, A. G. Olabi, T. Prescott, A. Rafferty and M. S. J. Hashmi, *J. Mater. Process. Technol.*, 2007, **191**, 96–101.
61 M. S. Amiri, M. Thielen, M. Rabung, M. Marx, K. Szielasko and C. Boller, *J. Magn. Magn. Mater.*, 2014, **372**, 16–22.
62 Z. Deng and M. J. Dapino, *Smart Mater. Struct.*, 2018, **27**, 113001.
63 A. Bieńkowski and J. Kulikowski, *J. Magn. Magn. Mater.*, 1980, **19**, 120–122.
64 R. Q. Wu, L. J. Chen, A. Shick and A. J. Freeman, *J. Magn. Magn. Mater.*, 1998, **177–181**, 1216–1219.
65 F. Wang, X. Dai, Y. Li, H. Jia, X. Wang and G. Liu, Presented in part at the 2015 IEEE International Magnetics Conference, Beijing, May, 2015.
66 A. Speliotis and D. Niarchos, *Sens. Actuators, A*, 2003, **106**, 298–301.
67 A. Pateras, R. Harder, S. Manna, B. Kiefer, R. L. Sandberg, S. Trugman, J. W. Kim, J. de la Venta, E. E. Fullerton, O. G. Shpyrko and E. Fohtung, *NPG Asia Mater.*, 2019, **11**, 59.
68 G. O. Fulop, M. B. S. Dias, H. R. Z. Sandim and C. Bormio-Nunes, *J. Magn. Magn. Mater.*, 2021, **527**, 167702.
69 K. Y. Ho, X. Y. Xiong, J. Zhi and L. Z. Cheng, *J. Appl. Phys.*, 1993, **74**, 6788–6790.
70 D. Vanoost, S. Steentjes, J. Peuteman, G. Gielen, H. De Gersem, D. Pissoort and K. Hameyer, *J. Magn. Magn. Mater.*, 2016, **414**, 168–179.

71 P. Ruuskanen and P. Kettunen, *J. Magn. Magn. Mater.*, 1991, **98**, 349–358.
72 A. E. Clark and K. B. Hathaway, *MRS Bull.*, 1993, **18**, 34–41.
73 S. Kotapati, A. Javed, N. Reeves-McLaren, M. R. J. Gibbs and N. A. Morley, *J. Magn. Magn. Mater.*, 2013, **331**, 67–71.
74 H. Wang, Y. N. Zhang, R. Q. Wu, L. Z. Sun, D. S. Xu and Z. D. Zhang, *Sci. Rep.*, 2013, **3**, 3521.
75 M. Klokkenburg, C. Vonk, E. M. Claesson, J. D. Meeldijk, B. H. Erné and A. P. Philipse, *J. Am. Chem. Soc.*, 2004, **126**, 16706–16707.
76 L. N. Donselaar, P. M. Frederik, P. Bomans, P. A. Buining, B. M. Humbel and A. P. Philipse, *J. Magn. Magn. Mater.*, 1999, **201**, 58–61.
77 R. Massart, *IEEE Trans. Magn.*, 1981, **17**, 1247–1248.
78 J. Park, K. An, Y. Hwang, J.-G. Park, H.-J. Noh, J.-Y. Kim, J.-H. Park, N.-M. Hwang and T. Hyeon, *Nat. Mater.*, 2004, **3**, 891–895.
79 S. Sun, H. Zeng, D. B. Robinson, S. Raoux, P. M. Rice, S. X. Wang and G. Li, *J. Am. Chem. Soc.*, 2004, **126**, 273–279.
80 H. Deng, X. Li, Q. Peng, X. Wang, J. Chen and Y. Li, *Angew. Chem., Int. Ed.*, 2005, **44**, 2782–2785.
81 M. A. Correa-Duarte, M. Grzelczak, V. Salgueiriño-Maceira, M. Giersig, L. M. Liz-Marzán, M. Farle, K. Sierazdki and R. Diaz, *J. Phys. Chem. B*, 2005, **109**, 19060–19063.
82 X. Fan, F. Tan, G. Zhang and F. Zhang, *Mater. Sci. Eng., A*, 2007, **454–455**, 37–42.
83 K. Liu, L. Han, P. Tang, K. Yang, D. Gan, X. Wang, K. Wang, F. Ren, L. Fang, Y. Xu, Z. Lu and X. Lu, *Nano Lett.*, 2019, **19**, 8343–8356.
84 R. Sheparovych, Y. Sahoo, M. Motornov, S. Wang, H. Luo, P. N. Prasad, I. Sokolov and S. Minko, *Chem. Mater.*, 2006, **18**, 591–593.
85 Y. Hu, L. He and Y. Yin, *Angew. Chem., Int. Ed.*, 2011, **50**, 3747–3750.
86 Q. Xiong, C. Y. Lim, J. Ren, J. Zhou, K. Pu, M. B. Chan-Park, H. Mao, Y. C. Lam and H. Duan, *Nat. Commun.*, 2018, **9**, 1743.
87 J. Saiz-Poseu, J. Mancebo-Aracil, F. Nador, F. Busqué and D. Ruiz-Molina, *Angew. Chem., Int. Ed.*, 2019, **58**, 696–714.
88 H. Lee, S. M. Dellatore, W. M. Miller and P. B. Messersmith, *Science*, 2007, **318**, 426–430.
89 B. K. Ahn, *J. Am. Chem. Soc.*, 2017, **139**, 10166–10171.
90 L. r. Meng, W. Chen, C. Chen, H. Zhou, Q. Peng and Y. Li, *Cryst. Growth Des.*, 2010, **10**, 479–482.
91 K. Nakata, Y. Hu, O. Uzun, O. Bakr and F. Stellacci, *Adv. Mater.*, 2008, **20**, 4294–4299.
92 G. A. DeVries, M. Brunnbauer, Y. Hu, A. M. Jackson, B. Long, B. T. Neltner, O. Uzun, B. H. Wunsch and F. Stellacci, *Science*, 2007, **315**, 358–361.
93 Q. He, T. Yuan, S. Wei, N. Haldolaarachchige, Z. Luo, D. P. Young, A. Khasanov and Z. Guo, *Angew. Chem., Int. Ed.*, 2012, **51**, 8842–8845.
94 Y. Xia, Q. Chen and U. Banin, *Chem. Rev.*, 2023, **123**, 3325–3328.
95 Y. Soumare, C. Garcia, T. Maurer, G. Chaboussant, F. Ott, F. Fiévet, J.-Y. Piquemal and G. Viau, *Adv. Funct. Mater.*, 2009, **19**, 1971–1977.
96 Y. C. Zhang, J. Y. Tang and X. Y. Hu, *J. Alloys Compd.*, 2008, **462**, 24–28.
97 V. F. Puntes, K. M. Krishnan and A. P. Alivisatos, *Science*, 2001, **291**, 2115–2117.
98 L. Hu, R. Zhang and Q. Chen, *Nanoscale*, 2014, **6**, 14064–14105.
99 L. Y. Zhang, D. S. Xue, X. F. Xu, A. B. Gui and C. X. Gao, *J. Phys.: Condens. Matter*, 2004, **16**, 4541.
100 X. Pang, Y. He, J. Jung and Z. Lin, *Science*, 2016, **353**, 1268–1272.
101 D. S. Xue, C. X. Gao, Q. F. Liu and L. Y. Zhang, *J. Phys.: Condens. Matter*, 2003, **15**, 1455.
102 D.-S. Xue, L.-Y. Zhang, C.-X. Gao, X.-F. Xu and A.-B. Gui, *Chin. Phys. Lett.*, 2004, **21**, 733.
103 J. Cha, J. S. Lee, S. J. Yoon, Y. K. Kim and J.-K. Lee, *RSC Adv.*, 2013, **3**, 3631–3637.
104 Z. Liu, D. Zhang, S. Han, C. Li, B. Lei, W. Lu, J. Fang and C. Zhou, *J. Am. Chem. Soc.*, 2005, **127**, 6–7.
105 C.-J. Jia, L.-D. Sun, Z.-G. Yan, L.-P. You, F. Luo, X.-D. Han, Y.-C. Pang, Z. Zhang and C.-H. Yan, *Angew. Chem., Int. Ed.*, 2005, **44**, 4328–4333.
106 J. Wang, Q. Chen, C. Zeng and B. Hou, *Adv. Mater.*, 2004, **16**, 137–140.
107 Y. Xiong, Y. Xie, Z. Li, R. Zhang, J. Yang and C. Wu, *New J. Chem.*, 2003, **27**, 588–590.
108 W. Wu, X. Xiao, S. Zhang, J. Zhou, L. Fan, F. Ren and C. Jiang, *J. Phys. Chem. C*, 2010, **114**, 16092–16103.
109 S. Palchoudhury, W. An, Y. Xu, Y. Qin, Z. Zhang, N. Chopra, R. A. Holler, C. H. Turner and Y. Bao, *Nano Lett.*, 2011, **11**, 1141–1146.
110 F. Dumestre, B. Chaudret, C. Amiens, M.-C. Fromen, M.-J. Casanove, P. Renaud and P. Zurcher, *Angew. Chem., Int. Ed.*, 2002, **41**, 4286–4289.
111 F. Dumestre, B. Chaudret, C. Amiens, M. Respaud, P. Fejes, P. Renaud and P. Zurcher, *Angew. Chem., Int. Ed.*, 2003, **42**, 5213–5216.
112 F. Fiévet, S. Ammar-Merah, R. Brayner, F. Chau, M. Giraud, F. Mammeri, J. Peron, J. Y. Piquemal, L. Sicard and G. Viau, *Chem. Soc. Rev.*, 2018, **47**, 5187–5233.
113 K. A. Atmane, C. Michel, J.-Y. Piquemal, P. Sautet, P. Beaunier, M. Giraud, M. Sicard, S. Nowak, R. Losno and G. Viau, *Nanoscale*, 2014, **6**, 2682–2692.
114 R. K. Ramamoorthy, A. Viola, B. Grindi, J. Peron, C. Gatel, M. Hytch, R. Arenal, L. Sicard, M. Giraud, J.-Y. Piquemal and G. Viau, *Nano Lett.*, 2019, **19**, 9160–9169.
115 K. Mrad, F. Schoenstein, H. T. T. Nong, E. Anagnostopoulou, A. Viola, L. Mouton, S. Mercone, C. Ricolleau, N. Jouini, M. Abderraba, L. M. Lacroix, G. Viau and J. Y. Piquemal, *CrystEngComm*, 2017, **19**, 3476–3484.
116 H.-H. Xu, Q. Wu, M. Yue, C.-L. Li and H.-J. Li, *Rare Met.*, 2023, **42**, 1994–1999.

117 S. Ener, E. Anagnostopoulou, I. Dirba, L.-M. Lacroix, F. Ott, T. Blon, J.-Y. Piquemal, K. P. Skokov, O. Gutfleisch and G. Viau, *Acta Mater.*, 2018, **145**, 290–297.
118 K. A. Atmane, F. Zighem, Y. Soumare, M. Ibrahim, R. Boubekri, T. Maurer, J. Margueritat, J. Y. Piquemal, F. Ott, G. Chaboussant, F. Schoenstein, N. Jouini and G. Viau, *J. Solid State Chem.*, 2013, **197**, 297–303.
119 P. D. Kulkarni, S. K. Dhar, A. Provino, P. Manfrinetti and A. K. Grover, *Phys. Rev. B: Condens. Matter Mater. Phys.*, 2010, **82**, 144411.
120 J. S. Kouvel and C. D. Graham, *J. Phys. Chem. Solids*, 1959, **11**, 220–225.
121 Y. Ma, Y. Yang, Y. Gao and Y. Hu, *Phys. Chem. Chem. Phys.*, 2021, **23**, 17365–17373.
122 S. Giri, M. Patra and S. Majumdar, *J. Phys.: Condens. Matter*, 2011, **23**, 073201.
123 M. Ávila-Gutiérrez, A. Moisset, A.-T. Ngo, S. Costanzo, G. Simon, P. Colomban, M. Petit, C. Petit and I. Lisiecki, *Colloids Surf., A*, 2023, **676**, 132281.
124 J. A. González, J. P. Andrés, J. A. De Toro, P. Muñiz, T. Muñoz, O. Crisan, C. Binns and J. M. Riveiro, *J. Nanopart. Res.*, 2009, **11**, 2105–2111.
125 O. Crisan, K. von Haeften, A. M. Ellis and C. Binns, *J. Nanopart. Res.*, 2008, **10**, 193–199.
126 S. A. Koch, G. Palasantzas, T. Vystavel, J. T. M. De Hosson, C. Binns and S. Louch, *Phys. Rev. B: Condens. Matter Mater. Phys.*, 2005, **71**, 085410.
127 V. Skumryev, S. Stoyanov, Y. Zhang, G. Hadjipanayis, D. Givord and J. Nogués, *Nature*, 2003, **423**, 850–853.
128 Z. M. Tian, S. L. Yuan, S. Y. Yin, L. Liu, J. H. He, H. N. Duan, P. Li and C. H. Wang, *Appl. Phys. Lett.*, 2008, **93**, 222505.
129 Y. Shen, Y. Wu, H. Xie, K. Li, J. Qiu and Z. Guo, *J. Appl. Phys.*, 2002, **91**, 8001–8003.
130 K. Temst, E. Popova, H. Loosvelt, M. J. Van Bael, S. Brems, Y. Bruynseraede, C. Van Haesendonck, H. Fritzsche, M. Gierlings, L. H. A. Leunissen and R. Jonckheere, *J. Magn. Magn. Mater.*, 2006, **304**, 14–18.
131 Z. B. Guo, Y. K. Zheng, K. B. Li, Z. Y. Liu, P. Luo and Y. H. Wu, *J. Appl. Phys.*, 2004, **95**, 4918–4921.
132 M. Perzanowski, O. Polit, J. Chojenka, W. Sas, A. Zarzycki and M. Marszalek, *Nanotechnology*, 2022, **33**, 495707.
133 A. Hoffmann, M. Grimsditch, J. E. Pearson, J. Nogués, W. A. A. Macedo and I. K. Schuller, *Phys. Rev. B: Condens. Matter Mater. Phys.*, 2003, **67**, 220406.
134 W. Zhang, D. N. Weiss and K. M. Krishnan, *J. Appl. Phys.*, 2010, **107**, 09D724.
135 C. Liu, C. Yu, H. Jiang, L. Shen, C. Alexander and G. J. Mankey, *J. Appl. Phys.*, 2000, **87**, 6644–6646.
136 D. Kumar, S. Singh and A. Gupta, *J. Appl. Phys.*, 2016, **120**, 085307.
137 B.-Y. Wang, C.-J. Chen, K. Lin, C.-Y. Hsu, J.-Y. Ning, M.-S. Tsai, T.-H. Chuang, D.-H. Wei and S.-C. Weng, *Appl. Surf. Sci.*, 2020, **533**, 147501.
138 K.-i. Imakita, M. Tsunoda and M. Takahashi, *J. Appl. Phys.*, 2005, **97**, 10K106.
139 M. S. Lund, W. A. A. Macedo, K. Liu, J. Nogués, I. K. Schuller and C. Leighton, *Phys. Rev. B: Condens. Matter Mater. Phys.*, 2002, **66**, 054422.
140 S. K. Mishra, *J. Magn. Magn. Mater.*, 2019, **488**, 165374.
141 M. Meinert, B. Büker, D. Graulich and M. Dunz, *Phys. Rev. B: Condens. Matter Mater. Phys.*, 2015, **92**, 144408.
142 N. T. Thanh, M. G. Chun, N. D. Ha, K. Y. Kim, C. O. Kim and C. G. Kim, *J. Magn. Magn. Mater.*, 2006, **305**, 432–435.
143 A. Kohn, A. Kovács, R. Fan, G. J. McIntyre, R. C. C. Ward and J. P. Goff, *Sci. Rep.*, 2013, **3**, 2412.
144 R. Wu, M. Xue, T. Maity, Y. Peng, S. K. Giri, G. Tian, J. L. MacManus-Driscoll and J. Yang, *Phys. Rev. B*, 2020, **101**, 014425.
145 M. Dunz and M. Meinert, *J. Appl. Phys.*, 2020, **128**, 153902.
146 H. Lu, J. F. Bi, K. L. Teo, T. Liew and T. C. Chong, *J. Appl. Phys.*, 2010, **107**, 09D717.
147 T. Blachowicz and A. Ehrmann, *Coatings*, 2021, **11**, 122.
148 M. Öztürk, E. Demirci, R. Topkaya, S. Kazan, N. Akdoğan, M. Obaida and K. Westerholt, *J. Supercond. Novel Magn.*, 2012, **25**, 2597–2603.
149 H.-C. Wu, R. Ramos, R. G. S. Sofin, Z.-M. Liao, M. Abid and I. V. Shvets, *Appl. Phys. Lett.*, 2012, **101**, 052402.
150 N. N. Phuoc, G. Chai and C. K. Ong, *J. Appl. Phys.*, 2012, **112**, 083925.
151 N. N. Phuoc and C. K. Ong, *J. Appl. Phys.*, 2013, **114**, 043911.
152 F. Liu and C. A. Ross, *J. Appl. Phys.*, 2014, **116**, 194307.
153 Y. Guo, Y. Ouyang, N. Sato, C. C. Ooi and S. X. Wang, *IEEE Sens. J.*, 2017, **17**, 3309–3315.
154 S. Bhatti, R. Sbiaa, A. Hirohata, H. Ohno, S. Fukami and S. N. Piramanayagam, *Mater. Today*, 2017, **20**, 530–548.
155 J. Nogués, J. Sort, V. Langlais, V. Skumryev, S. Suriñach, J. S. Muñoz and M. D. Baró, *Phys. Rep.*, 2005, **422**, 65–117.
156 A. Nemoto, Y. Otani, S. G. Kim, K. Fukamichi, O. Kitakami and Y. Shimada, *Appl. Phys. Lett.*, 1999, **74**, 4026–4028.
157 V. Baltz, J. Sort, S. Landis, B. Rodmacq and B. Dieny, *Phys. Rev. Lett.*, 2005, **94**, 117201.
158 E. Elahi, G. Dastgeer, G. Nazir, S. Nisar, M. Bashir, H. A. Qureshi, D.-k. Kim, J. Aziz, M. Aslam, K. Hussain, M. A. Assiri and M. Imran, *Comput. Mater. Sci.*, 2022, **213**, 111670.
159 C. Favieres, J. Vergara, C. Magén, M. R. Ibarra and V. Madurga, *J. Alloys Compd.*, 2016, **664**, 695–706.
160 M. Li, H. Yang, Y. Xie, K. Huang, L. Pan, W. Tang, X. Bao, Y. Yang, J. Sun, X. Wang, S. Che and R.-W. Li, *Nano Lett.*, 2023, **23**, 8073–8080.
161 J. Ryu, S. Priya, K. Uchino and H.-E. Kim, *J. Electroceram.*, 2002, **8**, 107–119.
162 T. A. Baudendistel and M. L. Turner, *IEEE Sens. J.*, 2007, **7**, 245–250.
163 A. Chernyshov, M. Overby, X. Liu, J. K. Furdyna, Y. Lyanda-Geller and L. P. Rokhinson, *Nat. Phys.*, 2009, **5**, 656–659.
164 Z.-Y. Jia, H.-F. Liu, F.-J. Wang, W. Liu and C.-Y. Ge, *Measurement*, 2011, **44**, 88–95.
165 P. P. Phulé, *Smart Mater. Bull.*, 2001, **2001**, 7–10.

166 L. Chen and S. Jerrams, *J. Appl. Phys.*, 2011, **110**, 013513.
167 Y. Han, W. Hong and L. E. Faidley, *Int. J. Solids Struct.*, 2013, **50**, 2281–2288.
168 J. O'Donnell, M. S. Rzchowski, J. N. Eckstein and I. Bozovic, *Appl. Phys. Lett.*, 1998, **72**, 1775–1777.
169 F. T. Calkins, A. B. Flatau and M. J. Dapino, *J. Intell. Mater. Syst. Struct.*, 2007, **18**, 1057–1066.
170 H.-C. Chang, S.-C. Liao, H.-S. Hsieh, J.-H. Wen, C.-H. Lai and W. Fang, *Sens. Actuators, A*, 2016, **238**, 25–36.
171 A. Grunwald and A. G. Olabi, *Sens. Actuators, A*, 2008, **144**, 161–175.
172 J. P. Joule, *Ann. Electr. Magn. Chem.*, 1842, **8**, 219–224.
173 A. E. Clark and H. S. Belson, *Phys. Rev. B: Solid State*, 1972, **5**, 3642–3644.
174 J. D. Lopez, A. Dante, A. O. Cremonezi, R. M. Bacurau, C. C. Carvalho, R. C. d. S. B. Allil, E. C. Ferreira and M. M. Werneck, *IEEE Sens. J.*, 2020, **20**, 3572–3578.
175 M. A. Anjanappa and J. Bi, *Smart Struct. Intel. Sys.*, 1993, **1917**, 908–918.
176 J. M. Vranish, D. P. Naik, J. B. Restorff and J. P. Teter, *IEEE Trans. Magn.*, 1991, **27**, 5355–5357.
177 D. Satpathi, J. A. Moore and M. G. Ennis, *IEEE Sens. J.*, 2005, **5**, 1057–1065.
178 C. Y. Lo, S. W. Or and H. L. W. Chan, *IEEE Trans. Magn.*, 2006, **42**, 3111–3113.
179 J. D. Snodgrass and O. D. McMasters, *J. Alloys Compd.*, 1997, **258**, 24–29.
180 A. E. Clark, J. P. Teter, M. Wun-Fogle, M. Moffett and J. Lindberg, *J. Appl. Phys.*, 1990, **67**, 5007–5009.
181 S. Zhao, H. Liu, X. Han, X. Meng, J. Qu, Y. Li and S. Li, *J. Appl. Phys.*, 2006, **99**, 08M708.
182 C. Rodríguez, A. Barrio, I. Orue, J. L. Vilas, L. M. León, J. M. Barandiarán and M. L. F. Ruiz, *Sens. Actuators, A*, 2008, **142**, 538–541.
183 K. K. Mohaideen and P. A. Joy, *ACS Appl. Mater. Interfaces*, 2012, **4**, 6421–6425.
184 S. E. Shirsath, D. Wang, S. S. Jadhav, M. L. Mane and S. Li, in *Handbook of Sol-Gel Science and Technology: Processing, Characterization and Applications*, ed. L. Klein, M. Aparicio and A. Jitianu, Springer International Publishing, Cham, 2018, pp. 695–735, DOI: **10.1007/978-3-319-32101-1_125**.
185 H. Lim, M. G. Lee, J. H. Kim, B. L. Adams and R. H. Wagoner, *Int. J. Plast.*, 2011, **27**, 1328–1354.
186 H. Van Swygenhoven, D. Farkas and A. Caro, *Phys. Rev. B: Condens. Matter Mater. Phys.*, 2000, **62**, 831–838.
187 C.-C. Hu, Z. Zhang, T.-N. Yang, Y.-G. Shi, X.-X. Cheng, J.-J. Ni, J.-G. Hao, W.-F. Rao and L.-Q. Chen, *Appl. Phys. Lett.*, 2019, **115**, 162402.
188 S. D. Bhame and P. A. Joy, *Sens. Actuators, A*, 2007, **137**, 256–261.
189 J. Wang, X. Gao, C. Yuan, J. Li and X. Bao, *J. Magn. Magn. Mater.*, 2016, **401**, 662–666.
190 S. Guruswamy, M. R. Loveless, N. Srisukhumbowornchai, M. K. McCarter and J. P. Teter, *IEEE Trans. Magn.*, 2000, **36**, 3219–3222.
191 D. Davino, A. Giustiniani and C. Visone, *Phys. B*, 2012, **407**, 1427–1432.
192 Q. B. Hu, Y. Hu, S. Zhang, W. Tang, X. J. He, Z. Li, Q. Q. Cao, D. H. Wang and Y. W. Du, *Appl. Phys. Lett.*, 2018, **112**, 052404.
193 X. Guan, X. Dong and J. Ou, *J. Magn. Magn. Mater.*, 2008, **320**, 158–163.
194 S. H. Lim, S. R. Kim, S. Y. Kang, J. K. Park, J. T. Nam and D. Son, *J. Magn. Magn. Mater.*, 1999, **191**, 113–121.
195 R. Elhajjar, C.-T. Law and A. Pegoretti, *Prog. Mater. Sci.*, 2018, **97**, 204–229.
196 X. Guan, X. Dong and J. Ou, *J. Magn. Magn. Mater.*, 2009, **321**, 2742–2748.
197 Z. Yang, Z. Wang, K. Nakajima, D. Neyama and F. Narita, *Compos. Sci. Technol.*, 2021, **210**, 108840.
198 K. Danas, S. V. Kankanala and N. Triantafyllidis, *J. Mech. Phys. Solids*, 2012, **60**, 120–138.
199 A. D. M. Charles, A. N. Rider, S. A. Brown and C.-H. Wang, *J. Mater. Chem. C*, 2022, **10**, 16865–16877.
200 X. Dong, M. Qi, X. Guan and J. Ou, *Polym. Test.*, 2010, **29**, 369–374.
201 T. A. Duenas and G. P. Carman, *J. Appl. Phys.*, 2000, **87**, 4696–4701.
202 B. Li, T. Zhang, Y. Wu and C. Jiang, *J. Alloys Compd.*, 2019, **805**, 1266–1270.
203 K. K. Mohaideen and P. A. Joy, *Appl. Phys. Lett.*, 2012, **101**, 072405.
204 S. Bednarek, *Appl. Phys. A*, 1999, **68**, 63–67.
205 W. Chen, Z. Zhang and P. H. J. Kouwer, *Small*, 2022, **18**, 2203033.
206 A. K. Bastola, M. Paudel, L. Li and W. Li, *Smart Mater. Struct.*, 2020, **29**, 123002.
207 L. C. Davis, *J. Appl. Phys.*, 1999, **85**, 3348–3351.
208 Y. Li, J. Li, W. Li and H. Du, *Smart Mater. Struct.*, 2014, **23**, 123001.
209 T. H. Nam, I. Petríková and B. Marvalová, *Polym. Test.*, 2020, **81**, 106272.
210 H. S. Jung, S. H. Kwon, H. J. Choi, J. H. Jung and Y. G. Kim, *Compos. Struct.*, 2016, **136**, 106–112.
211 H. Kurita, T. Keino, T. Senzaki and F. Narita, *Sens. Actuators, A*, 2022, **337**, 113427.
212 S. Datta, J. Atulasimha, C. Mudivarthi and A. B. Flatau, *J. Magn. Magn. Mater.*, 2010, **322**, 2135–2144.
213 Y. Zhou, X. Zhao, J. Xu, Y. Fang, G. Chen, Y. Song, S. Li and J. Chen, *Nat. Mater.*, 2021, **20**, 1670–1676.
214 M. A. Khan, J. Sun, B. Li, A. Przybysz and J. Kosel, *Eng. Res. Express*, 2021, **3**, 022005.
215 S. Mostufa, P. Yari, B. Rezaei, K. Xu and K. Wu, *ACS Appl. Nano Mater.*, 2023, **6**, 13732–13765.
216 M. Melzer, D. Makarov and O. G. Schmidt, *J. Phys. D: Appl. Phys.*, 2020, **53**, 083002.
217 J. E. Lenz, *Proc. IEEE*, 1990, **78**, 973–989.
218 M. Melzer, J. I. Mönch, D. Makarov, Y. Zabila, G. S. C. Bermúdez, D. Karnaushenko, S. Baunack, F. Bahr, C. Yan, M. Kaltenbrunner and O. G. Schmidt, *Adv. Mater.*, 2015, **27**, 1274–1280.

219 B. A. Kaidarova, W. Liu, L. Swanepoel, A. Almansouri, N. R. Geraldi, C. M. Duarte and J. Kosel, *npj Flexible Electron.*, 2021, **5**, 2.
220 Z. Wang, M. Shaygan, M. Otto, D. Schall and D. Neumaier, *Nanoscale*, 2016, **8**, 7683–7687.
221 E. Roman, Y. Mokrousov and I. Souza, *Phys. Rev. Lett.*, 2009, **103**, 097203.
222 M. Ha, G. S. C. Bermúdez, J. A.-C. Liu, E. S. Oliveros Mata, B. A. Evans, J. B. Tracy and D. Makarov, *Adv. Mater.*, 2021, **33**, 2008751.
223 B. Lim, M. Mahfoud, P. T. Das, T. Jeon, C. Jeon, M. Kim, T.-K. Nguyen, Q.-H. Tran, F. Terki and C. Kim, *APL Mater.*, 2022, **10**, 051108.
224 T. McGuire and R. Potter, *IEEE Trans. Magn.*, 1975, **11**, 1018–1038.
225 W. Kwiatkowski and S. Tumanski, *J. Phys. E: Sci. Instrum.*, 1986, **19**, 502.
226 Z. Wang, X. Wang, M. Li, Y. Gao, Z. Hu, T. Nan, X. Liang, H. Chen, J. Yang, S. Cash and N.-X. Sun, *Adv. Mater.*, 2016, **28**, 9370–9377.
227 S. Tumański, *Przegl. Elektrotech.*, 2013, 1–12.
228 J. Yu, X. Tang, H. Su and Z. Zhong, *J. Magn. Magn. Mater.*, 2020, **493**, 165695.
229 G. S. C. Bermúdez, H. Fuchs, L. Bischoff, J. Fassbender and D. Makarov, *Nat. Electron.*, 2018, **1**, 589–595.
230 R. Coehoorn, J. C. S. Kools, T. G. S. M. Rijks and K. M. H. Lenssen, *Philips J. Res.*, 1998, **51**, 93–124.
231 T. G. S. M. Rijks, R. F. O. Reneerkens, R. Coehoorn, J. C. S. Kools, M. F. Gillies, J. N. Chapman and W. J. M. de Jonge, *J. Appl. Phys.*, 1997, **82**, 3442–3451.
232 Y. Gong, Z. Cevher, M. Ebrahim, J. Lou, C. Pettiford, N. X. Sun and Y. H. Ren, *J. Appl. Phys.*, 2009, **106**, 063916.
233 A. Siritaratiwat, E. W. Hill, I. Stutt, J. M. Fallon and P. J. Grundy, *Sens. Actuators, A*, 2000, **81**, 40–43.
234 C. Rizal, B. Moa, J. Wingert and O. G. Shpyrko, *IEEE Trans. Magn.*, 2015, **51**, 1–6.
235 C. S. Rizal and Y. Ueda, *IEEE Trans. Magn.*, 2009, **45**, 2399–2402.
236 I. Bakonyi, E. Simon, B. G. Tóth, L. Péter and L. F. Kiss, *Phys. Rev. B: Condens. Matter Mater. Phys.*, 2009, **79**, 174421.
237 K. Takanashi, in *Spintronics for Next Generation Innovative Devices*, 2015, pp. 1–20. DOI: **10.1002/9781118751886.ch1**.
238 S. N. Okuno and K. Inomata, *Phys. Rev. Lett.*, 1994, **72**, 1553–1556.
239 A. Tekgül, M. Alper and H. Kockar, *J. Magn. Magn. Mater.*, 2017, **421**, 472–476.
240 K. Inomata and Y. Saito, *J. Magn. Magn. Mater.*, 1993, **126**, 425–429.
241 M. Melzer, M. Kaltenbrunner, D. Makarov, D. Karnaushenko, D. Karnaushenko, T. Sekitani, T. Someya and O. G. Schmidt, *Nat. Commun.*, 2015, **6**, 6080.
242 M. Kondo, M. Melzer, D. Karnaushenko, T. Uemura, S. Yoshimoto, M. Akiyama, Y. Noda, T. Araki, O. G. Schmidt and T. Sekitani, *Sci. Adv.*, 2020, **6**, eaay6094.
243 J. Lv, G. Thangavel and P. S. Lee, *Nanoscale*, 2023, **15**, 434–449.
244 E. S. O. Mata, G. S. C. Bermúdez, M. Ha, T. Kosub, Y. Zabila, J. Fassbender and D. Makarov, *Appl. Phys. A*, 2021, **127**, 280.
245 M. Ha, G. S. C. Bermúdez, T. Kosub, I. Mönch, Y. Zabila, E. S. O. Mata, R. Illing, Y. Wang, J. Fassbender and D. Makarov, *Adv. Mater.*, 2021, **33**, 2005521.
246 D. E. Heim, R. E. Fontana, C. Tsang, V. S. Speriosu, B. A. Gurney and M. L. Williams, *IEEE Trans. Magn.*, 1994, **30**, 316–321.
247 C. Becker, D. Karnaushenko, T. Kang, D. D. Karnaushenko, M. Faghih, A. Mirhajivarzaneh and O. G. Schmidt, *Sci. Adv.*, 2019, **5**, eaay7459.
248 J.-G. Zhu and C. Park, *Mater. Today*, 2006, **9**, 36–45.
249 T. Scheike, Z. Wen, H. Sukegawa and S. Mitani, *Appl. Phys. Lett.*, 2023, **122**, 112404.
250 S. Willing, K. Schlage, L. Bocklage, M. M. R. Moayed, T. Gurieva, G. Meier and R. Röhlsberger, *ACS Appl. Mater. Interfaces*, 2021, **13**, 32343–32351.
251 J.-Y. Chen, Y.-C. Lau, J. M. D. Coey, M. Li and J.-P. Wang, *Sci. Rep.*, 2017, **7**, 42001.
252 T. Uhrmann, L. Bär, T. Dimopoulos, N. Wiese, M. Rührig and A. Lechner, *J. Magn. Magn. Mater.*, 2006, **307**, 209–211.
253 S. Ota, A. Ando and D. Chiba, *Nat. Electron.*, 2018, **1**, 124–129.
254 Y. Fuji, Y. Higashi, S. Kaji, K. Masunishi, T. Nagata, A. Yuzawa, K. Okamoto, S. Baba, T. Ono and M. Hara, *Jpn. J. Appl. Phys.*, 2019, **58**, SD0802.
255 J. M. Barandiarán, J. Gutiérrez and A. García-Arribas, *Phys. Status Solidi A*, 2011, **208**, 2258–2264.
256 Y.-C. Lai, J. Deng, R. Liu, Y.-C. Hsiao, S. L. Zhang, W. Peng, H.-M. Wu, X. Wang and Z. L. Wang, *Adv. Mater.*, 2018, **30**, 1801114.
257 M. Fattori, S. Cardarelli, J. Fijn, P. Harpe, M. Charbonneau, D. Locatelli, S. Lombard, C. Laugier, L. Tournon, S. Jacob, K. Romanjek, R. Coppard, H. Gold, M. Adler, M. Zirkl, J. Groten, A. Tschepp, B. Lamprecht, M. Postl, B. Stadlober, J. Socratous and E. Cantatore, *Nat. Electron.*, 2022, **5**, 289–299.
258 S. Pyo, J. Lee, K. Bae, S. Sim and J. Kim, *Adv. Mater.*, 2021, **33**, 2005902.
259 D. Sengupta, J. Romano and A. G. P. Kottapalli, *npj Flexible Electron.*, 2021, **5**, 29.
260 G. Gu, N. Zhang, H. Xu, S. Lin, Y. Yu, G. Chai, L. Ge, H. Yang, Q. Shao, X. Sheng, X. Zhu and X. Zhao, *Nat. Biomed. Eng.*, 2023, **7**, 589–598.
261 Q. Wei, G. Chen, H. Pan, Z. Ye, C. Au, C. Chen, X. Zhao, Y. Zhou, X. Xiao, H. Tai, Y. Jiang, G. Xie, Y. Su and J. Chen, *Small Methods*, 2022, **6**, 2101051.
262 X. Cao, J. Zhang, S. Chen, R. J. Varley and K. Pan, *Adv. Funct. Mater.*, 2020, **30**, 2003618.
263 R. Guo, Y. Fang, Z. Wang, A. Libanori, X. Xiao, D. Wan, X. Cui, S. Sang, W. Zhang, H. Zhang and J. Chen, *Adv. Funct. Mater.*, 2022, **32**, 2204803.

264 X. He, Z. Liu, G. Shen, X. He, J. Liang, Y. Zhong, T. Liang, J. He, Y. Xin, C. Zhang, D. Ye and G. Cai, *npj Flexible Electron.*, 2021, **5**, 17.
265 G. Tian, W. Deng, Y. Gao, D. Xiong, C. Yan, X. He, T. Yang, L. Jin, X. Chu, H. Zhang, W. Yan and W. Yang, *Nano Energy*, 2019, **59**, 574–581.
266 T. Liu, W. Mo, X. Zou, B. Luo, S. Zhang, Y. Liu, C. Cai, M. Chi, J. Wang, S. Wang, D. Lu and S. Nie, *Adv. Funct. Mater.*, 2023, **33**, 2304321.
267 J. Wang, J. He, L. Ma, Y. Yao, X. Zhu, L. Peng, X. Liu, K. Li and M. Qu, *Chem. Eng. J.*, 2021, **423**, 130200.
268 L. Yang, J. Ma, W. Zhong, Q. Liu, M. Li, W. Wang, Y. Wu, Y. Wang, X. Liu and D. Wang, *J. Mater. Chem. C*, 2021, **9**, 5217–5226.
269 R. D. I. G. Dharmasena, J. H. B. Deane and S. R. P. Silva, *Adv. Energy Mater.*, 2018, **8**, 1802190.
270 M. S. Woo, J. H. Ahn, J. H. Eom, W. S. Hwang, J. H. Kim, C. H. Yang, G. J. Song, S. D. Hong, J. P. Jhun and T. H. Sung, *Sens. Actuators, A*, 2018, **269**, 524–534.
271 G. Chen, X. Zhao, S. Andalib, J. Xu, Y. Zhou, T. Tat, K. Lin and J. Chen, *Matter*, 2021, **4**, 3725–3740.
272 X. Zhao, G. Chen, Y. Zhou, A. Nashalian, J. Xu, T. Tat, Y. Song, A. Libanori, S. Xu, S. Li and J. Chen, *ACS Nano*, 2022, **16**, 6013–6022.
273 Y. Yan, Z. Hu, Z. Yang, W. Yuan, C. Song, J. Pan and Y. Shen, *Sci. Robot*, 2021, **6**, eabc8801.
274 R. Yang, W. Zhang, N. Tiwari, H. Yan, T. Li and H. Cheng, *Adv. Sci.*, 2022, **9**, 2202470.
275 Q. Zhou, B. Ji, F. Hu, J. Luo and B. Zhou, *Nano-Micro Lett.*, 2021, **13**, 197.
276 W. Liu, Y. Duo, J. Liu, F. Yuan, L. Li, L. Li, G. Wang, B. Chen, S. Wang, H. Yang, Y. Liu, Y. Mo, Y. Wang, B. Fang, F. Sun, X. Ding, C. Zhang and L. Wen, *Nat. Commun.*, 2022, **13**, 5030.
277 H. Xiao, S. Li, Z. He, Y. Wu, Z. Gao, C. Hu, S. Hu, S. Wang, C. Liu, J. Shang, M. Liao, D. Makarov, Y. Liu and R.-W. Li, *Adv. Funct. Mater.*, 2023, **33**, 2214907.
278 H. Hu, C. Zhang, C. Pan, H. Dai, H. Sun, Y. Pan, X. Lai, C. Lyu, D. Tang, J. Fu and P. Zhao, *ACS Nano*, 2022, **16**, 19271–19280.
279 W. Liu, Y. Duo, X. Chen, B. Chen, T. Bu, L. Li, J. Duan, Z. Zuo, Y. Wang, B. Fang, F. Sun, K. Xu, X. Ding, C. Zhang and L. Wen, *Adv. Funct. Mater.*, 2023, **33**, 2306368.
280 P. Rothemund, Y. Kim, R. H. Heisser, X. Zhao, R. F. Shepherd and C. Keplinger, *Nat. Mater.*, 2021, **20**, 1582–1587.
281 M. Cianchetti, C. Laschi, A. Menciassi and P. Dario, *Nat. Rev. Mater.*, 2018, **3**, 143–153.
282 Z. Ding, C. Yuan, X. Peng, T. Wang, H. J. Qi and M. L. Dunn, *Sci. Adv.*, 2017, **3**, e1602890.
283 T. Jia, Y. Wang, Y. Dou, Y. Li, M. Jung de Andrade, R. Wang, S. Fang, J. Li, Z. Yu, R. Qiao, Z. Liu, Y. Cheng, Y. Su, M. Minary-Jolandan, R. H. Baughman, D. Qian and Z. Liu, *Adv. Funct. Mater.*, 2019, **29**, 1808241.
284 W. Wang, X. Xu, C. Zhang, H. Huang, L. Zhu, K. Yue, M. Zhu and S. Yang, *Adv. Sci.*, 2022, **9**, 2105764.
285 X. Duan, J. Yu, Y. Zhu, Z. Zheng, Q. Liao, Y. Xiao, Y. Li, Z. He, Y. Zhao, H. Wang and L. Qu, *ACS Nano*, 2020, **14**, 14929–14938.
286 R. E. Pelrine, R. D. Kornbluh and J. P. Joseph, *Sens. Actuators, A*, 1998, **64**, 77–85.
287 J. Kim, S. E. Chung, S.-E. Choi, H. Lee, J. Kim and S. Kwon, *Nat. Mater.*, 2011, **10**, 747–752.
288 Y. Kim, H. Yuk, R. Zhao, S. A. Chester and X. Zhao, *Nature*, 2018, **558**, 274–279.
289 H.-J. Chung, A. M. Parsons and L. Zheng, *Adv. Intell. Syst. Comput.*, 2021, **3**, 2000186.
290 L. Hines, K. Petersen, G. Z. Lum and M. Sitti, *Adv. Mater.*, 2017, **29**, 1603483.
291 T. Xu, J. Zhang, M. Salehizadeh, O. Onaizah and E. Diller, *Sci. Robot*, 2019, **4**, eaav4494.
292 J. Thévenot, H. Oliveira, O. Sandre and S. Lecommandoux, *Chem. Soc. Rev.*, 2013, **42**, 7099–7116.
293 S. Yi, L. Wang, Z. Chen, J. Wang, X. Song, P. Liu, Y. Zhang, Q. Luo, L. Peng, Z. Wu, C. F. Guo and L. Jiang, *Nat. Commun.*, 2022, **13**, 4177.
294 W. Hu, G. Z. Lum, M. Mastrangeli and M. Sitti, *Nature*, 2018, **554**, 81–85.
295 H. Deng, K. Sattari, Y. Xie, P. Liao, Z. Yan and J. Lin, *Nat. Commun.*, 2020, **11**, 6325.
296 H. Song, H. Lee, J. Lee, J. K. Choe, S. Lee, J. Y. Yi, S. Park, J.-W. Yoo, M. S. Kwon and J. Kim, *Nano Lett.*, 2020, **20**, 5185–5192.
297 C. Li, G. C. Lau, H. Yuan, A. Aggarwal, V. L. Dominguez, S. Liu, H. Sai, L. C. Palmer, N. A. Sather, T. J. Pearson, D. E. Freedman, P. K. Amiri, M. O. de la Cruz and S. I. Stupp, *Sci. Robot*, 2020, **5**, eabb9822.
298 Y. Li, Q. Liu, A. J. Hess, S. Mi, X. Liu, Z. Chen, Y. Xie and I. I. Smalyukh, *ACS Nano*, 2019, **13**, 13875–13883.
299 L. S. Ganapathe, M. A. Mohamed, R. M. Yunus and D. D. Berhanuddin, *Magnetochemistry*, 2020, **6**, 68.
300 T. Mi, Y. Cai, Q. Wang, N. Habibul, X. Ma, Z. Su and W. Wu, *RSC Adv.*, 2020, **10**, 10309–10314.
301 B. Wang, D. Liu, Y. Liao, Y. Huang, M. Ni, M. Wang, Z. Ma, Z. Wu and Y. Lu, *ACS Nano*, 2022, **16**, 20985–21001.
302 H.-W. Huang, M. S. Sakar, A. J. Petruska, S. Pané and B. J. Nelson, *Nat. Commun.*, 2016, **7**, 12263.
303 J. Shintake, V. Cacucciolo, D. Floreano and H. Shea, *Adv. Mater.*, 2018, **30**, 1707035.
304 K. Ham, J. Han and Y.-J. Park, *Int. J. Precis.*, 2018, **19**, 487–494.
305 B. Fang, F. Sun, L. Wu, F. Liu, X. Wang, H. Huang, W. Huang, H. Liu and L. Wen, *Soft Rob.*, 2022, **9**, 233–249.
306 J. Cramer, M. Cramer, E. Demeester and K. Kellens, *Procedia CIRP*, 2018, **76**, 127–132.
307 Y. Haibin, K. Cheng, L. Junfeng and Y. Guilin, *Mech. Mach. Theory*, 2018, **128**, 254–274.
308 D. Wang, H. Hu, S. Li, H. Tian, W. Fan, X. Li, X. Chen, A. C. Taylor and J. Shao, *Sci. Adv.*, 2023, **9**, eadf4051.
309 M. Tan, D. Chen, Y. Cheng, H. Sun, G. Chen, S. Dong, G. Zhao, B. Sun, S. Wu, W. Zhang, J. Han, W. Han and X. Zhang, *Adv. Funct. Mater.*, 2022, **32**, 2202057.

310 A. Iqbal, P. Sambyal and C. M. Koo, *Adv. Funct. Mater.*, 2020, **30**, 2000883.
311 L. Omana, A. Chandran, R. E. John, R. Wilson, K. C. George, N. V. Unnikrishnan, S. S. Varghese, G. George, S. M. Simon and I. Paul, *ACS Omega*, 2022, **7**, 25921–25947.
312 L. Leyssens, B. Vinck, C. Van Der Straeten, F. Wuyts and L. Maes, *Toxicology*, 2017, **387**, 43–56.
313 G. Genchi, A. Carocci, G. Lauria, M. S. Sinicropi and A. Catalano, *Int. J. Environ. Res. Public Health*, 2020, **17**, 679.
314 B. Ankamwar, T. C. Lai, J. H. Huang, R. S. Liu, M. Hsiao, C. H. Chen and Y. K. Hwu, *Nanotechnology*, 2010, **21**, 075102.
315 R. Qiao, C. Yang and M. Gao, *J. Mater. Chem.*, 2009, **19**, 6274–6293.
316 G. L. Nealon, B. Donnio, R. Greget, J.-P. Kappler, E. Terazzi and J.-L. Gallani, *Nanoscale*, 2012, **4**, 5244–5258.
317 K. C. Kwon, E. Jo, Y.-W. Kwon, B. Lee, J. H. Ryu, E. J. Lee, K. Kim and J. Lee, *Adv. Mater.*, 2017, **29**, 1701146.
318 M. Melzer, G. Lin, D. Makarov and O. G. Schmidt, *Adv. Mater.*, 2012, **24**, 6468–6472.
319 G. S. C. Bermúdez, D. D. Karnaushenko, D. Karnaushenko, A. Lebanov, L. Bischoff, M. Kaltenbrunner, J. Fassbender, O. G. Schmidt and D. Makarov, *Sci. Adv.*, 2018, **4**, eaao2623.
320 L. M. Loong, W. Lee, X. Qiu, P. Yang, H. Kawai, M. Saeys, J.-H. Ahn and H. Yang, *Adv. Mater.*, 2016, **28**, 4983–4990.
321 J. Gaspar, H. Fonseca, E. Paz, M. Martins, J. Valadeiro, S. Cardoso, R. Ferreira and P. P. Freitas, *IEEE Trans. Magn.*, 2017, **53**, 1–4.
322 P. I. Baburova, D. V. Kladko, A. Lokteva, A. Pozhitkova, V. Rumyantceva, V. Rumyantceva, I. V. Pankov, S. Taskaev and V. V. Vinogradov, *ACS Nano*, 2023, **17**, 20925–20938.
323 S. R. Goudu, I. C. Yasa, X. Hu, H. Ceylan, W. Hu and M. Sitti, *Adv. Funct. Mater.*, 2020, **30**, 2004975.